Molecular Outflows in Star Forming Regions

Dissertation

zur

Erlangung des Doktorgrades (Dr. rer. nat.)

der

Mathematisch-Naturwissenschaftlichen Fakultät

der

Rheinischen Friedrich-Wilhelms-Universität Bonn

vorgelegt von

Arturo Iván Gómez Ruiz

aus

Campeche, Mexiko

Bonn, Oktober 2012

Angefertigt mit Genehmigung der Mathematisch-Naturwissenschaftlichen Fakultät
der Rheinischen Friedrich-Wilhelms-Universität Bonn

1. Referent: Prof. Dr. Karl M. Menten
2. Referent: Prof. Dr. Pavel Kroupa

Tag der Promotion: 03.06.2013

Diese Dissertation ist auf dem Hochschulschriftenserver der ULB Bonn unter
http://hss.ulb.uni-bonn.de/diss_online elektronisch publiziert.

Erscheinungsjahr: 2014

Dedicada a
Mi pueblo del Mayab...

[Aunque no se conozca, existe el número de las estrellas y el número de los granos de arena. Pero lo que existe y no se puede contar y se siente aquí dentro, exige una palabra para decirlo. Esta palabra, en este caso, sería inmensidad. Es como una palabra húmeda de misterio. Con ella no se necesita contar ni las estrellas ni los granos de arena. Hemos cambiado el conocimiento por la emoción: que es también una manera de penetrar en la verdad de las cosas.

CANEK, de Ermilo Abreu Gómez]

ABSTRACT

This thesis work focus on the study of the molecular emission from outflows produced by jets in regions of star formation. After introducing the topic of star formation, and in particular its related outflow process, a series of studies performed in the millimeter and sub-millimeter wavelengths range are presented, including regions of low-, intermediate-, and high-mass.

Using the Submillimeter Array the SiO, H_2CO, and CH_3OH lines were observed in a prototypical low-mass protostellar outflow. These observations revealed a small scale stratification of the different molecular species, with the SiO mainly tracing the principal bow-shock in the region. However, the kinematic structure at the main bow-shock position is different from that expected in a single bow shock. It is proposed that the high-velocity SiO clump at such position is kinetically independent from the low-velocity gas. The analysis of the SiO emission allowed the determination of the physical conditions of the emitting gas, showing that the the high velocity SiO clumps consist of high density gas, with values comparable to the density of the bullets in the extremely high velocity (EHV) jets. It is proposed that the high-velocity SiO clumps in L1157 have the same origin as the EHV bullets.

The so-called mid$-J$ CO lines (CO $J = 6 - 5$, $J = 7 - 6$) were observed with the APEX telescope towards regions of low-, intermediate-, and high-mass star formation. The warm gas traced by these transitions was particularly found in the high-velocity gas close to the exciting source and in the terminal bow shocks, suggesting that energetic processes are at work in these environments and are especially traced by these lines. A relevant result obtained from the mid$-J$ CO observations is that even at low velocities the emission clearly defines the outflow structures, which is remarkably different from what we see in low$-J$ CO lines. The latter allowed to identify outflows whose axis are close to the plane of the sky, particularly important in region of high-mass star formation. In addition, an EHV outflow was unveiled only by the mid$-J$ CO observations, suggesting that this kind of outflow are particularly traced by mid$-J$ CO lines. Therefore, the overall picture presented by the mid$-J$ CO observations in protostellar outflows is a tendency to trace the most excited regions within them, i.e. the jet component and the terminal bow shocks. Also, the mid$-J$ CO lines have proven to be good tracers of the low-velocity emission in outflows, as well as important tracers of highly excited extremely high velocity emission.

One of the first high spectral resolution observations of high$-J$ CO lines are also presented in this thesis. The high$-J$ CO lines at terahertz frequencies (CO $J = 12-11$, $J = 13-12$), observed with the GREAT instrument on the SOFIA telescope, proved to be important tracers of molecular bullets in the intermediate-mass outflow studied here. In addition to be prominent in the high-velocity bullets, the high$-J$ CO emission was also found at low velocities, which means that previous assumptions made for spectrally unresolved observations that the high$-J$ CO emission in protostellar outflows is produced only at high velocities must be revisited.

Contents

Chapter 1

Introduction

1.1 Star Formation

The star formation process is one of the main topics in astronomy. Observations collected over the last few decades support the scenario in which the stars are formed from condensations of gas and dust that are present within galaxies, the so-called molecular clouds. Inside molecular clouds, small and dense condensations exist, that after collapse will form stars.

Most of the molecular material in the Galaxy is concentrated in Giant Molecular Clouds (GMC), i.e. clouds with masses in the range of 10^5-10^6 $M_\odot$. Inside GMC, dense and massive cores will eventually form massive stars. On the other hand, Small Molecular Clouds (SMC), those with masses $\lesssim 10^4$ $M_\odot$, will only form low-mass stars out of less massive cores.

Observational evidence have lead to the consolidation of a theoretical model which describes most of the phenomena present in the regions where low-mass stars are formed. The classical work by Shu et al. (1987), which successfully explain the characteristics observed in low-mass systems, propose four stages of star formation (see Fig. 1.1):

a) The first stage of star formation begins with the formation of slowly rotating cores. In sub-critical clumps (those without enough mass to overcome the effect of the magnetic field), this occurs through the slow leakage of magnetic (and turbulent) support by ambipolar diffusion. In super-critical clumps (those with enough mass to overcome magnetic support by self gravity), the clump can also fragment when it contracts as a whole.

b) The second stage starts when the core inside the cloud becomes unstable and collapse dynamically, the so-called *inside-out* collapse. This evolutionary phase is characterized by the existence of a central protostar and a disk, both of them embedded in a envelope of gas and dust in collapse. The collapsing material produce an accretion shock when it reaches the central protostar and disk, thus contributing to the total luminosity of the protostellar system.

c) If the convection and differential rotation of the star are combined to produce a dynamo, the star can evolve to a stage with a stellar wind. However, the ram pressure of the material in collapse onto the protostar halt the outflow. It is only when the ram pressure decreases, due to the material that now is falling mainly through the disk, that the stellar wind can escape through the channels with less pressure, i.e. the rotational poles, producing collimated jets and bipolar outflows.

d) As the time evolves, more and more material falls preferentially through the disk, and then the aperture angle of protostellar outflows becomes wider, sweeping up more material from the molecular envelope. Eventually the pre-main sequence object emerges accompanied by a debris disk.

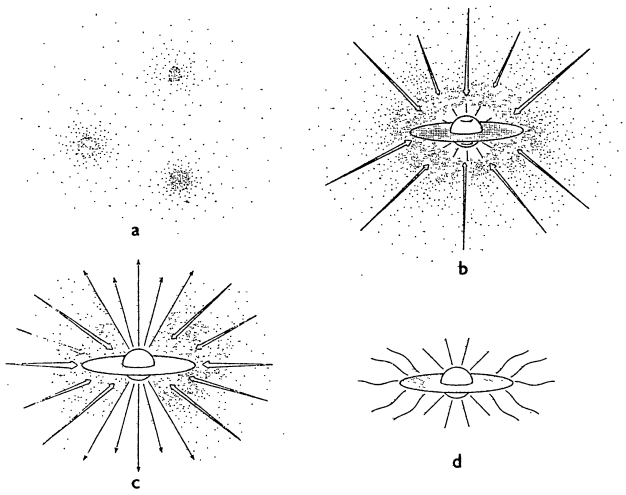

Figure 1.1: The four stages of star formation, according to Shu et al. (1987). See description in the text.

Accretion and outflow are therefore two related processes that characterize star-formation. Both phenomena have been widely confirmed in low-mass star forming regions. However, although outflows in massive regions have bee widely studied, the presence of an accretion disk is still under debate (e.g. Cesaroni et al. 2007). That has lead to a controversy on whether high-mass stars form via the collapse-accretion/outflow process or by competitive accretion including possibly stellar mergers in dense clusters (Bonnell & Bate 2005; Zinnecker & Yorke 2007). The principal problems to unambiguously establish a massive star formation scenario reside in the intrinsic characteristic of the massive star formation environments, such as the typical distances to massive regions of at least few kilo parsec (kpc) and the tendency of massive stars to form in cluster of several members (including low-mass stars). The larger distances translates into the need of high angular resolution observations (below one arcsec) to separate the individual members of the cluster. The

current limited observational capabilities to reach such angular resolution in the millimeter wavelength regime have resulted in the elusive detection of massive disks. On the other hand, bipolar molecular outflows extend to larger distances from the protostar than the disk systems, and therefore they are a potential tool to prove the accretion/outflow process in the formation of high-mass stars and investigate their properties.

For all these challenges and their intrinsic importance, understanding the formation of high-mass stars is one of the main problems of modern astrophysics. In recent years, unbiased surveys in the Mid-IR and sub-mm have given us new samples of candidates of high-mass protostars in the earliest phase of formation. Systematic studies trying to characterize such objects are underway. Examples of these surveys are the GLIMPSE survey in the Mid-IR (MIR) (Benjamin et al. 2003) and ATLASGAL in the sub-mm (Schuller et al. 2009).

1.2 Low-mass Outflows

1.2.1 The CO emission

The first evidence of the existence of molecular outflows in star formation was found in the 1970's by mapping the high-velocity emission of the rotational transition (quantum number J) 1–0 of the CO molecule (Kwan & Scoville 1976). Soon after it was proven that the structure of the emission presented a bipolar structure (Snell et al. 1980; Rodriguez et al. 1980), extending up to distances of 0.1-1 pc, and in some cases with relative velocities (respect the cloud velocity) close to 100 km s^{-1} (Snell 1987). The conclusion was that this phenomenon must be related to expansive motions of molecular gas from the star in the process of formation, to what since then has been known as *high-velocity molecular outflows*. The high-velocity emission related to outflows was also observed in rotational transitions of other molecules, such as SiO, SO, HCN (Kwan & Scoville 1976).

The high-velocity emission observed in the spectra of certain molecules are known as *high-velocity wings*, being the *red-wing* the high velocity emission corresponding to the gas going away from the observer, and the *blue-wing* the emission moving towards the observer (see Fig. 1.2).

An important characteristic of a molecular outflow is that, in its spatial distribution, gas in the *red-wing* and the gas in the *blue-wing* are not coincident, but in general they present a bipolar distribution, forming two lobes located at each side of the poles of the protostar (see Fig. 1.3). This result implicates that high velocity gas may be ejected from the protostar, forming lobes of gas along the axis of rotation, moving away from the central region.

The CO molecule, which is very important for the study of the structure of molecular clouds (the second most abundant molecule in the ISM after the H_2), became also crucial for the study of molecular outflows. The current knowledge on the structure and dynamical properties of molecular outflows has been based mainly

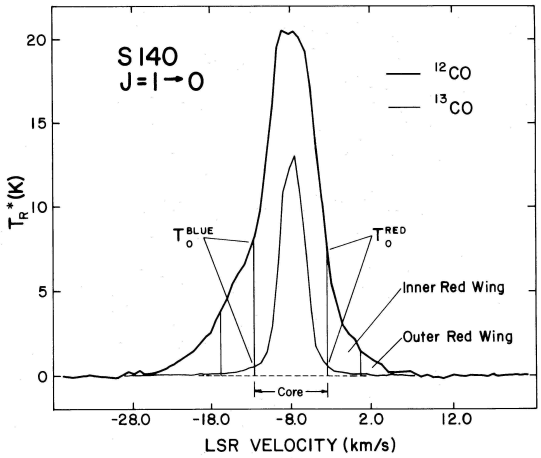

Figure 1.2: CO (1–0) spectrum with high velocity wings in the star forming region S140. Upper profile shows the ^{12}CO (1–0) line while lower profile the ^{13}CO (1–0) line. It is also shown the three velocity ranges in which the line is divided: core, internal and external wings (Margulis & Lada 1985).

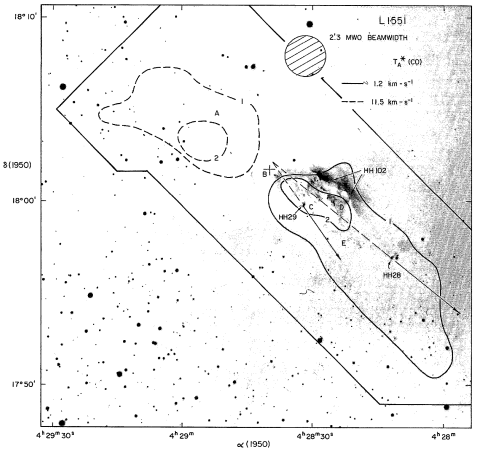

Figure 1.3: Bipolar molecular outflow observed in CO(1–0) in the region L1551. The blue-lobe (solid contours) and the red-lobe (dashed contours) are located at two opposite sides respect the central source indicated in the image by the cross (Snell et al. 1980).

on CO observations, predominantly of low$-J$ transitions (usually up to $J_u = 3$), with single-dish and interferometers.

Low$-J$ CO observations of molecular outflows in low-mass systems, collected during the 1980's and 1990's, pointed out that the line broadening comes mainly from two components: a standard high velocity (SHV) and an extremely high velocity (EHV) component. The SHV component is present at relative velocities (respect the cloud velocity) of up to 20 km s^{-1}, while EHV component span from relative velocities of

40 km s^{-1} up to 100 km s^{-1} (Bachiller et al. 1990). An important difference between these two components, as observed with low$-J$ CO lines, is that the EHV is weaker than the SHV, with the later more massive than the former. Another important feature revealed by interferometric observations is the collimation factor, which is higher for EHV than for SHV (see figure 1.4).

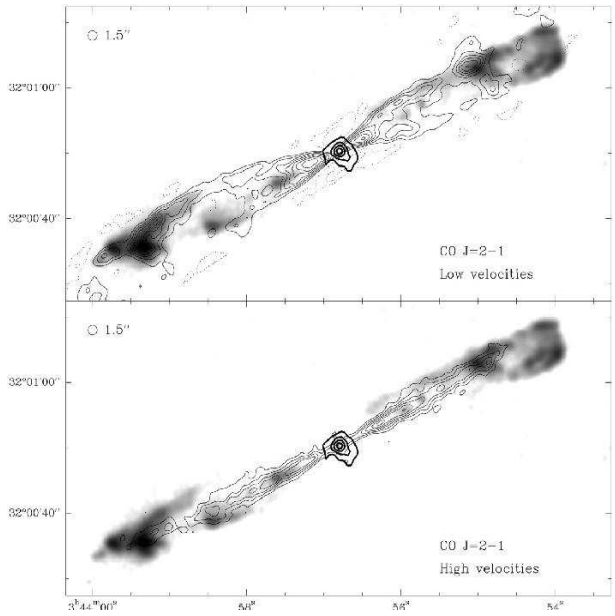

Figure 1.4: CO $(2-1)$ maps of low- and high-velocity emission (thin contours) overlaid on the H_2 emission (grey scale). Thick contours show the continuum emission at 230 GHz, which point out the presence of a protostellar disk (Gueth & Guilloteau 1999a).

Following the initial suggestion by Snell et al. (1980), there exist a consensus that the SHV component consist of gas that has been swept-up by the action of a stellar wind. Indeed, the moment carried out by the EHV component is high enough to put in motion the SHV component. In addition, it has been observed that the terminal velocity of the EHV component decreases with distance, while for the SHV it increases with distance, which at the end suggest that the EHV component injects moment to the ambient cloud to produce the SHV component (Bachiller 1996).

It has also been observed that the structure of the EHV component is not continuous, but presents well defined peaks in space and velocity. Such peaks are known as *molecular bullets* (Bachiller et al. 1990). The EHV gas shows a structure constituted by a chain of *molecular bullets* interconnected by weak emission, while SHV gas shows as extended lobes around the EHV gas (see figure 1.5). In Fig. 1.6, representative spectra with EHV peaks are shown. *Molecular bullets* can reach velocities up to 100 km s^{-1}, but not all bullets can reach such extreme velocities. The

typical size of such *molecular bullets* is $\sim 10^{-2}$ pc and masses of about 10^{-4} $M_\odot$ (Bachiller et al. 1990). *Molecular bullets* tend to be regularly separated along the jet axis and in symmetric groups. The position and velocity symmetry found in the blue- and red-shifted bullets suggest that each pair of bullets correspond to a bipolar ejection event which take place close to the YSO. Such ejection events could be quasi-periodic, with a time interval between two consecutive events of the order of 10^3 years (Bachiller 1996).

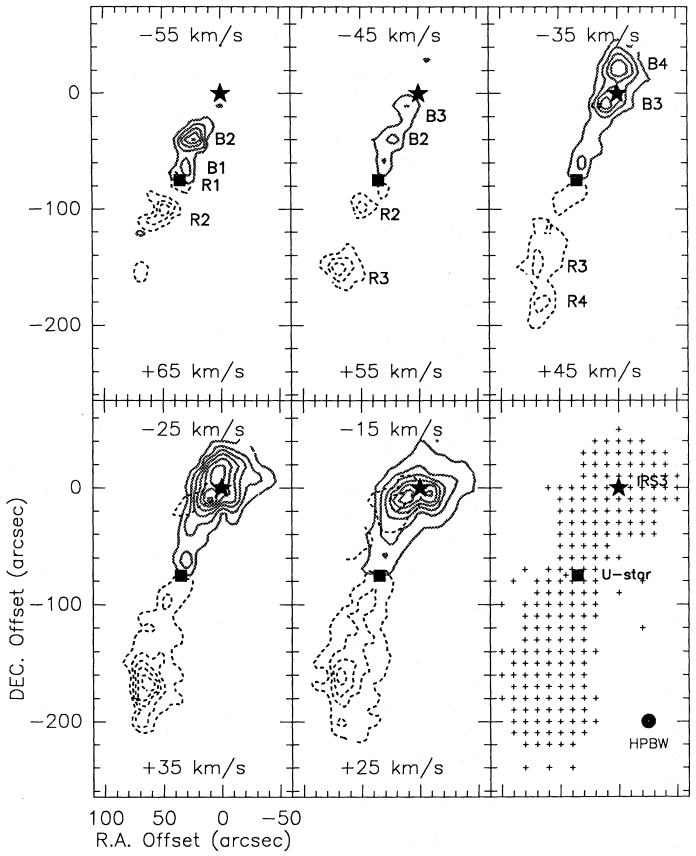

Figure 1.5: The protostellar outflow in the L1448 region, which presents *molecular bullets* . B1, B2, B3 refer to blue-shifted bullets, and R1, R2, R3, R4 are the red-shifted bullets. Each panel shows the CO (2–1) emission integrated in intervals of 10 km s^{-1}, and centered at the indicated velocities (i.e. different velocity ranges). The bottom left panel showing the coverage of the mapped region (Bachiller et al. 1990).

In recent years, CO observations at 0.8 mm (i.e. CO 3–2 transition) have shown that bullets traced by these submillimeter transitions appear closer to the central protostars than bullets traced by CO transitions in the millimeter range (Palau et al. 2006; Hirano et al. 2006). The importance of these submillimeter observations is that they may help to our understanding of the origin of the outflow process in star

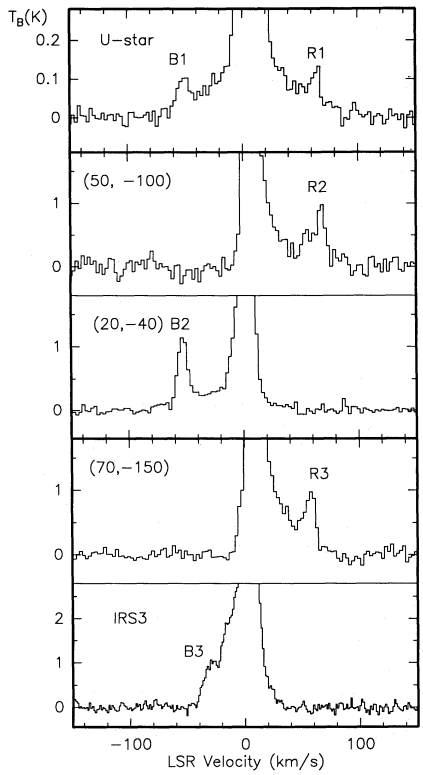

Figure 1.6: The CO (2–1) spectra obtained at different positions within the lobes of the L1448 outflow. The components corresponding to the *molecular bullets* are labeled as in figure 1.5. The number in parenthesis indicates the offset position, respect the IRS3 source, on which each spectrum was taken.

formation, since the bullets revealed by such transitions are possibly related with the primary jet. Later on we provide a more complete discussion about this point since this topic is of key importance for the present thesis.

1.2.2 The SiO emission

Early in the 1980's it was found that SiO was another molecule tracing high velocity gas in YSO's. In the 1990's CO and SiO observations were critical to establish the dynamical properties of the outflow process in star formation.

Molecular outflow observations in low-mass systems indicates that the SiO emission has the same components as observed in CO: SHV and EHV. However, the important difference is that the SiO emission is not present in the ambient cloud, contrary to the CO case (Bachiller et al. 1991b). In the regions where the SiO emission has been detected, its abundance appears to be increased. The high increment of the SiO abundance in the high-velocity gas, could be explained if the SiO molecule is formed in shocked regions. Shock waves destroy dust grains, releasing

Silicon in gas phase, which combined with oxygen (mainly O_2), eventually increase the SiO abundance in the gas phase(Martin-Pintado et al. 1992a). In this way, the SiO molecule is able to trace an element of the jet-cloud interaction that is not seen with other tracers of molecular outflows.

Observations in low-mass regions have shown that each pair of *molecular bullets* seen in CO have their counterpart in SiO (Bachiller et al. 1991b). Typically, CO emission is stronger than the SiO emission. However, in the low-mass system related to L1448-mm, the bullets very close to the exciting source are stronger in SiO than in CO. An interesting trend is found in the SiO to CO column density ratio, with higher values towards higher velocities. In addition, the SiO abundance is increased by a factor of 10^5 in the *molecular bullets* close to the protostar (Bachiller et al. 1991b).

Recent studies have shown that the SiO submillimeter emission from low-mass outflows seems to trace regions closer to the protostar compared to the CO emission (Palau et al. 2006; Hirano et al. 2006). For the outflow related to the HH211-mm protostar, Palau et al. (2006) determined that the SiO (8–7) emission in the inner bullets (called B1 and R1) are located at 450 AU from the protostar (see figure 1.7). At distances $\geq$ 1500 UA from the protostar, the SiO (8–7) emission present velocities that increase with the distance. The CO (3–2) emission also increases its velocity with distance, at such scales, but reaching lower velocities than the SiO (8–7) emission. An interpretation of this fact is that the SiO (8–7) is tracing denser gas closer to the primary jet than the gas traced by CO (3–2). The importance here is that the SiO emission may be closely related with the primary jet likely originated close to the protostar.

1.3 Massive Outflows

It is known that Massive Young Stellar Objects (MYSO) pass through an outflow phase similar to low-mass YSOs. However, the tendency of massive stars to form in clusters (including low-mass members) produce a situation in which within a same region multiple outflows are present, making difficult the study of the outflow properties of a single member (see figure 1.8). In addition, the distances in which this clusters are located (typically few kilo parsec) make more difficult, even for high angular resolution interferometric observations, detailed studies of outflow structures down to scales of less than 1000 AU (Beuther 2005). As a result, relatively few outflows in MYSO have been studied in great detail, and thus leaving open the question on whether or not outflows in massive star formation are produced by the same processes known in low-mass systems (Shepherd & Churchwell 1996).

The pioneering study by Shepherd & Churchwell (1996) on molecular outflows from high-mass systems proved that they were similar to the outflows found in low-

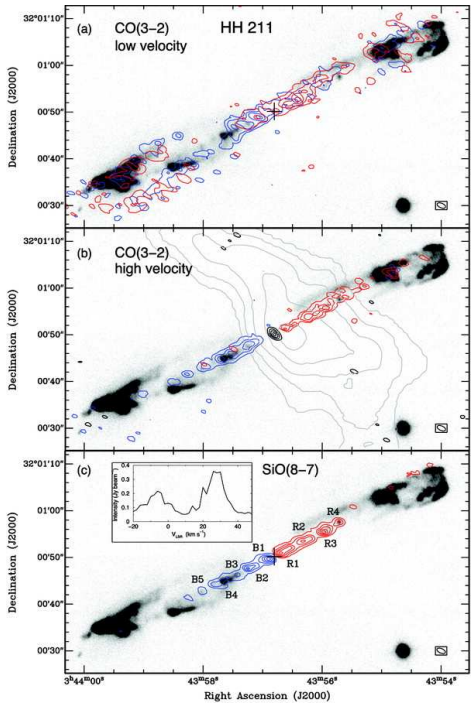

Figure 1.7: The $CO(3-2)$ and $SiO(8-7)$ emission maps overlaid on H_2 emission at 2.2 μm in HH211-mm (Palau et al. 2006). a) $CO(3--2)$ integrated emission at low velocities (blue:2 to 8 km s^{-1}; red:10 to 18 km s^{-1}). b) CO(3–2) high velocity emission (blue:-14 to 0 km s^{-1}; red: 20 to 40 km s^{-1}). Black contours show the millimeter continuum emission. The $NH_3(1,1)$ is shown by grey contours. c) High velocity $SiO(8--7)$ emission (blue:-20 to 0 km s^{-1}; red: 20 to 42 km s^{-1})

mass regions. However, their physical parameters were found with higher values than in the low-mass case. In their sample of MYSO, outflow masses between 16 - 72 $M_\odot$ and kinetic energies between 10^{45} y 10^{46}erg were found. They also found that the outflow mass rate, $\dot{M}$, increases with the luminosity of the protostar, and is several orders of magnitudes higher for massive outflows compared with low-mass outflows. However, they also showed that massive outflows appear to be less collimated than the ones in low-mass systems. This was later confirmed by Richer et al. (2000), who found collimation factors in the range of 1 to 1.8. These first studies have shown that collimation of massive outflows is not only dependent of the age of the system (characteristic time scales of 10^2 - 10^5 years), but also that more luminous MYSO do not produce collimated outflows. On the other hand, higher angular resolution observations by Beuther et al. (2002b) proved that massive outflows were indeed as collimated as in the low-mass case, since accounting for projection and angular resolution effects, collimation factor can reach a value close to 10, i.e. similar to the highest values found in low-mass outflows. Therefore, outflow's collimation in massive star forming regions has a strong dependence on the angular resolution the observations are made Beuther et al. (2002b).

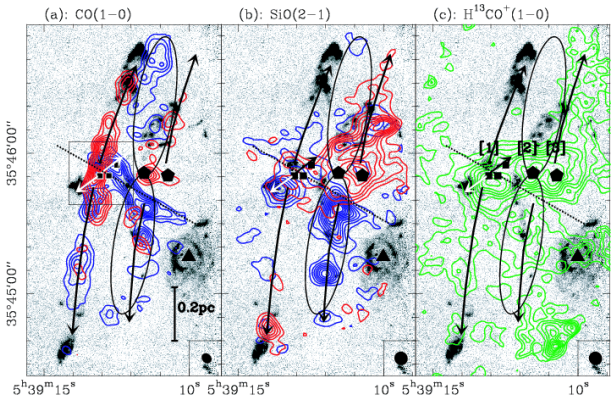

Figure 1.8: Interferometric observations of the region IRAS 05358+3543. Contours show the high velocity wings, blue and red. Maps are overlaid on the H_2 emission in grey scale. (a) CO $(1 - -0)$, (b) SiO $(2 - -1)$ and (c) $H^{13}CO^+$ $(1 - -0)$. Green contours show the total $H^{13}CO^+$ (1–0) integrated emission. In all images the arrows point out the three main outflows in the region. The ellipses are a second interpretation of the west outflow. Squares indicate the millimeter sources, diamonds the $H^{13}CO^+$ (1–0) emission peaks, and the triangle the positions of the IRAS source at 12 μm (Beuther et al. 2002a).

In the last years interferometric observations of molecular outflows in massive regions have shown that protostars more massive than 10 $M_\odot$ can present collimated outflows (Beuther 2005). One of the best examples is the massive protostar IRAS 05358+3543 (figure 1.8). This source, which is in a stage prior to the formation of an Ultra Compact (UC) HII region, presents three molecular outflows. In one of these outflows a collimation factor of 10 has been measured. The infrared source related to this outflow has a bolometric luminosity of $10^{3.8}$ $L_\odot$, which correspond to a star of spectral type B1 Beuther et al. (2002a). On the other hand, collimated outflows in stars earlier than B0 have not been fully demonstrated by observations, although on average early type B protostars are less collimated than the low-mass case (Shepherd 2005).

The observational data base at high angular resolution in MYSO's is still poor, but they suggest that collimation in massive outflows change with time (Beuther 2005). In the earliest phases of massive star formation, outflows with a high collimation factor tend to appear in systems with ages less than 10^4 years, a time in which the central object has not reach the Main Sequence. On the other hand, poorly collimated outflows (aperture angle more than 50 degrees) are associated with more evolved objects in which HII regions are detected (i.e. central source reached the Main Sequence). The latter is due to the radiation field in the form of Lyman photon which ionize the outflow gas, inducing a larger velocity dispersion at the base of the jet, and therefore minimizing the collimation effect. Recent numerical simu-

lations by Vaidya et al. (2011) have supported the later scheme. In this scenario it is evident that the non-detection of collimated outflows in O type protostars is due to the extremely short time scale in which these objects evolve, making difficult to find this morphology in such objects (Beuther 2005).

1.4 Physical properties of protostellar outflows

The determination of physical parameters of molecular outflows is of crucial importance in the study of star formation, since it allows to test or even discriminate the different formation mechanism involved. However, in the practice, the calculation of such parameters is not easy. For example, in the case of CO a difficulty is found when trying to separate the high velocity component from the ambient gas emission, in particular for low$-J$ CO transitions. Also, observed in the plane of the sky, the inclination angles of outflows are usually unknown, and therefore inducing uncertainties in the determined values. A series of studies of the physical properties in molecular outflows from low-mass systems by Cabrit & Bertout (1986, 1990, 1992) are commonly used for the determination of such parameters. Here we present the expression normally used in such studies:

$$\begin{aligned} M_{out} &= M_b + M_r = (N_b \times area_b + N_r \times area_r) m_{H2} \\ P &= M_b \times v_{maxb} + M_r \times v_{maxr} \\ E_{kin} &= \frac{1}{2} M_b \times v_{maxb}^2 + \frac{1}{2} M_r \times v_{maxr}^2 \\ t &= \frac{r}{(v_{maxb} + v_{maxr})/2} \\ L_m &= \frac{E_{kin}}{t} \end{aligned}$$

In these equations, M_{out} is the total mass carried out by the outflow, including both lobes (M_b y M_r). N_a y N_r are the H_2 column densities[1] from the blue and red lobes, respectively (where m_{H_2} is the mass of hydrogen molecule). The quantities $area_b$ and $area_r$ are the sizes of the lobes (projected on the plane of the sky). The moment, P, carried out by the outflow is calculated from the mass of the lobes (M_a and M_r) and the maximum velocity of blue and red wings (v_{maxa} and v_{maxr}); the kinetic energy (E_{kin}) is obtained from these same parameters. From E_{kin} we can find the mechanical luminosity (L_{mec}), which is defined as the kinetic energy per unit time. The dynamical time scale is calculated by the ratio between the length of the outflow and the average of the maximum velocities.

[1]Particle density per unit area along the line of sight.

It has been found that the only difference between low- and high-mass outflows are the time in which they are present, the mass carried out, and the energies involved in the process. An important correlation has been found between the outflow's mechanical luminosity and the luminosity of the protostar, with the former increasing as the latter increase, although the outflow's mechanical luminosity show lower values than the luminosity of the protostar. It is also observed that molecular outflows possess energies comparable to the accretion process (Bachiller 1996). Finally, these quantities depends strongly on the mass of the star they are related with.

From the discussion above we can infer that the physical parameters related to outflows present a wide range of values. Including low- and high-mass systems, the estimation of such physical properties indicates that bipolar molecular outflows are an energetic process (characteristic energies of $10^{43} - 10^{48}$erg), and therefore an important phenomenon which impact the evolution of molecular clouds (see discussion below). As determined from low$-J$ CO observations, high-velocity molecular outflows are constituted by relatively cold molecular gas ($T_k \backsimeq 10 - 50$K), with masses between 10^{-2} to 1000 solar masses, with velocities between 10 to 100 km s^{-1}. The collimation factor varies from 1 to 30, being the low-mass systems where we found the more collimated outflows. In table 1.1 a summary of the properties of molecular outflows in star formation is presented.

Table 1.1: Physical properties of high-velocity molecular outflows

Mass	0.01-1000 $M_\odot$
Kinetic temperature	10-50 K
Velocity	10-100 km s^{-1}
Size	0.1-5 pc
Collimation factor	1-30
Kinetic energy	10^{45}-10^{48} erg
Time scale	10^2-10^5 years
Mechanical luminosity	0.01-900$L\odot$

Note– Compiled from Bachiller (1996) and Beuther et al. (2002b)

1.5 Jet/outflow models

During the last few decades, several outflows models have been proposed to explain the observations towards protostellar outflows. The outflow models can be divided into four classes: wind-driven shells, jet-driven bow shocks, jet-driven turbulent flows, and circulation flows (Arce et al. 2007, see Fig. 1.9). The firs three explain molecular outflows as material entrained by a wide-angle wind or accelerated

by a highly collimated jet, while in the last one the molecular outflows are produced by deflected infalling gas. Out of them, the jet-driven bow shocks and the wind-driven shells are the models that account for most of the observed characteristics of protostellar outflows. In the following we focus on explaining the main properties of these two kind of models.

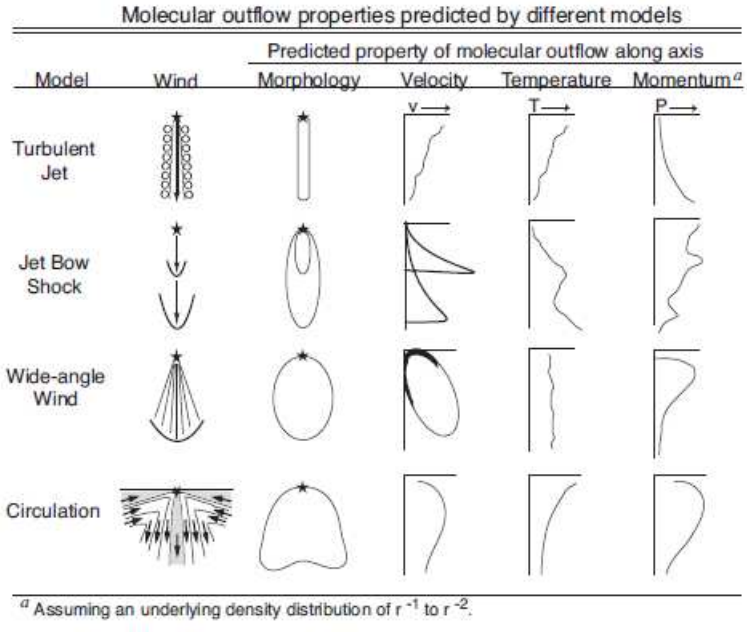

Figure 1.9: Outflow models as summarized by Arce et al. (2007).

wide-angle wind. In the wind-driven shell model, we have the action of a wide-angle radial wind that blows into the surrounding ambient material, producing a thin swept-up shell that can be identified as the outflow shell observed in the standard high velocity outflows (Shu et al. 1991; Li & Shu 1996; Matzner & McKee 1999). This kind of models explain particularly the old outflows of large lateral extents and low collimation (Arce et al. 2007). The wide-angle wind models are able to produce CO outflows with large widths, i.e. outflow widths of 0.1 to 0.2 pc, with an age of about 10^4 years, and thus consistent with observations. However, these models have problems producing discrete bow shock type features as seen in high angular resolution CO maps, and discrete position-velocity spur structures. These features are difficult to produce as the wide-angle wind impacts all locations on the shell.

Jet-driven bow shocks. In the jet driven bow shock model, a highly collimated jet propagates into the surrounding medium, producing a thin outflow shell around the jet (Raga & Cabrit 1993; Masson & Chernin 1993). As the jet impacts the ambient material, a jet shock and a bow shock are formed at the head of the jet, and thus high pressure gas between the shocks is ejected sideways out of the jet beam. The sideways ejection interacts with unperturbed ambient gas through a broader bow shock surface, creating an outflow shell surrounding the jet. In addition, an

episodic variation in the mass-loss rate produces a chain of knotty shocks and bow shocks along the jet axis within the outflow shell (Raga & Kofman 1992). Jet simulations that include periodic velocity pulses present position-velocity features with a sequence of Hubble wedges, similar to that observed in molecular outflows. In addition, current jet-driven models can qualitatively account for the broad range of CO velocities near to H_2 shocks, and the morphological relation between the CO and H_2 emission in young and collimated outflows. However, jet driven outflow models have difficulty producing the observed width of poorly collimated outflows. These models produce narrow outflows mainly because the shocked gas in the working surfaces limits the transverse momentum (perpendicular to the jet axis) that can be delivered to the surrounding medium. Jet-driven models have also difficulties producing the observed outflow momenta, and this comes mainly because of the fact that the jet-driven models predict mean transverse velocities much lower than observed.

A synthesis model, which combines attributes from both the wind- and jet-driven models, is arguably the best option to produce the available outflow data (Arce et al. 2007). In particular, as we have shown in previous sections, CO observations in some cases reveal the simultaneous presence of collimated jets and less collimated structures, with the jet component usually more prominent in sub-millimeter transitions. There is increasing evidence that the morphology of some molecular outflows is better described with a dual-wind model (e.g. Arce & Goodman 2002). In the optical, for example, line profiles of T Tauri stars show two velocity components: (1) a high-velocity component argued to arise in a jet, and (2) a low-velocity component that might result from a disk-wind (Kwan & Tademaru 1995). Recently, an unified model of molecular outflows has been proposed by Shang et al. (2006). In this unified model a single physically motivated, stratified MHD wind running into ambient media of different density distributions, produces a shell of mostly swept-up ambient material and a jet along the axis that is the densest part of the primary wind. Indeed this model has been tested with the prototype of jet-like outflow, HH 211, providing the strongest support for the unified wind model. Moreover, these authors propose that the jet-like and classical wide-angle molecular outflows are unified in an evolutionary sequence, with the jet-like component dominating the early stages of evolution. However, additional observational tests are needed to finally verify whether this unified wind model is able to account for the wide range of observed features in molecular outflows from low- and high-mass protostars, and along their different evolutionary stages.

1.6 Impact of outflows in star formation

The outflow process in star formation can affect the surrounding protostellar environment from scales of a few AU up to tens of parsec (Arce et al. 2007). The impact of outflows on the surrounding environment can be divided in three types, as explained below.

Outflow-envelope interaction. Owing to its origin within a few AU of the protostar, the protostellar winds interact with the dense circumstellar envelope, which is the principal protostellar mass reservoir with sizes from 10^3 to 10^4 AU. Indeed, studies of the circumstellar gas within 10^4 AU in low-mass protostars show that outflows contribute to the mass-loss of the surrounding dense gas (from about 10^{-8} to 10^{-4} $M_\odot$ yr^{-1}). Outflows from class 0 sources are actually able to modify the kinematics and distribution of the high-density gas surrounding a protostar. In L1157, for example, high-density molecular line tracers have shown the dense gas as an structure elongated along the outflow axis, at scales of 4000 AU (Gueth et al. 1997; Beltrán et al. 2004). Therefore, the results show that young outflows entrain dense envelope gas along the outflow axis. Wide-angle outflows, usually observed in evolved protostars, have also an impact in the gas envelope. There is observational evidence, in low-mass protostars, of the erosion of the envelope due to the outflow-envelope interaction (e.g. Arce & Sargent 2004). Thus, it is clear that the outflow-envelope interaction will have an impact on the subsequent circumstellar density distribution, as it will help widen the cavity created by the outflow expansion and therefore constrain the infall region (Arce et al. 2007).

Outflow-core interaction. The evidence of the interaction between the outflow and the protostellar core, which consist of dense gas within 0.1 to 0.3 pc of the protostar, comes from detection of velocity shifts in the core's medium and high-density gas (Arce et al. 2007). The average velocity shifts in the dense core gas are usually lower than the average velocity of the CO outflow, which is consistent with a momentum-conserving outflow entrainment process. Outflows appear to be the main mechanism able to efficiently sweep out about 90% of the parent core by the end of the pre-main sequence stage of intermediate-mass protostars (Fuente et al. 2002). Additionally, outflows from low- and high-mass protostars have kinetic energies comparable to the gravitationally binding energy of their parent core, suggesting that they have the potential to disperse the core. (e.g. Tafalla et al. 1997). However, additional systematic observations in a statistical significant sample, including outflow-harboring cores in different stages of evolution, are required in order to fully understand the core dispersal process and to test whether or not outflows are able to disperse their entire parent core (Arce et al. 2007).

Outflow-cloud interaction. Giant molecular outflows are commonly observed in regions of low- and high-mass star formation, interacting with cloud gas at distances greater than 1 pc from their driving protostar (e.g. Reipurth et al. 1997). Giant molecular outflows from intermediate- and high-mass protostars are able to entrain from tens to hundreds of solar masses, induce velocity gradients at parsec scales, produce dense and massive shells of swept-up gas at large distances, and even have the potential to break the cloud apart (e.g. Fuente et al. 1998; Shepherd et al. 2000). Similarly, giant outflows from low-mass protostars have kinetic energies comparable (or larger than) the turbulent energy and gravitational binding energy of their parent cloud (Arce 2003). Since most of the star formation in the Galaxy appears to occur in cluster mode, multiple outflows should be even more disruptive in their cloud than in isolated star formation. Multiple outflows from a cluster region interact

with a substantial volume of their parent cloud and may be a considerable source of energy for driving the supersonic turbulence inside clouds (e.g. Mac Low & Klessen 2004). However, more information on both theory and observations are still needed to fully understand the role of giant outflows and multiple outflows in star formation environments.

1.7 The present thesis

As described in previous sections, the current knowledge in the study of protostellar outflows shows that although a large body of information is available in molecular tracers to draw a general picture of the role the mass-loss phenomenon in star formation, several questions are still open. Some of them are actually of crucial importance for the understanding of the star formation process. One of them is the jet collimation in low- and high-mass protostars, that due to the high opacity of the regions were this is suppose to happen, it's direct observation has remained elusive. Another important question is whether massive stars in their early stages of formation develop jets as collimated as the ones observed in low-mass regions, and also if there are protostellar disk present that may confirm the disk-jet connection in the formation of massive stars. The recent access to the sub-millimeter wavelength window from excellent ground-based locations, like the Atacama desert in Chile, is giving us the opportunity to shed light into some of these key questions.

In particular, the Atacama Pathfinder Experiment (APEX) with it's CHAMP+ instrument allows for the first time the mapping of large regions of the sky simultaneously at 450 and 350 μm ($\sim$600 and 800 GHz, respectively). In this spectral window, the CO (6–5) and (7–6) transitions, or mid$-J$ CO transitions, are available as tools to trace the warm gas in protostellar outflows, due the high energy required for their excitation (upper energy of few hundred Kelvin). In previous sections we have described that going from CO observation at 1-3 mm to 0.8 mm lead to a higher tendency of tracing inner bullets that may be related to the primary jet. Then the question is whether we can get even closer to the primary jet by observing CO transitions at around 0.4 mm. Obviously, the answer will come with observations of these transitions at sub-arcsec scales, possible only with future sub-mm interferometers such as the Atacama Large Millimeter/sub-millimeter Array (ALMA), currently under construction in the Atacama desert in Chile. However, before ALMA, pilot studies at lower angular resolution are necessary to characterize the emission in these transitions. In addition, at the end of 2011 another facility started operation at the sub-millimeter/far-infrared region: the Stratospheric Observatory for Far-Infrared Astronomy (SOFIA). With its GREAT spectrometer, SOFIA gives access to even higher$-J$ CO transitions that allow us to study the hot gas in protostellar outflows. The main objective of the present thesis is to provide a single-dish study of mid- and high$-J$ CO transitions in protostellar outflows by observations with CHAMP+ at APEX and GREAT at SOFIA.

As a starting point, I present in chapter 2 a study of 'standard' molecular tracers

towards a prototypical low-mass source, L1157, which provided me insights into the general characteristic of low-mass outflows, but also showed me the inherent complications in the study of these relatively well known sources. In Chapter 3 I show the results of a project to characterize the mid$-J$ CO emission in two prototypical highly collimated low-mass outflows, L1448 and HH211. In Chapter 4 mid$-J$ CO maps covering several intermediate-mass protostars in the OMC-2/3 region are presented. In Chapter 5, a mid$-J$ CO mapping follow-up to the ATLASGAL survey is shown, together with complementary data at one millimeter with the Submillimeter Array (SMA). In Chapter 6, single-pointing observations of two high$-$J CO transitions made with the GREAT instrument on board SOFIA towards the well-know intermediate-mass outflow Cep-E outflow is presented. Finally, in Chapter 7 the main conclusions and future work motivated by the results of this thesis are given.

Chapter 2

Sub-Millimeter Array observations of L1157: A case of study of SiO emission in low-mass outflows[1]

2.1 Introduction

There is now increasing evidence that extremely young outflows driven by class 0 low-mass protostars interact with surrounding ambient gas and produce strong shock waves. One prototypical and well-studied example of an outflow with strong shocks is the well-collimated bipolar outflow driven by the class 0 source of $L_{bol} \sim 11\ L_{\odot}$, IRAS 20386+6751, in the L1157 dark cloud at 440 pc from the Sun (e.g., Umemoto et al. 1992; Gueth et al. 1997). This outflow has been extensively studied with various molecular lines. The spatial-kinematic structure of the CO (1–0) was reproduced by a model of two limb-brightened cavities with slightly different axes (Gueth et al. 1996). The locations of the two cavities are indicated by the yellow and green lines in Fig. 1. At the tips of these two cavities, labeled B2 and B1, respectively, strong SiO and NH_3 (3, 3) emission lines, which are considered to be good tracers of shocked molecular gas, are observed (Gueth et al. 1998; Zhang et al. 1995, 2000; Tafalla & Bachiller 1995). On the basis of the observations of the highly excited $(J, K) = (5, 5)$ and (6, 6) NH_3 emission lines, and the CO (6–5), (3–2), and (1–0) lines, the gas kinetic temperature in the shocked region at the B1 position was estimated to be ∼170 K, which is a factor of ∼10 higher than that of the quiescent gas (Umemoto et al. 1999; Hirano & Taniguchi 2001). A remarkable correlation between the kinetic temperature and velocity dispersion of the CO J=3–2 emission along the lobe suggests that the molecular gas at the head of the bow-shock is indeed heated kinetically (Hirano & Taniguchi 2001).

In the shocked region, where the gas is significantly heated and compressed, various chemical reactions that cannot proceed in the cold and quiescent dark clouds

[1]Based on Gómez-Ruiz, Hirano, Leurini, Liu. The L1157 outflow imaged with the SMA, submitted to A&A.

are expected to be triggered off. Bachiller & Perez Gutierrez (1997) and Bachiller et al. (2001) surveyed molecular lines in the L1157 outflow, and found that molecules such as SiO, CH_3OH, H_2CO, HCN, CN, SO, and SO_2 are enhanced by at least an order of magnitude at the shocked region. In the blue lobe, molecular lines such as SiO, CH_3OH, and H_2CO mainly come from three regions labeled B2, B1, and B0 (Fig. 1). Furthermore, the spatial distributions of these shock-enhanced molecules differ from species to species; the SiO is remarkably enhanced at the B1 position, the CH_3OH is equally enhanced at both B1 and B2 positions, whereas HCO^+ and CN are enhanced in the region between the driving source and B1 position. This suggests that there is a stratification in the chemical composition of the shocked gas.

Millimeter interferometric observations by Benedettini et al. (2007) have resolved each emission structure (B0, B1, and B2) into a group of smaller scale clumps with a size of 0.02-0.04 pc. In addition, each emission structure also has its internal chemical stratification. At the B1 position, the HC_3N, HCN, CS, NH_3, and SiO lines are brighter in the eastern clumps, while the CH_3OH, OCS, and ^{34}SO lines are brighter in the western clumps. Interferometric observations have also suggested a temperature stratification within the B1 position, with the highest temperatures found towards the apex of the B1 bow shock (Codella et al. 2009).

Understanding the internal structure of the shocks in L1157 outflow is of particular interest in the light of the chemical studies currently underway with several facilities towards this remarkable object, for example Herschel key-program observations (Codella et al. 2010; Lefloch et al. 2010). In order to study the spatial and kinematic structure of the shocked gas at high angular resolution, we have mapped the blue lobe of the L1157 outflow at 1.3 mm using the Submillimeter Array (SMA).

2.2 Observations

2.2.1 SMA observations

The observations were carried out on 2004 August 10 with the SMA[2] on Mauna Kea, Hawaii (Ho et al. 2004). We used the compact-north array configuration that provided baselines ranging from 12.9 m to 109.5 m. The primary-beam size (HPBW) of the 6 m diameter antennas at 217 GHz was measured to be $\sim 54''$. The entire region of the southern blue lobe was covered by four pointings separated by $30''$ (Fig. 1). The spectral correlator covers 2 GHz bandwidth in each of the two sidebands separated by 10 GHz. The frequency coverage was from 216.6 to 218.6 GHz in the lower sideband (LSB) and from 226.6 to 228.6 GHz in the upper sideband (USB). Each band is divided into 24 "chunks" of 104 MHz width. We used a uniform spectral resolution of 406.25 kHz across an entire 2 GHz band. The corresponding

[2]The Submillimeter Array is a joint project between the Smithsonian Astrophysical Observatory and the Academia Sinica Institute of Astronomy and Astrophysics, and is funded by the Smithsonian Institution and the Academia Sinica.

Table 2.1: List of the detected transitions

Transition	Rest Frequency GHz	E_u K
SiO (5–4)	217.10498	31.3
H_2CO 3(0,3)–2(0,2)	218.22218	21.0
H_2CO 3(2,2)–2(2,1)	218.47561	68.1
CH_3OH 4(2,2)–3(1,2)E	218.44000	37.6

velocity resolution was 0.561 km s^{-1}. The visibility data were calibrated using the MIR software package, which was originally developed for Owens Valley Radio Observatory (Scoville et al. 1993) and adapted for the SMA [3]. The absolute flux density scale was determined from observations of Uranus. A pair of nearby compact radio sources 1927+739 and 1806+698 were used to calibrate relative amplitude and phase. We used Uranus to calibrate the bandpass.

The calibrated visibility data were imaged using MIRIAD, followed by a nonlinear joint deconvolution using the CLEAN-based algorithm, MOSSDI (Sault et al. 1996). We used natural weighting that provided a synthesized beam of $3.4'' \times 2.3''$ with a position angle of 63°. The rms noise level of the line data was 234 mJy $beam^{-1}$ at 1.3 km s^{-1} spectral resolution. Four molecular lines, SiO(5–4), CH_3OH 4(2,2)–3(1,2)E, H_2CO 3(0,3)–2(0,2) and H_2CO 3(2,2)–2(2,1), were detected above a 4σ level (see Table 2.1). All these lines were in the LSB, while no significant lines were detected in the USB. The continuum map was obtained by averaging the line-free chunks of the both sidebands. To improve the signal-to-noise ratio, the upper and lower sidebands were combined after the consistency of the images of two sidebands was confirmed. With natural weighting, the synthesized beam size was $3.4'' \times 2.2''$ with a position angle of 63°. The rms noise level of the 1.4 mm continuum map was 4.82 mJy $beam^{-1}$.

2.2.2 *Spitzer* IRAC observations

Archival data of all four IRAC bands (3.6μm, 4.5μm, 5.8μm, 8.0μm) were retrieved from Spitzer data base through Leopard. We have used the post-basic calibrated data (BCD) images for our analysis. The mean FWHM of the point respond functions are $1.66''$, $1.72''$, $1.88''$, and $1.98''$ for bands 1, 2, 3 and 4, respectively. The details of the IRAC observations of L1157 are described in Looney et al. (2007).

[3] http://cfa-www.harvard.edu/ cqi/mircook.html

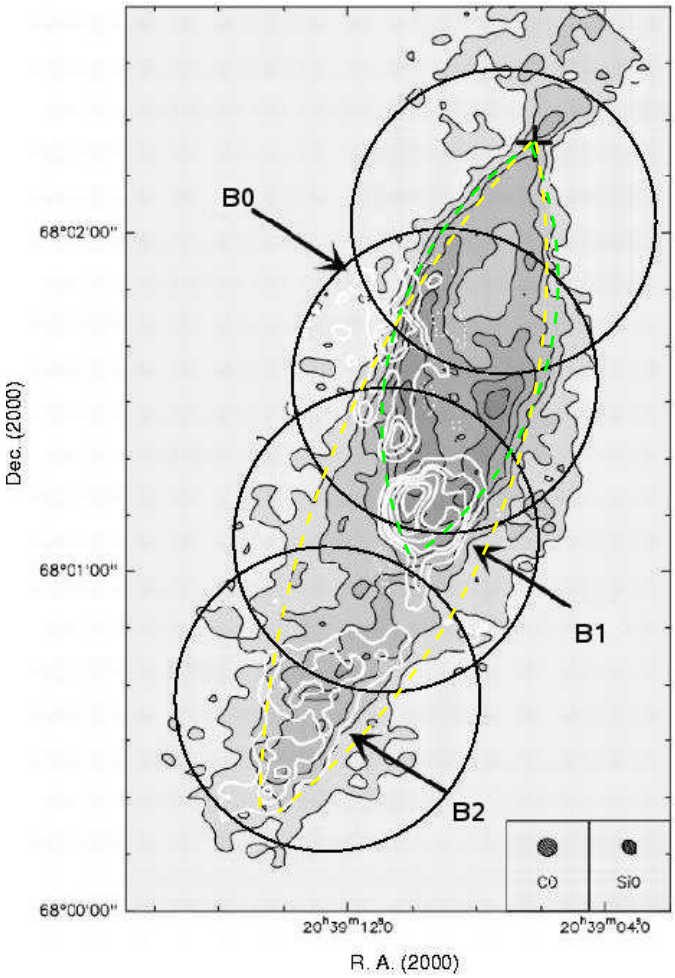

Figure 2.1: The half-power primary beams of the 4 fields observed with the SMA (circles) superposed on the integrated CO (1–0) emission in grey scale and SiO (2–1) emission in the white contours (from Gueth et al. 1998). The cross indicates the position of the protostar L1157-mm, $\alpha = 20^h39^m06.19^s$, $\delta = 68°02'15.9''$ (J2000.0) given by Gueth et al. (1997). The bottom-right corner shows the HPBW of Gueth et al. (1998) observations. Yellow and green ellipses indicate the location of the two cavities proposed by Gueth et al. (1997).

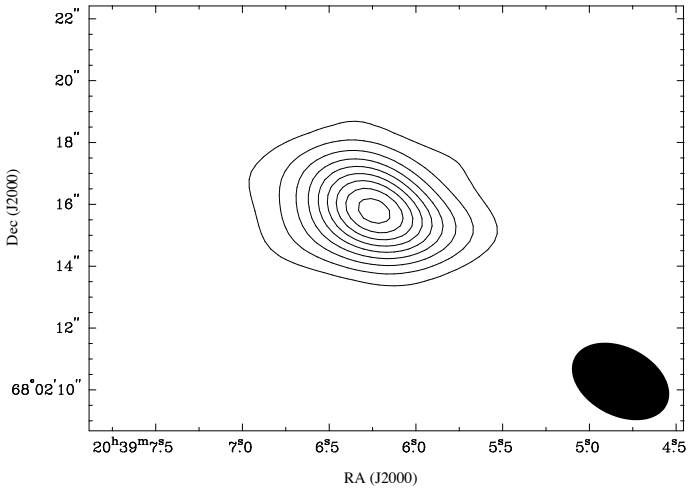

Figure 2.2: The 1.4 mm continuum emission from L1157-mm. First contour and contour spacing is 3σ (σ=4.82 mJy beam^{-1}), with the highest contour at 27σ. Black ellipse show the synthesized beam size (natural weighting). The parameters of a Gaussian fit to this image are presented in Table 2.2.

2.3 Results

2.3.1 Millimeter continuum emission

The continuum emission map is shown in Fig. 2.2. The continuum emission from the central source was detected at a level of $\sim 27\sigma$. The parameters of the continuum source, obtained through an elliptical Gaussian fit, are presented in Table 2.2. Previous observations at the same wavelength have presented by Beltrán et al. (2004) and Jørgensen et al. (2007). However, a comparison with these previous works is not always straightforward due to the different uv-coverage of the observations. Beltrán et al. (2004) detected an extended, low surface brightness, component that is not clearly seen in our map. We attribute this effect to the space filtering and lower sensitivity of our observations compared to Beltrán et al. (2004) observations, which included short-spacing observations with the IRAM-30m, and achieved a rms noise of 1.4 mJy beam^{-1}. Trying to compare with the compact component reported by Beltrán et al. (2004), we produce a map using the baselines longer than 40m. The synthesized beam size of this map is $2.8'' \times 1.7''$ with a position angle of 63°. An elliptical Gaussian fit to the image produce a source with an integrated flux of $\sim$130 mJy, which is then about 1.7 times higher than the compact component reported by Beltrán et al. (2004). This discrepancy can be explained by the fact that our larger baseline is about half the length of Beltrán et al. (2004) observations ($\sim$109 m compared to $\sim$288 m, respectively). On the other hand, the integrated flux of $\sim$130 mJy is consistent with the value given by Jørgensen et al. (2007) for the point source fit case ($\sim$120 mJy). We therefore conclude that our SMA observations reveal the compact source and part of the extended emission of L1157-mm.

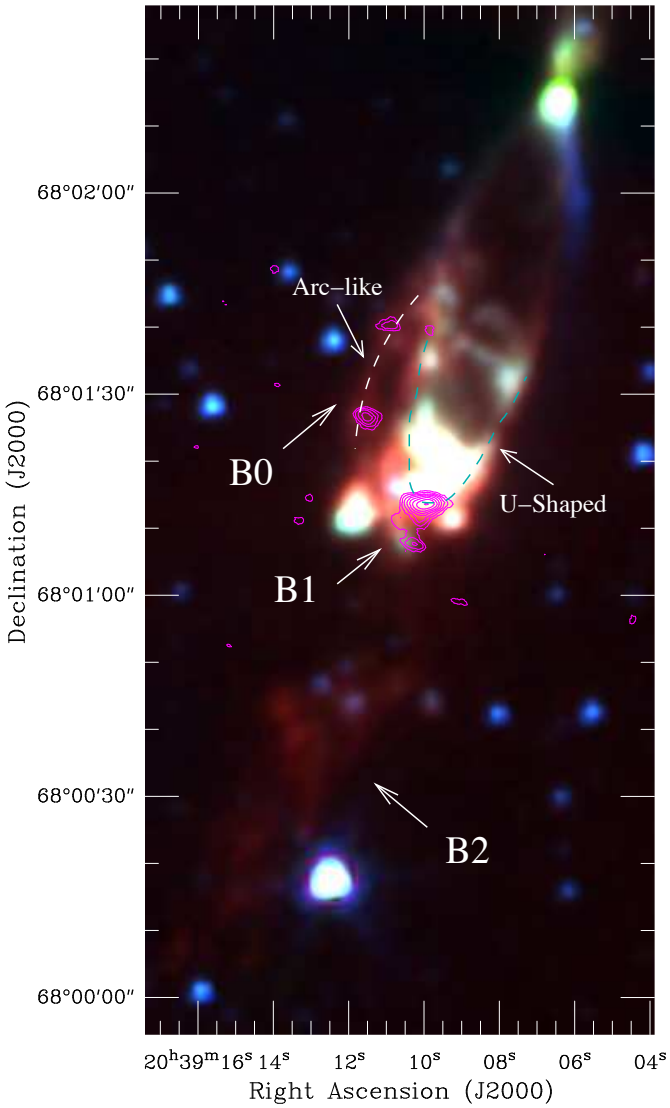

Figure 2.3: Overlaid of SiO (5–4) integrated emission (integrated from −16.7 to +4.1 km s^{-1}; magenta contours) and IRAC 3 color image (blue: 3.6μm, green: 4.5μm, red: 8.0μm). White and cyan dashed lines indicates the arc-like feature and the U-shaped structure, respectively, delineated by the mid-IR emission. SiO contours start at 3σ (σ=1.40 Jy beam^{-1} km s^{-1}) and then separated by steps of 1σ.

Table 2.2: Parameters of the 1.4 mm continuum source

Peak intensity (Jy/beam)	0.13±0.01
Total integrated flux (Jy)	0.211
R.A. (J2000)	$20^h39^m06.24^s$
DEC (J2000)	$68°02'15.8''$
Position angle (degrees)	73.86
Deconvolved Major axis (arcsec)	2.702
Deconvolved Minor axis (arcsec)	1.470
Deconvolved Position angle (degrees)	87.7

2.3.2 Mid-IR emission from the shocked gas

A detailed analysis by Takami et al. (2010) has shown that the mid-IR emission from this outflow is well explained by thermal H_2 emission excited by shocks. Figure 2 shows a 3 color image of IRAC bands 1, 2 and 4 of the blue lobe of the L1157 outflow, together with contours of the SiO (5–4) emission which will be described in the next section. The mid-IR emission delineates a U-shaped structure with an apex near the position of B1. The eastern and western walls of the U-shaped structure are connected by an emission ridge. To the east of the U-shaped structure there is another fainter arc-like feature. The mid-IR emission from the B2 position is much fainter than that of the B1 position.

The U-shaped structure in the mid-IR is confined inside the CO (1–0) cavity whose tip is B1. The blurred emission at B2 also has its counterpart in the CO (1–0) map. The location of the arc-like feature coincides with that of the B0 position. A comparison between the images of mid-IR and CO (1–0) implies that the arc-like feature corresponds to the eastern wall of the outer cavity produced by the B2 shock.

The difference in the Mid-IR color is considered to be due to the different excitation conditions (Takami et al. 2010). The mid-IR emission at the B2 position and the arc-like feature is dominated by the longer wavelength component seen in the red color. This suggest that the excitation conditions of these two regions are rather low because of the lower temperature and/or density. Indeed this is confirmed by H_2 rotational line studies: the temperature derived from the H_2 line is lower than 300 K toward the arc-like feature, which is significantly lower than 1400 K at the tip of the U-shaped structure (Nisini et al. 2010).

2.3.3 Molecular line emission observed with the SMA

SiO (5–4)

The SiO 5–4 emission was detected in the velocity range from -16.7 km/s to +4.1 km/s. Most of the SiO 5–4 emission observed with the SMA is blue-shifted with respect to the cloud systemic velocity of +2.7 km/s. The total integrated intensity map is shown in Fig. 2.3, and velocity channel map at 2.6 km/s interval is presented in Fig. 2.4. The total integrated intensity map shows that the SiO

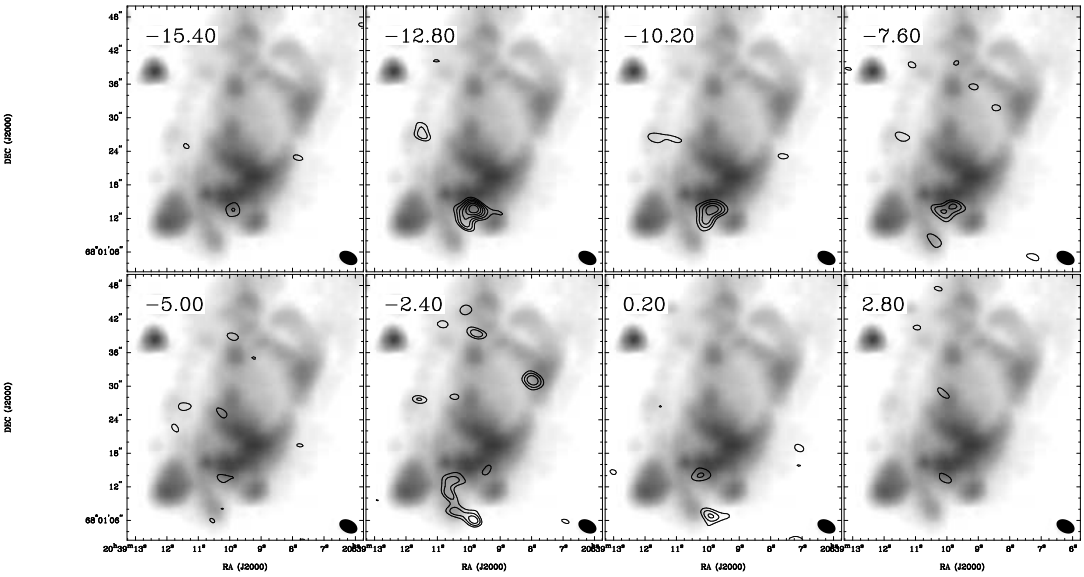

Figure 2.4: The SiO (5–4) emission (contours) in channel maps of 2.6 km s^{-1} width, overlaid on the 4.5μm emission from IRAC/Spitzer. SiO contours start at 3σ (σ=0.189 Jy beam^{-1} km s^{-1}) and then separated by steps of 1σ up to a value of 8σ. The central velocity of each channel map is indicated in upper left, while the ellipse in the lower right shows the synthesized beam.

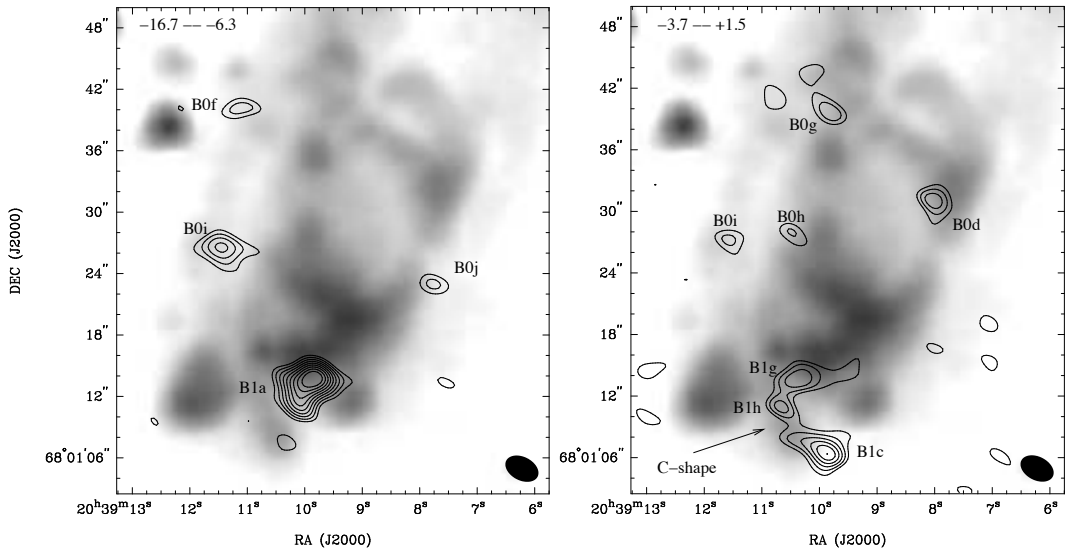

Figure 2.5: The SiO(5–4) emission in the blue-lobe of L1157 outflow integrated in two velocity ranges. High velocity range (left panel) is integrated from -16.7 to -6.3 km s^{-1}, while low velocity range (right panel) from -3.7 to +1.5 km s^{-1}. The velocity range is indicated in the upper left corner of each panel. Contours start at 3σ (σ = 0.985 Jy beam^{-1} for high velocity; σ = 0.648 Jy beam^{-1} for low velocity) and then separated by steps of 1σ. Grey scale represents the 4.5μm emission from IRAC/Spitzer.

(5–4) emission is brightest at the B1 position, which correspond to the apex of the U-shaped structure seen in the mid-IR. There are two compact SiO clumps along the faint arc-like feature to the east of the B0 position. Notably, no significant emission was detected at the position of B2, although the SiO (5–4) emission at this position was detected in the single-dish telescope observations of Bachiller et al. (2001). Our observations with the shortest projected baseline of 9.3 kλ were not able to recover the structure larger than $\sim 27''$, while the emission component at the B2 position in the single-dish map is extended more than $20''$. Furthermore, the r.m.s. noise level of our map is $\sim$4.6 K km s^{-1}, which is not sensitive enough to detect the SiO (5–4) emission at the B2 position, the peak intensity of which is $\sim$6 K km s^{-1} in the single-dish map. Therefore this indicates that the SiO (5–4) emission from B2 position is spatially extended with low surface brightness and thus filtered out in our data.

The velocity channel map reveals that the most prominent clump at the B1 position appears in the velocity channels from -15.4 km/s to -7.6 km/s (the corresponding velocity range is from -16.7 km/s to -6.3 km/s). On the other hand, the SiO 5–4 emission from the B1 position is more extended in the channels of -2.4 km/s and 0.2 km/s (the velocity range is from -3.7 km/s to +1.5 km/s). In Figure 5, we display the spatial distributions of the SiO in the velocity ranges from -16.7 km/s to -6.3 km/s and from -3.7 to +1.5 km/s. In these maps, all the SiO clumps detected above the 4-sigma level are labeled. In Table 2.3 we list the clumps and their positions obtained by a two dimensional Gaussian fit. The list of clumps is shown in decreasing order of declination. We use the same notation as reported by Benedettini et al. (2007) when our clumps are coincident within $4''$ of their positions. Otherwise we name the clumps by following the sequence of letters for either B0 or B1. Three clumps shown in the map of the total integrated intensity (Fig. 2.3) appear in the high velocity range (labeled B0f, B0i, and B1a). In the low velocity range, the most prominent feature is the C-shaped structure that consist of three clumps labeled B1c, B1g, and B1h. This C-shaped feature is surrounding the brightest clump B1a seen in the high velocity range. In addition, two marginally detected (4 σ) clumps labeled B0g and B0h are on the eastern wall, and the clump B0d is on the western wall of the mid-IR U-shaped structure.

The SiO 5-4 emission from B1 position has also been observed with the Plateau de Bure Interferometer (PdBI) by Gueth et al. (1998). The overall features observed with the SMA are consistent with those of the PdBI map made with a similar angular resolution, in particular the peak flux ($\sim$1.5 Jy beam^{-1}) is in good agreement with the PdBI observations. The exception is the linear structure ahead of B1c and the westward extension of the B1c clump. These structures are seen in the PdBI map but not in the SMA map, probably because of the insufficient sensitivity (for a 2.6 km s^{-1} velocity bin, $\sim$190 mJy beam^{-1} compared to $\sim$50 mJy beam^{-1} of the PdBI observations) and different u-v coverage of the SMA observations.

A number of observations have proven the particular chemical richness of the B1 position in L1157. Thus, the physical characterization at such position is important in order to account for kinematic effects in the chemical models that try to explain

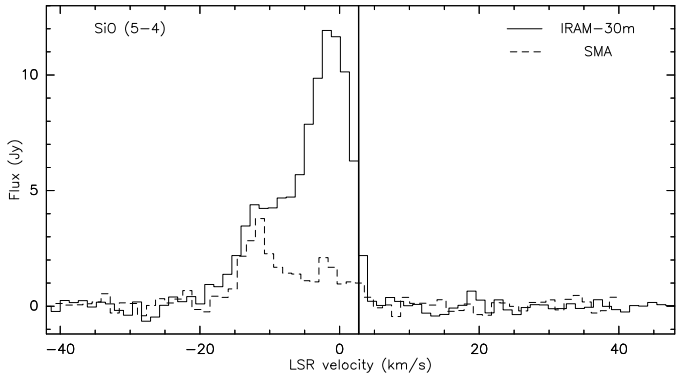

Figure 2.6: SiO (5–4) spectra at the B1 position observed by IRAM 30m telescope (thin solid line) and the SMA (dashed line). Cloud velocity is indicated by a thick vertical line (V_{LSR}=2.7 km s^{-1}). The SMA observations were convolved to the 11 arcsec resolution so as to match the beam of the IRAM 30m telescope. Spectral resolution is 1.3 km s^{-1} in both cases.

the emission from different molecular species (e.g. Viti et al. 2011). Therefore, most of the analysis of the SiO emission presented in the following sections are mainly focused on the B1 position. With the aim to estimate the missing flux at the B1 position, we have compared the single-dish spectrum taken with the IRAM-30m (provided by M. Tafalla) with our SMA spectrum convolved to the same angular resolution (11″). As shown in Fig. 2.6, the single-dish spectrum in B1 peaks at V_{LSR} ∼-2 km s^{-1}. On the other hand, the spectrum obtained with the SMA peaks at V_{LSR} ∼-11 km s^{-1}, which is also seen as a bump in the single-dish spectrum. It is found that the SiO flux recovered by the SMA was only ∼10% in the velocity range from -10.3 to +2.6 km/s, suggesting that most of the SiO emission in this velocity range comes from spatially extended region and filtered out in the current SMA map. In contrast, the SMA recovered up to ∼80% of the SiO flux in the velocity range from -15.3 to -11.4 km/s. This implies that most of the SiO emission in this velocity range arises from the compact clump, B1a. Therefore, our SMA observations peaks at -11 km s^{-1} instead of ∼-2 km s^{-1}, as the IRAM-30m observations, because most of the low-velocity emission is filtered out in the SMA map.

H_2CO and CH_3OH

Two formaldehyde (H_2CO) lines were detected in the LSB (see Table 2.1). The H_2CO 3(0,3)–2(0,2) line was detected in the velocity range from -3.7 km s^{-1} to +4.1 km s^{-1}, while the H_2CO 3(2,2)–2(2,1) line was detected from -1.1 to +4.1 km s^{-1}. In Fig. 2.7a,b we show the total integrated emission of both H_2CO transitions, overlaid on the IRAC 4.5μm emission. In order to improve the sensitivity, we have convolved both maps to 5″×5″. As in the case of SiO, there is no significant H_2CO emission from B2 position. The spatial distribution of the H_2CO 3(0,3)–2(0,2) emission is similar to that of the H_2CO 3(2,2)–2(2,1), except the elongated structure along the

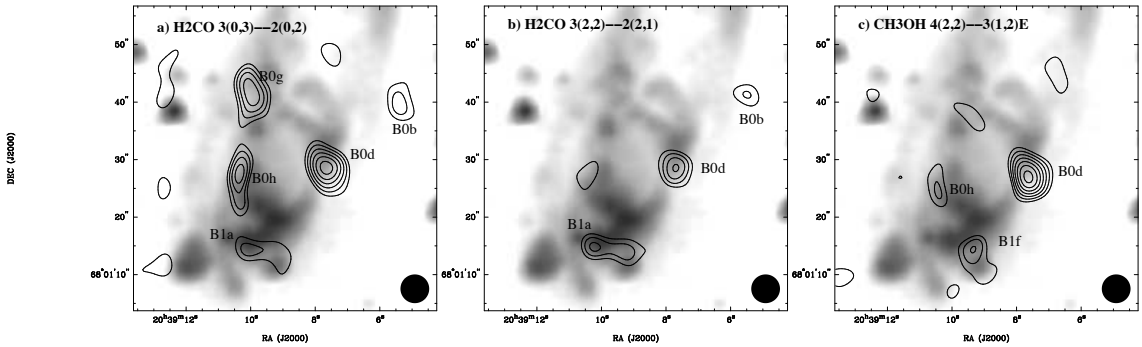

Figure 2.7: Total integrated emission of the (a) H_2CO 3(0,3)–2(0,2), (b) H_2CO 3(2,2)–2(2,1), and (c) CH_3OH 4(2,2)–3(1,2)E transitions. In all panels, contours start at 3σ (σ=1.35, 0.50, 0.55 Jy beam^{-1} km s^{-1}, respectively) and then separated by steps of 1 σ. The grey scale represents the 4.5μm emission from *Spitzer*/IRAC. All maps are convolved to $5''\times5''$ (beam is shown at the bottom-right of each panel).

Table 2.3: Clump positions

Clump	R.A.	Dec	Molecular tracer[a]		
	J2000	J2000	SiO	H_2CO	CH_3OH
B0b*	20:39:05.5	68:01:40	N	Y	N
B0f	20:39:10.9	68:01:40	Y	N	N
B0g	20:39:09.8	68:01:39	Y	N	N
B0d*	20:39:07.9	68:01:30	Y	Y	Y
B0h	20:39:10.4	68:01:27	Y	Y	Y
B0i	20:39:11.5	68:01:27	Y	N	N
B0j	20:39:07.7	68:01:22	Y	N	N
B1g	20:39:10.3	68:01:13	Y	N	N
B1f$^+$	20:39:09.0	68:01:13	N	Y	Y
B1a*	20:39:10.0	68:01:12	Y	Y	Y
B1h	20:39:10.6	68:01:11	Y	N	N
B1c*	20:39:09.9	68:01:06	Y	N	N

* Reported also by Benedettini et al. (2007).
$^+$ Reported also by Codella et al. (2009).

[a]Detections above 4 σ marked Y, while non-detections marked N.

eastern wall that is barely seen in the H_2CO 3(2,2)–2(2,1). The energy level in the upper state of the H_2CO 3(0,3)–2(0,2) transition is 21 K, while for the H_2CO 3(2,2)–2(2,1) it is 68 K. Therefore, difference in the spatial distribution between the two transitions of H_2CO suggest that the excitation condition of the elongated structure in the eastern wall is lower than that of the B0d clump.

The H_2CO emission clumps detected above the 4σ level are labeled in Figure 2.7 and their positions listed in Table 2.3. We have also used the same notation as reported by Benedettini et al. (2007) and Codella et al. (2009) when our clumps are coincident within $4''$ of their positions, otherwise define the new clumps in the same way as we have proceeded for SiO. As shown in Fig. 2.7a and 2.8, an elongated H_2CO 3(0,3)–2(0,2) emission feature, well traces the eastern wall (clumps B0g and B0h) and the apex (clump B1a) of the mid-IR U-shaped structure. A Similar elongated feature was also seen in the HC_3N (11–10) map of Benedettini et al. (2007) and the CH_3CN map of Codella et al. (2009). The brightest H_2CO emission component is seen in the western wall. This component is likely to be the counterpart of the B0d clump seen in the HCN (1–0) and CH_3OH (2_K–1_K) maps of Benedettini et al. (2007). The H_2CO clump at $\sim 15''$ northwest of B0d is considered to be the counterpart of the B0b clump in the CH_3OH (2_K–1_K).

The CH_3OH 4(2,2)–3(1,2)E line emission was found in a velocity range from $\sim$ -3.7 km s^{-1} to +1.5 km s^{-1}. The CH_3OH total integrated intensity map shown in Figure 2.7c was also convolved to the $5''\times5''$ resolution in order to improve the signal-to-noise ratio. The overall distribution of the CH_3OH 4(2,2)–3(1,2)E emission is similar to that of the H_2CO 3(2,2)–2(2,1). The CH_3OH emission is brightest in the B0d clump, but also showing emission at B0h and B1f. No CH_3OH emission was detected at the B2 position. The clumps detected above a 4σ level in the CH_3OH 4(2,2)–3(1,2)E line are also listed in Table 2.3.

2.4 Discussion

2.4.1 Physical conditions of the clumps

The SiO high velocity clumps

Using the line ratio between the SiO (5–4) and SiO (2–1) transitions we have derived the physical conditions of the gas in the high-velocity clumps. We have chosen the high-velocity range for the analysis since this velocity range is less affected by the missing flux. This analysis has been done at B0i and B1a, in which the SiO (5–4) emission was detected above 5σ level. For our calculations we use the interferometric SiO (2–1) observations from Zhang et al. (2000), with a synthesized beam of $9.5''\times8.0''$. We note that the analysis using the multi-transition SiO lines has been done by Nisini et al. (2007). However, the analysis of Nisini et al. (2007) used the single-dish data with $\sim27''$ resolution, and obtained the line ratio using the total integrated intensity including the low-velocity component. On the other hand, our analysis used higher resolution data, and focused on the high-velocity

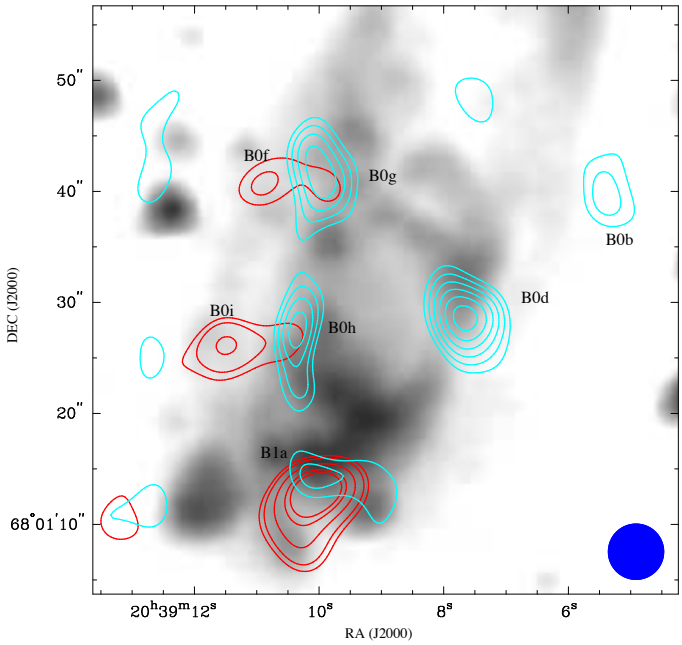

Figure 2.8: Total integrated H_2CO 3(0,3)–2(0,2) emission (cyan; from -3.7 to +4.1 km s^{-1}) and the SiO (5–4) emission (red; from -16.7 to +4.1 km s^{-1}). Contours start at 3σ (σ=1.35 and 2.60 Jy $beam^{-1}$ km s^{-1}, respectively) and then separated by steps of 1 σ. The grey scale represents the 4.5μm emission from *Spitzer*/IRAC. The maps are convolved to 5″×5″ (beam shown at the bottom-right).

component.

Since the interferometric SiO (2–1) observations agreed to better than 20% with the single-dish results, Zhang et al. (2000) concluded that most of the SiO (2–1) flux was recovered with the interferometer. Therefore we do not take into account the effect of the missing flux in this transition. Our SiO (5–4) observations were convolved to the angular resolution of the SiO (2–1) data (i.e. 9.5″×8.0″). In Fig. 2.9 we show the SiO (5–4) and (2–1) spectra at the position of clumps B0i and B1a. The high-velocity range in clump B1a is defined as the velocity interval in which most of the single-dish SiO (5–4) emission is recovered by our SMA observations, i.e. from -15.3 to -11.4 km s^{-1}. As shown in Fig. 2.9, the SiO (5–4) emission is much brighter than the SiO (2-1) in this velocity range. For the B0i clump we assume the same velocity range as for the B1a clumps, i.e. from -15.3 to -11.4 km s^{-1}.

We use the non-LTE program RADEX (van der Tak et al. 2007) in the LVG approximation and plane parallel geometry to model the (2–1)/(5–4) ratios. Using the RADEX offline distribution[4] we estimated the kinetic temperature (T_{kin}) and/or the volume density (n) from the observed line ratio. As input parameters we use the CMB temperature, 2.73 K, as the background radiation field, and the line widths as defined previously for the high-velocity ranges. In order to constrain the column density, we use also the observed brightness temperature of the SiO (5–4) emission.

[4]http://www.sron.rug.nl/∼vdtak/radex/

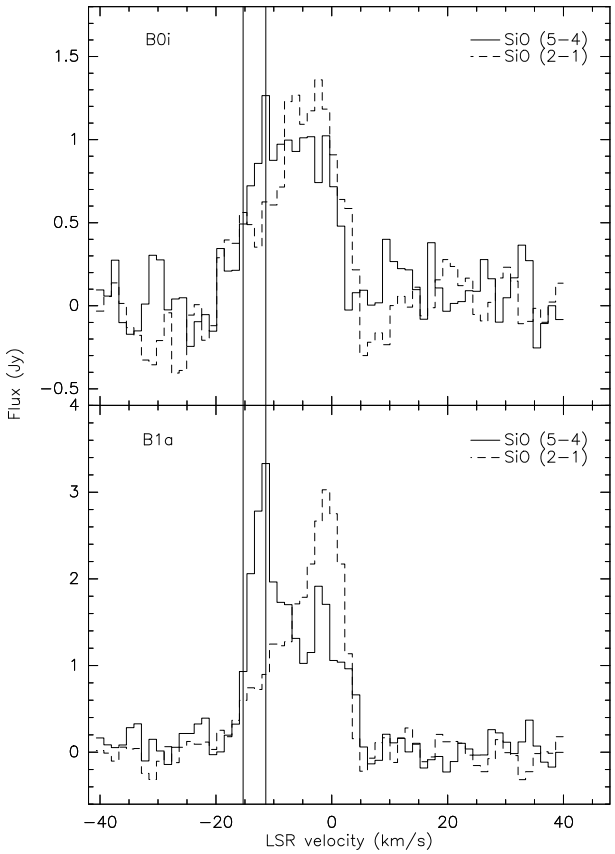

Figure 2.9: SiO spectra at B0i and B1a positions. SiO (5–4) has been convolved to the angular resolution of the SiO (2–1) observations (i.e. 9.5×8.0 arcsec). Thick vertical line indicates the high-velocity ranges on which the analysis has been done, from -16.7 to -6.3 km s^{-1} for B0i and from -15.3 to -11.4 km s^{-1} for B1a.

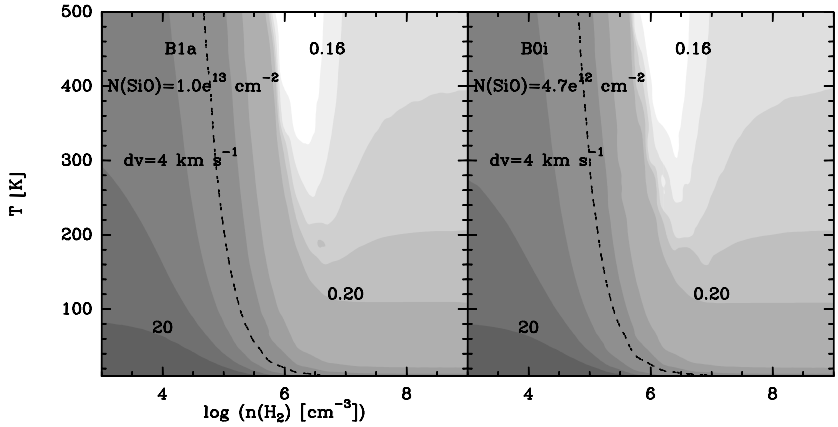

Figure 2.10: SiO (2–1)/(5–4) ratio as a function of T_{kin} and $n(H_2)$ from the LVG modeling (grey scale). The panels show the case of B1a and B0i. The N(SiO) is the best solution obtained from the simultaneous fit of the ratio and the SiO (5–4) brightness temperature. The observed line ratio (in brightness temperature: 2.3 at B1a and 1.8 at B0i) is shown as a dashed curve in each panel. The line ratios plotted in grey are 0.16, 0.17 0.18, 0.2, 0.5, 1, 5, 10, 20 (some of them indicated with numbers).

Then, by running the LVG for different column densities, we find the best column density that better match with the velocity integrated brightness temperature and line ratio.

In Fig. 2.10 we show the LVG results for the two cases of interest. In the temperature versus density plots of Fig. 2.10, the (2–1)/(5–4) ratio does not strongly depend on the temperature (unless the density exceeds 10^7 cm^{-3}), but it is sensitive to the density. Therefore a strong constrain can not be given for temperature but for density. We found that the observed ratios yield similar solutions for both positions, with lower limits n >5×10^4 cm^{-3}, T_{kin} > 10 K. We also found that these results do not change considerably by extending the velocity range up to ∼- 6 km s^{-1} (e.g. the high-velocity range shown in Fig. 5). Nisini et al. (2007), by using the (8–7)/(5–4) ratio in the high velocity range, found that the ratio was consistent with a density of ∼5×10^6 cm^{-3}. Therefore, these results from Nisini et al. (2007) are similar to our results from the (2–1)/(5–4) ratio in the region of low temperatures shown in Fig. 2.10. These results show that indeed the high-velocity gas from the B1a position consist of relatively high-density gas. We note that such high densities are similar to the values found in outflows with EHV emission, for example the EHV bullets in L1448C for which measurements show that they consist of clumps with n ∼0.8-1×10^6 cm^{-3} (e.g., Nisini et al. 2007). A high density of >10^6 cm^{-3} has also been observed in the EHV jet of HH211 (Hirano et al. 2006; Palau et al. 2006). This similarity with the density of EHV bullets may suggest that the high velocity emission in L1157 may have a similar origin.

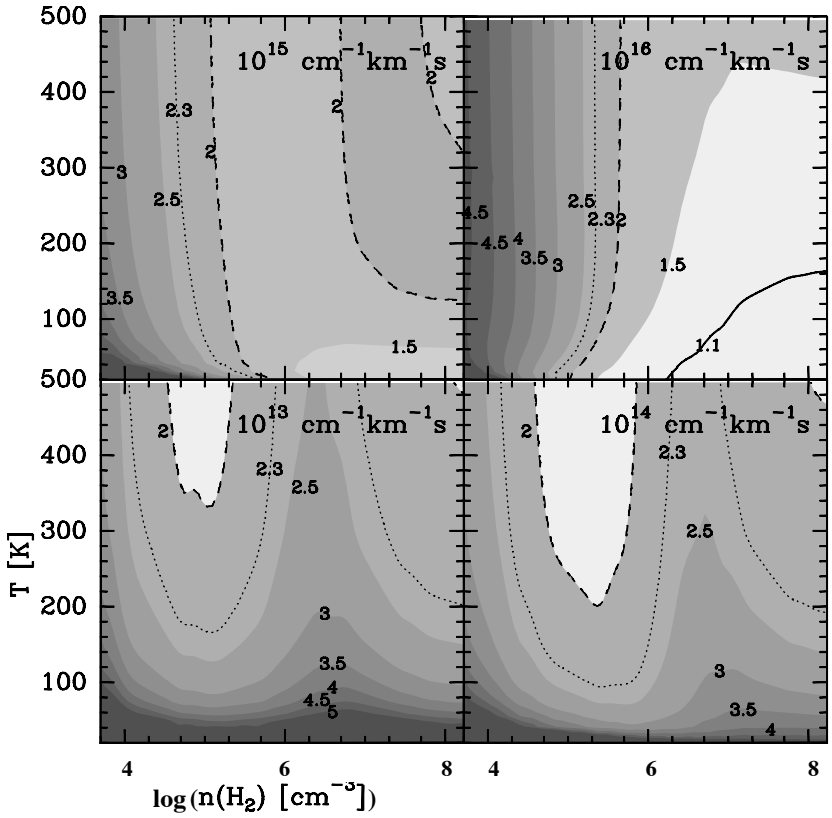

Figure 2.11: LVG for the H_2CO emission in L1157. The H_2CO 3(0,3)–2(0,2)/ 3(2,2)–2(2,1) observed ratios are: 1.1 (solid), 2.0 (dashed), and 2.3 (dotted). Each panel show the N/Δv parameter for which the LVG was run (taking Δv=1 km s^{-1}). In grey scale different (2-1)/(5-4) ratios are plotted, which values are indicated by the numbers in black.

H_2CO emission

The H_2CO 3(0,3)–2(0,2)/3(2,2)–2(2,1) ratio is sensitive to temperature in the range of 50–200 K (van Dishoeck et al. 1993; Mangum & Wootten 1993). These two transitions were detected in the clumps B0h, B0d, and B1a. The line ratios, 3(0,3)–2(0,2)/3(2,2)–2(2,1), averaged over a 5" beam, measured at the center of these clumps, are 2.3±0.8 in B0h, 2.0±0.4 in B0d, and 1.1±0.4 in B1a. It is likely that both transition should have significant missing flux. Since there is no available single-dish data for these transitions, it is difficult to estimate how much flux was missed. However, since the two line transitions were observed simultaneously with the same uv sampling, the line ratio can be reliable for spatially compact components. In general, the missing flux in the lower excitation line is expected to be larger than that in the higher excitation line, because the lower excitation line is more extended than the higher excitation line. Therefore, the line ratio derived here can be a lower limit, if the source is extended.

We have run LVG models to reproduce the H_2CO 3(0,3)–2(0,2)/3(2,2)–2(2,1) line ratio observed at these three clumps. In order to show the general trend of the results of the LVG for the H_2CO case, in Fig. 2.11 we present the temperature versus density plot for different N/Δv parameters (with Δv=1 km s^{-1}). As seen from the figure, the ratios are sensitive to temperature for N/Δv between 10^{13} and 10^{14} cm^{-1} km^{-1} s. On the other hand, the line ratio is sensitive to densities for N/Δv between 10^{15} and 10^{16} cm^{-1} km^{-1} s. Assuming a value of the column density of the order of 10^{14} cm^{-2} (e.g. Bachiller & Perez Gutierrez 1997) and a linewidth of 4 km s^{-1}, the H_2CO line ratio suggests that the gas temperature in B0d and B0h to be $>$ 200 K and $>$ 100K, respectively. On the other hand, the line ratio at B1a position has only solution in the extreme model with N/Δv of 10^{16} cm^{-1} km^{-1} s, which then turns into a value of N which is two orders of magnitude higher than the values derived from the single-dish observations. Such a low value of line ratio suggests that B1a clump is spatially extended. This clump is not clearly seen in the H_2CO 3(0,3)–2(0,2) map shown in Figure 2.7. This also support that the emission in B1a clump is dominated by the spatially extended component.

2.4.2 The SiO emission at B1

Figure 2.12 displays a close-up view of the high- and low-velocity SiO emission at the B1 position, taken from Fig.2.5. It is seen that the high-velocity clump B1a is surrounded by three low-velocity clumps, with two of them (B1c and B1h) located downstream of B1a. Indeed the clumpy structure of the low-velocity SiO emission at the B1 position is a remarkable finding of the present observations. The position-velocity (PV) diagram along the axis of the C2 cavity (P.A. 161 deg.) also exhibits the higher velocity emission at the position closest to the protostar and the lower velocity in the downstream (Figure 2.13). Such a velocity structure is different from that expected in a single bow shock, in which the highest velocity appears at the tip followed by a low-velocity "wake" or "bow wing" (e.g., Lee et al. 2000). In addition,

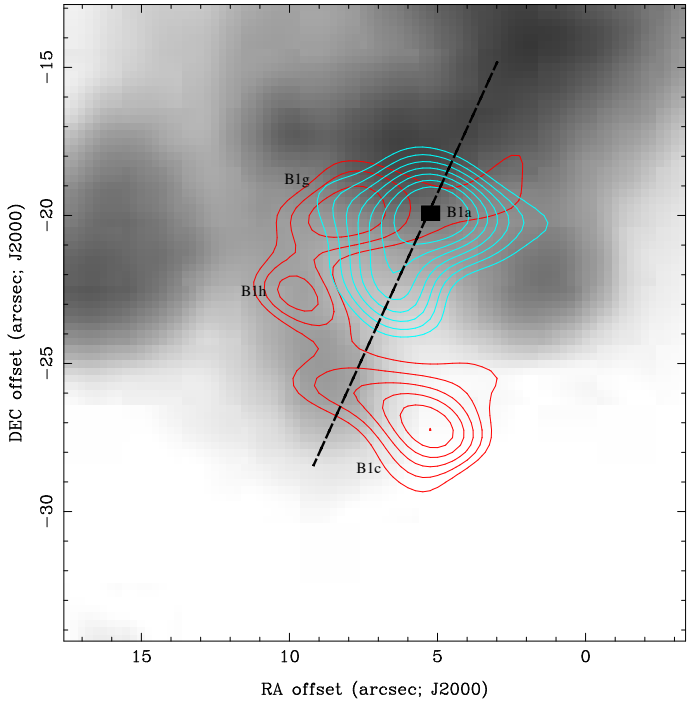

Figure 2.12: Low velocity (red contours) and high velocity (cyan contours) SiO(5–4) emission at the B1 position, overlaid on the 4.5μm emission from IRAC/Spitzer. Dashed line indicates the axis (P.A. of 161 degrees) of the C2 cavity, on which the PV diagram in Figure 2.13 was made. Black square shows the reference position (i.e. offset=0) of PV diagram in Figure 2.13.

the PV plot of a single bow shock produced by a jet whose axis is close to the plane of the sky (as is the case for L1157 outflow) should narrow considerably towards distances closer to the protostar (Lee et al. 2000), which is not exactly the case of the PV plot in Fig.2.13 that still show a broad range of velocities at such distances. It is likely that the high-velocity clump B1a is kinetically independent from the low-velocity ones. As discussed previously, the low velocity clumps are likely to be the part of the spatially extended structure, while the high velocity clump is a distinct and compact structure. The idea of the low- and high-velocity molecular emission at the B1 position as two different phases has been recently explored by the models of Viti et al. (2011) for the water and ammonia emission: a first phase characterized by a pre-existing (to the shock) clump, and a second phase with the action of the shock. Our observations may give support to this alternative explanation for the molecular emission at this position, however the two phases model applied to the specific case of SiO is needed to test whether this is also a possible scenario for the SiO emission.

The line profile of the high-velocity component observed with the SMA shows a maximum intensity close to the highest blue-shifted velocity with a gradual wing toward the lower velocity (Figure 2.6). This line profile is similar to those produced by the C-type shock models calculated by Schilke et al. (1997). The line profile also resemble the model calculations by Jiménez-Serra et al. (2009) for a single shock with a few hundred years. This kind of line profiles are observed in the extremely high velocity (EHV) bullets of jet sources such as L1448C and HH211 (e.g., Nisini et al. 2007). Such bullets can be related with the early stages of shocks in outflows, since they have a short dynamical time (they are close to the central source), and therefore consistent with the shock calculations. The similarity with the line profiles in EHV jets may suggest that the B1a clump is the possible counterpart of the EHV knots seen in outflows like L1448C. An additional support to this suggestion is the size and mass of the high velocity clump. Since $\sim$ 80% flux of the high-velocity SiO emission is recovered with the SMA at B1 position, the size of the knot is considered to be that of clump B1a. Assuming that the clump is a spheroid with semi-axes of 100 AU x 500 AU x 500 AU (as measured from a Gaussian fit the B1a clump), and that the density is constant, n = 10^6 cm^{-3} (as derived from the LVG analysis for a kinetic temperature of about 30 K, i.e. $\sim$E$_{up}$ of the SiO 5–4 transition), the corresponding mass is $\sim 6\times10^{-4}$ M$_\odot$. The mass of this clump is therefore close to that reported by Nisini et al. (2007) in L1448C high-velocity bullets (i.e. 3×10^{-3} M$_\odot$). In summary, the position-velocity distribution, the line profile and mass estimation of the B1a clump as found with our SMA observations suggest that it may be related with a single shock, possibly the counterpart of the EHV knots observed in jet sources such as L1448C.

In the case of L1157, there is no jet-like EHV feature along the axis of the lobe. This is probably because the direction of the jet changes more significantly as compared to the cases of L1448C and HH211, and therefore the internal working surfaces that characterize narrow EHV jets can not be produced (Raga et al. 1990). The high-velocity SiO clumps including the B1a clump at the apex of the C2 cavity

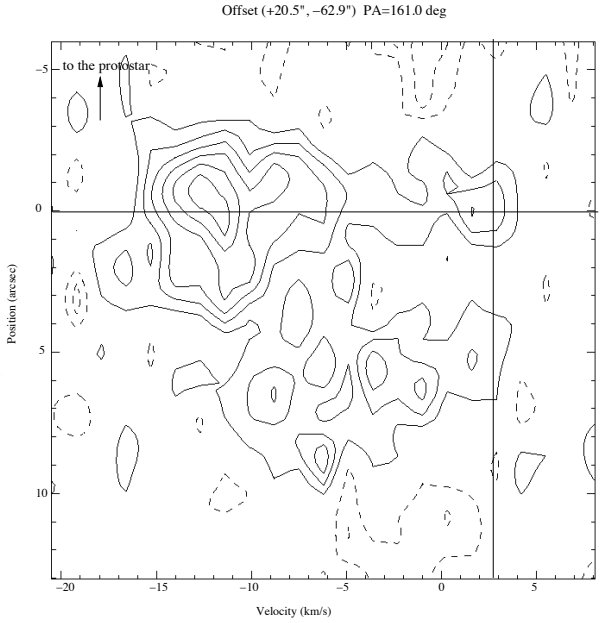

Figure 2.13: Position-velocity diagram of the SiO(5–4) emission at the position of B1 clump. Offset is measured from the center of the B1a clump. The cut is along the axis of the C2 cavity. Vertical line indicates the cloud velocity (V_{LSR}= 2.7 km s^{-1}), while horizontal line the reference position (offset=0).

and B0i and B0f along the arc-like feature can be explained in the context of the precessing jet proposed by Bachiller et al. (2001). This model predicts a S-shaped point-symmetry, which consists of three or four independent episodes of mass ejection from the central source. The position of the SiO (5–4) clumps B0f, B0i, and B1a, are consistent with the independent ejection events produced by the precessing jet model. On the other hand, the low-velocity component that dominates the single-dish spectrum is spatially extended and is likely to be ambient quiescent material accelerated by the shock. The line profile of the single-dish spectrum, which shows a peak at the systemic velocity and a gradual blue wing, suggests that only a small fraction of the gas is accelerated to the high velocities. Although this scenario is speculative, the morphology of the outflow and the locations of the shocks support this possibility.

2.4.3 The SiO, H_2CO, and CH_3OH spatial distribution

H_2CO and CH_3OH are known to be formed efficiently on grain surfaces through successive hydrogenation (e.g., Tielens & Whittet 1997; Charnley et al. 1997; Watanabe & Kouchi 2002). Observationally, H2CO and CH3OH show significant abundance enhancement, which is likely to be originated from evaporation of grain mantles (e.g., Bachiller et al. 1995; Avery & Chiao 1996; Schöier et al. 2004). As shown in Fig. 2.7, the two H_2CO transitions and the CH_3OH 4(2,2)–3(1,2)E line exhibit

a similar spatial distribution, that is the walls of the U-shaped feature, suggesting that the chemistry of both molecular species are linked. However, the detailed structure within this cavity shows differences from one molecular tracer to the other. For example, if we compare the spatial distribution of the CH_3OH and H_2CO lines with similar energy levels (i.e. CH_3OH 4(2,2)–3(1,2) with $E_u \sim 38$ K and H_2CO 3(0,3)–2(0,2) with $E_u = 21$ K), the CH_3OH tends to be to the west and the H_2CO tends to be to the east of the apex.

The abundance of the SiO molecule is also expected to be enhanced, in this case by the sputtering from the grains (cores or mantles) of silicon-bearing species that are injected into the gas phase in the form of neutral Si, SiO, SiO_2, or SiH_4 (Schilke et al. 1997; Gusdorf et al. 2008a). In the Fig. 2.8a we show the total integrated emission of the SiO (5–4) and H_2CO 3(0,3)–2(0,2) transitions, convolved to the same angular resolution of 5″. From Fig.2.8 we see that the spatial distribution of SiO is different from that of the H_2CO (and therefore to that of CH_3OH, since its distribution is similar to H_2CO). The most prominent SiO clumps are located at the apex of the U-shaped structure, and along the faint mid-IR arc-like feature outside of the U-shaped structure. On the other hand, the H_2CO emission is located almost exclusively along the U-shaped structure. Another important fact, apart from the different spacial distribution, is that the high-velocity SiO clumps (B0f, B0i, B1a) dominate the total integrated emission, contrary to the H_2CO (and also CH_3OH) emission which is only observed at low velocities.

Since the H_2CO and CH_3OH lines appear in the low-velocity range and trace well the mid-IR U-shaped structure, these lines are likely to come from the wing of the bow shock whose tip is a bright SiO clump, B1a. The velocity structure seen at the tip of the bow shock can be explained if high-velocity gas plunge into the slow-moving material in the downstream. On the other hand, the SiO clumps, B0f and B0i, which are located outside of the U-shaped structure, are likely to be produced by the different ejection event.

2.5 Summary and Conclusions

The principal results of the SMA observations at 1.3 mm towards the blue-lobe of the L1157 outflow are summarized as follows:

- Four molecular transitions, SiO (5-4), H_2CO 3(0,3)–2(0,2), H_2CO 3(2,2)–2(2,1), and CH_3OH 4(2,2)–3(1,2)E were detected at B1 and B0 positions in the blue lobe. None of these lines shows significant emission at the protostellar position and the B2 position.

- The SiO (5-4) emission is brightest at the B1 position, which corresponds to the apex of the U-shaped structure seen in the mid-IR. There are two compact SiO clumps along the mid-IR arc-like feature to the east of the B0 position.

- The H_2CO and CH_3OH lines trace (or delineate) the U-shaped structure. The overall distribution of both species are similar.

- At the B1 position, the SMA recovered 80% of the single-dish flux in the high-velocity range, suggesting that the high velocity emission is confined in a compact clump of $\sim$ 2000×1000 AU size. On the other hand, the SMA recovered only ∼10% of the flux in the low-velocity range. This indicates that the low-velocity SiO is spatially extended.

- The velocity structure around the B1 position is different from that expected in a single bow shock. It is likely that the high-velocity clump, B1a, is kinetically independent from the low velocity ones. The low-velocity clumps are likely to be part of the spatially extended structure that dominates the single-dish observations, and possibly related with an older shock.

- The physical parameters determined for the high velocity SiO emission confirm that the high-velocity clumps consist of high density gas (n>5×10^4 cm^{-3}). Such high densities are similar to the ones reported with outflows with EHV bullets and therefore suggesting a similar origin.

Chapter 3

Warm gas in protostellar outflows I. Flows from the low-mass protostars in L1448 and HH211[1]

3.1 Introduction

Bipolar molecular outflows are a common phenomenon accompanying the formation of both low- and high- mass stars (Arce et al. 2007). The perturbation produced when outflow momentum and energy are injected into the material surrounding the protostar has an impact on the mass assembly process. Outflows are known to affect the material from the immediate vicinity of the protostar (core and envelope) up to cloud scales (tens of parsec), and therefore are the most likely responsible for clearing surrounding material off the protostellar object, inducing the termination of the infall phase and affecting the star formation efficiency (Arce et al. 2007). The high temperatures produced when the outflow impacts the interstellar medium give rise to chemical reactions that would not occur in the quiescent, dense interstellar medium (ISM), increasing the chemical complexity in the affected gas. For all these reasons, molecular outflows are an important part of the star formation process.

Traditionally molecular outflows have been studied through observations of low$-J$ CO and low$-J$ SiO rotational lines (low$-J$ defined here as transitions up to $J_u = 5$). The upper state energies of these transitions imply that their excitation requires low gas temperatures. In the case of CO, transitions up to $J_u = 4$, with upper state energies (E_u) < 50 K, have been commonly used; for SiO transitions up to $J_u = 5$, with $E_u \leq 40$ K, have been usually observed to trace the outflow gas. However some studies exist of higher-J CO (up to $J_u = 38$, from space facilities such as ISO and Herschel: van Kempen et al. 2010a; Nisini et al. 2002), and SiO (up to $J_u = 11$, from ground-based facilities: Kawamura et al. 1999) transitions, probing temperatures $\geq$ 100 K. These observations have proven that such transitions are useful tools to trace

[1]Based on Gómez-Ruiz, Wyrowski, Gusdorf, Leurini, Menten, Güsten. Warms gas in protostellar outflows I, submitted to A&A

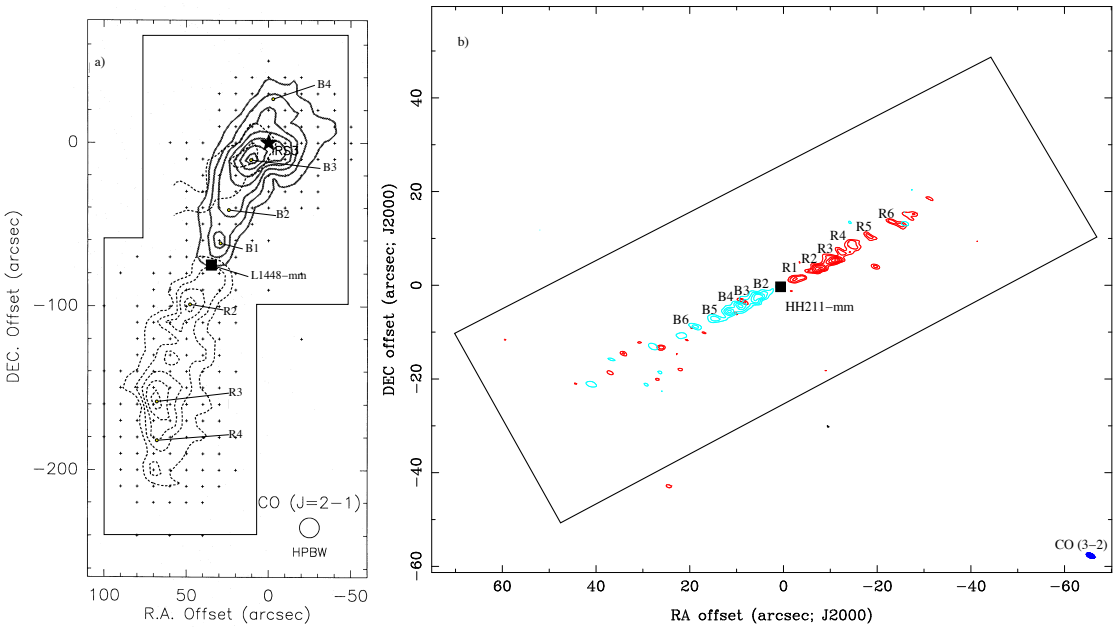

Figure 3.1: a) The CO (2–1) high-velocity emission in the L1448/IRS3 system, taken from Bachiller et al. (1990). The contours show the integrated emission in the ranges from -55 km s^{-1} to 0 km s^{-1} (solid) and from +10 km s^{-1} to +65 km s^{-1} (dashed). First contour and contour interval are 10 K km s^{-1}. The central (0,0) offset position is located at the position of IRS3 (black star), while the position of L1448-mm source is shown by the black square. The labels indicate the position of all clumps reported by Bachiller et al. (1990). b) The CO (3–2) high-velocity emission in HH211, from Palau et al. (2006). The contours show the integrated emission in the ranges from -14 km s^{-1} to 0 km s^{-1} (blue) and from +20 km s^{-1} to +40 km s^{-1} (red). Contours interval is 2σ, while first contour is 4σ (σ=2.21 and 2.38 Jy beam^{-1} km s^{-1}, for blue-shifted and redshifted, respectively). The central (0,0) offset position is located at the position of H211-mm (black square). The labels indicate the position of all clumps reported by Palau et al. (2006) and Hirano et al. (2006). At the bottom-right the beam of the CO (3–2) observations is shown. In a) and b), the beam of each observation is shown at the bottom-right, while the black polygons delineate approximately the area covered by the CO (6–5) and (7–6) observations.

the warm and/or dense gas present within the shocked regions.

Recent studies by van Kempen et al. (2009b,a), using the CHAMP+ array on the Atacama Pathfinder Experiment (APEX) telescope, have shown the importance of mid$-J$ CO transitions (throughout this paper referring to CO (6–5) and CO (7–6) transitions) in tracing the warm gas (50-200 K) in the envelope and outflow of low-mass protostars. These authors found a strong and narrow low-velocity CO (6–5) line around the central position and outflow regions of several low-mass objects, which they interpreted as emission originating from material heated by UV photons scattered in the outflow cavity, and not only by the passive heating taking place in the inner protostellar envelope. Since the low-velocity narrow component becomes stronger closer to the shocked region, it was suggested that the emission is produced by UV photons from the shocks, although no proper shock modeling was applied. In addition, the emission from the broad wing component was consistent with temperatures $\sim$ 100 K. Although these observations provided information on the heating process close to the central object and a preliminary view of the role of shocks in the excitation of mid$-J$ CO transitions in outflows, they shed little light on the excitation of CO in the high-velocity material. In particular, these studies did not target outflows with extremely high-velocity (EHV) emission. Recent CO (3–2) and SiO (8–7) observations of EHV outflows from class 0 protostars have suggested that these transitions may be tracing the material very close to the primary jet, probably the molecular counter part of the atomic jet (Palau et al. 2006). Especially attractive in this regard are submillimeter mid$-J$ CO observations towards such EHV outflows, because one would expect that their elevated excitations requirements would most directly make them probes of the primary jet. With the objective of studying the properties of the warm gas in EHV outflows, we have observed two well-known prototypes of such objects. In this paper we present CO (6–5) and (7–6) observations of two class 0 outflows with EHV emission and with a high collimation degree, namely L1448 and HH211.

3.2 The sources

3.2.1 The L1448-mm/IRS3 region

L1448 is a dense globule located in the nearby complex of dark clouds in Perseus (Bachiller & Cernicharo 1986), at a distance of 235 pc (Hirota et al. 2011). Associated with the globule are three IRAS sources, named IRS 1, 2, and 3; IRS3 being the most prominent source at infrared wavelengths (Bachiller & Cernicharo 1986). CO observations around IRS3 revealed the presence of high-velocity gas to the south of the infrared source (Bachiller et al. 1990). The high-velocity CO emission was found tracing a well collimated and bipolar structure, with a terminal radial velocity of about $\pm$70 km s^{-1} (with respect to an LSR velocity, V_{LSR}, of +4.5 km s^{-1}: Bachiller et al. 1990) and a size of $\sim$ 4.5' (see Fig. 1). Along the main outflow axis, several well-defined CO clumps were found moving at high velocities, the so-called molecular "bullets". These clumps appear at symmetrical positions with respect to a center

(83" south of IRS3) that was later identified as a compact millimeter continuum source (Bachiller et al. 1991a), with a bolometric luminosity, L_{bol}, of 7.5 $L_\odot$ (Tobin et al. 2007), named L1448-mm. In addition, the same CO observations also revealed a second (less energetic) outflow driven by IRS3 itself, orientated in a nearly east-west direction. To complicate matters, IRS3 turned to be a binary system, likely driving two bipolar outflows (e.g. Kwon et al. 2006). However, due to the overlap of IRS3 with the blue shifted lobe of L1448-mm outflow, a clear characterization of IRS3's outflows has been difficult, even for interferometric observations (Kwon et al. 2006). Through out the paper we will refer to the region that includes the main outflow from L1448-mm and the outflow system around IRS3 as L1448-mm/IRS3.

The clump pairs in the L1448-mm main outflow, as traced by CO (2–1), were named B1-R1, B2-R2, B3-R3, and B4-R4, with "B" and "R" referring to blue-shifted and red-shifted clumps, respectively, and with the numbering increasing going outwards from L1448-mm (Bachiller et al. 1990, see Fig. 3.1a). At the highest velocities ($V_{LSR}\sim$ -60 and +70 km s^{-1}, for blue- and red-shifted emission, respectively) B1 and R1 appear in CO (2–1) as weak intensity (T_{MB} ∼0.1 K) clumps within a region of ∼ 10" in radius around L1448-mm, while further away, B2-R2 show stronger CO (2–1) emission (T_{MB} ∼1 K). B3-R3 are similar to B2-R2 in intensity and size (∼ 20"), although at slightly lower velocities than the later. B4-R4 are less well defined and appear at moderate radial velocities. At the lowest velocities the outflow lobes excited by IRS3 system can be seen. In this paper, we use the same terminology as based on the CO (2–1) observations by Bachiller et al. (1990) to name the clumps we found in CO (6–5).

3.2.2 HH211-mm

Located in the IC 348 complex in Perseus, at a distance of 250 pc (Enoch et al. 2006), the HH211 outflow was discovered from H_2 observations at 2.12 μm (McCaughrean et al. 1994). The source driving this outflow was later identified with mm-wavelength continuum emission as a class 0 protostar with L_{bol} ∼3.6 $L_\odot$ (Froebrich 2005), known as HH211-mm. Follow-up CO observations showed that the low-velocity CO emission delineates a pair of cavities whose tips were associated with the 2.12 μm H_2 emission. On the other hand, high-velocity CO traces a narrow jet-like structure along the axis of the cavities (Gueth & Guilloteau 1999b, hereafter GG99). The high-velocity jet-like structure is also traced by SiO emission (e.g. Hirano et al. 2006). The total extent of the outflow is ∼ 1.2', with a terminal radial velocity of 25 km s^{-1} on the blue lobe and 35 km s^{-1} on the red lobe (with respect to the cloud V_{LSR} of +9.2 km s^{-1} Palau et al. 2006). The high-velocity emission consists of clump pairs (or "bullets"), symmetrically located at each side of the continuum source. These bullets pairs have been named by Hirano et al. (2006) as B1-R1, B2-R2, B3-R3, B4-R4, and B5-R5; with "B" and "R" referring to the blue-shifted and red-shifted clumps, respectively, and the numbering increasing going outwards from HH211-mm (see Fig. 3.1b). Additional clumps have been found in the CO emission, close to the bow-shocks traced by H_2 (Palau et al. 2006; Lee

Table 3.1: Transitions observed.

Line	ν_0 GHz	A 10^{-5} s^{-1}	E_u/k K	HPBW ”	η_s [a]
CO (6–5)	691.473	2.137	116.16	9.0	0.46
CO (7–6)	806.651	3.422	154.87	7.7	0.40
^{13}CO (6–5)	661.067	1.868	111.05	9.4	0.46

[a]Values measured during L1448/IRS3 observations. See text for details and for the values during HH211 observations.

Table 3.2: Source information and map rms.

Source	α(J2000) (h m s)	δ(J2000) (° ′ ″)	V_{LSR} (km s^{-1})[b]	^{12}CO rms (K)[a] (6–5)	(7–6)
L1448-mm	03:25:38.9	30:44:05.0	+4.5[c]	0.31	0.88
HH211-mm	03:43:56.8	32:00:50.0	+9.2[d]	0.66	0.21

[a]Average rms, in $T_{MB}{}^*$, at 1 km s^{-1} spectral resolution.
[b]Bandpass center.
[c]Bachiller et al. (1990).
[d]Palau et al. (2006).

et al. 2007). In this paper we use the same terminology as defined with low$-J$ CO and SiO observations by Hirano et al. (2006) and Palau et al. (2006) to name the clumps found in CO (6–5).

Recently, interferometric CO (3–2) and SiO (8–7) sub-millimeter observations have been done in HH211-mm (Hirano et al. 2006; Palau et al. 2006). A comparison between the CO (3–2) and SiO (8–7) high-velocity emission with lower$-J$ CO (2–1) and SiO (1–0) has shown that submillimeter transitions better trace the knots of gas very close to the exciting source than the low-J millimeter transitions. In particular, the B1-R1 clump pairs revealed in CO (3–2) and SiO (8–7) have no counterparts in CO (2–1) and SiO (1–0). Given the high densities and temperatures inferred for these high-velocity clumps close to the central position, it has been suggested that submillimeter CO and SiO transitions may be tracing the gas closely related with the primary jet (Hirano et al. 2006).

3.3 CHAMP+ observations at APEX

Mid$-J$ CO observations were performed with the MPIfR Principal Investigator (PI) instrument CHAMP+ (Kasemann et al. 2006) on the APEX telescope (Güsten et al. 2006). CHAMP+ is a dual-color 2 × 7 pixels heterodyne array for operation in the 450 μm (low frequency array, LFA) and 350 μm (high frequency array, HFA) atmospheric windows. The optics allow simultaneous observations in both colors. Both sub-arrays present an hexagonal arrangement. The front-end is connected to

a suit of fast Fourier transform spectrometer (FFTS: Klein et al. 2006).

L1448-mm/IRS3 was observed in CO (6–5), (7–6) and ^{13}CO (6–5) during 2009 June and August. HH211-mm was observed in the same transitions during 2010 July and September. For both sources the whole extent of their outflow was mapped (blue and red lobes) simultaneously in CO (6–5) and (7–6). For L1448-mm/IRS3 a second setup was used to map only the central and northern part of the region, simultaneously in ^{13}CO (6–5) and CO (7–6); while toward HH211-mm outflow single-pointing observations were done on selected positions in a third setup consisting of ^{13}CO (6–5) and HCO$^+$ (9–8). For the purpose of this paper, the HCO$^+$ (9–8) observations are not considered due to their low signal-to-noise. For all observations, the back was set with two overlapping units, of 1.5 GHz and 8192 channels each, that in the end provide a total bandwidth of 2.8 GHz. The final spectra were re-sampled to 1 km s^{-1} spectral resolution for all transitions in both sources.

During the observations, the precipitable water vapor (PWV) was in the range of 0.3 to 0.7 mm. The pointing was determined by CO (6–5) cross-scan observations on IK Tau (L1448-mm/IRS3) and CRL618 (HH211-mm). Pointing corrections were always within 3". Focus was checked on Mars. Mapping observations were done in the On-The-Fly mode, with an ON time of 0.5 seconds per position, and steps of 3". In the case of L1448-mm/IRS3, the reference position was observed without showing emission of the CO (6–5) line. On the other hand, for HH211-mm we did not observe the reference position, and therefore we can not discard the possibility of contamination at least around the cloud velocity. Spectra were reduced with CLASS and images were produced with GReG, both software being part of the GILDAS package [2]. During the June 2009 observations an anomaly in the warm optics affected the coupling efficiency of the LFA, requiring the application of a correction factor depending on the dewar angle of the array during the observations. In addition, due to weather instabilities, affecting the baseline stability of high frequency observations, a quarter of the CO (7–6) spectra in L1448 were not usable, affecting uniformly each point of the map. Table 4.1 and 4.2 show a summary of the observations, including the transitions observed and the coordinates (α/δ) of the central positions of the maps presented in this paper.

Intensities in this paper are presented in T_{MB} scale for which we have used a forward efficiency of 0.95 and beam efficiencies (η_s) measured on Jupiter. We consider the later appropriate, based on the average size of the structures we have mapped in both outflows. During L1448-mm observations, η_s values measured on Jupiter were 0.46 and 0.40, for LFA and HFA, respectively. During HH211-mm observations, η_s of 0.48 was measured for both LFA and HFA. Unless otherwise stated, through out the paper LSR velocity is used to present and describe the data.

[2] http://iram.fr/IRAMFR/PDB/gildas/gildas.html

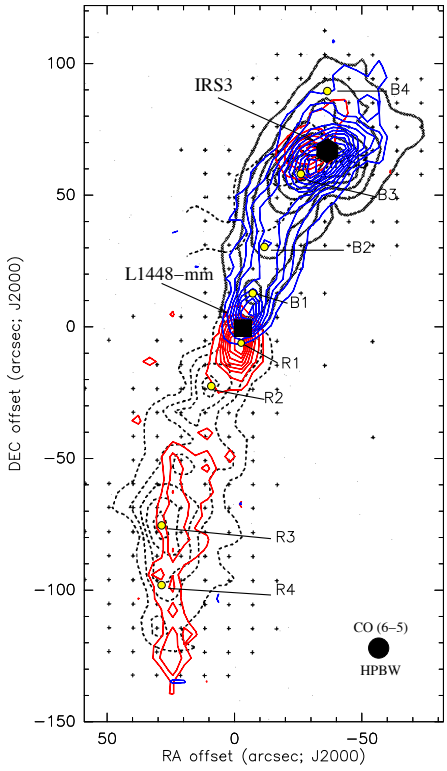

Figure 3.2: The CO (6–5) high-velocity emission in the L1448-mm/IRS3 system. Blue contours show the blue-shifted wing (from -55 km s^{-1} to 0 km s^{-1}) and red contours the red-shifted wing (from +10 km s^{-1} to +65km s^{-1}). The contour spacing is 2σ (σ=0.262 K), with the first contour at 3σ. The central (0,0) position is located at the coordinates of L1448-mm source (see Table 2) and indicated by the black square. The black hexagon represents the position of IRS3 (offset -38,+70). Black contours (solid and dashed) show the CO (2–1) emission from Bachiller et al. (1990), integrated in the same velocity ranges. The black crosses indicate the coverage of the CO (2–1) map, which is roughly identical in CO (6–5). Yellow circles indicate the positions of all the clumps reported by Bachiller et al. (1990). Also shown by a black filled circle is the HPBW at the frequency of the CO (6–5) transition.

3.4 Molecular outflows in L1448-mm/IRS3

3.4.1 High-velocity CO (6–5) emission

The CO (6–5) emission was detected in a velocity range from -60 to +70 km s^{-1}. Figure 3.2 shows the CO (6–5) emission in L1448-mm/IRS3, integrated over the red and blue shifted wings. The overall morphology is similar to the structures traced by previous low$-J$ CO observations. Red-shifted emission is mainly tracing

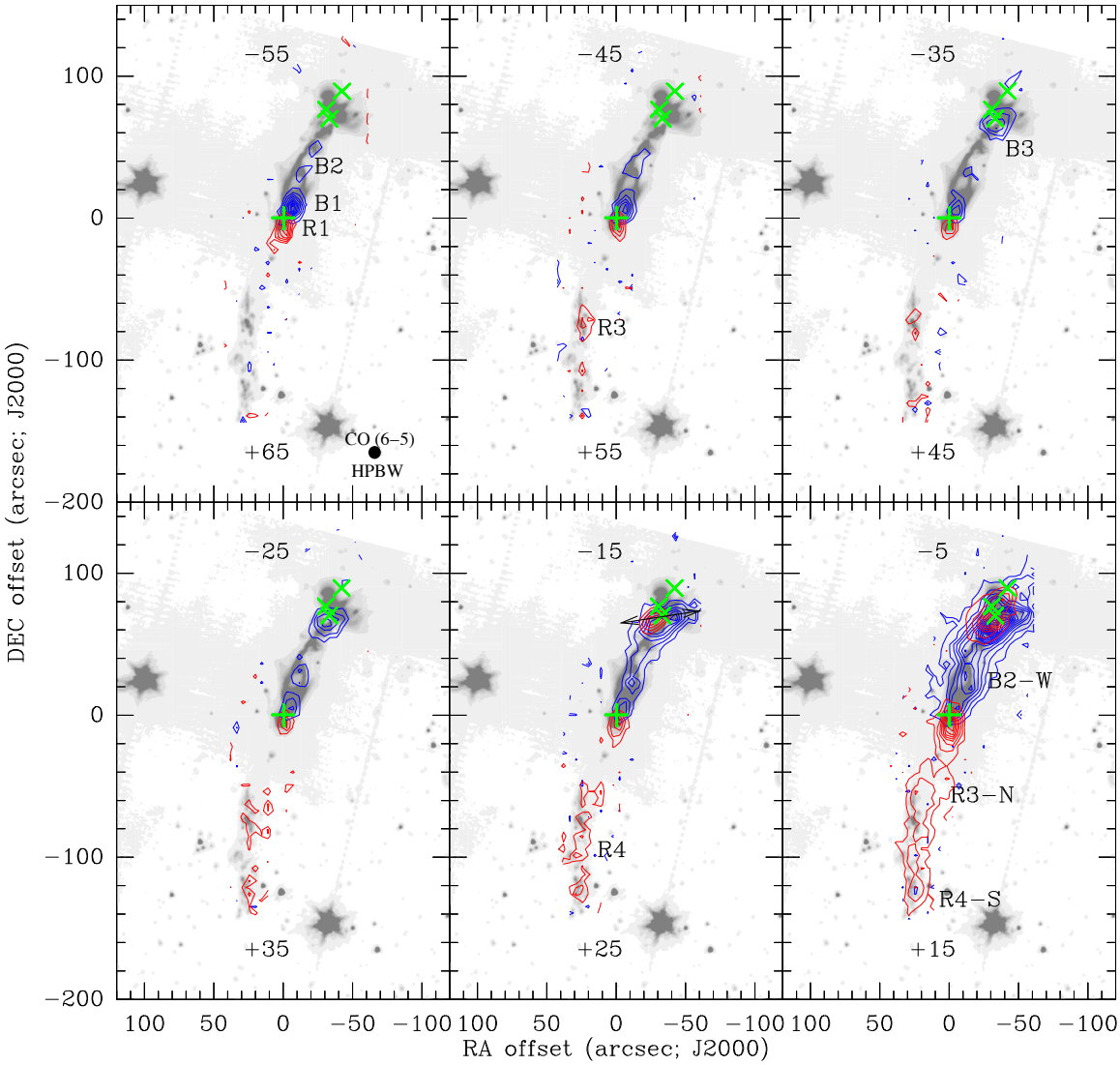

Figure 3.3: CO (6–5) maps of the L1448-mm/IRS3 region in different velocity ranges, overlaid on the *Spitzer/IRAC* 4.5μm image. Each panel shows the integrated red- and blue-shifted emission in a 10 km s^{-1} wide velocity interval, centered on the velocity shown in the bottom (red-shifted) and top (blue-shifted) part of each panel. The contour spacing is 2σ, with the first contour at 3σ (σ=1.20 K km s^{-1} for blue contours and σ=1.61 K km s^{-1} for red contours). The (0,0) offset refers to the position of L1448-mm central source (see Table 1), also indicated by a green plus symbol. The green crosses represent the position of the members of the IRS3 system (3A, 3B, and 3C: Kwon et al. 2006) The arrow in the bottom-middle panel indicates the direction of the outflow system from IRS3. Note that the peak values for the highest velocity range are 11.3 K km s^{-1} for B1 and 10.3 K km s^{-1} for R1.

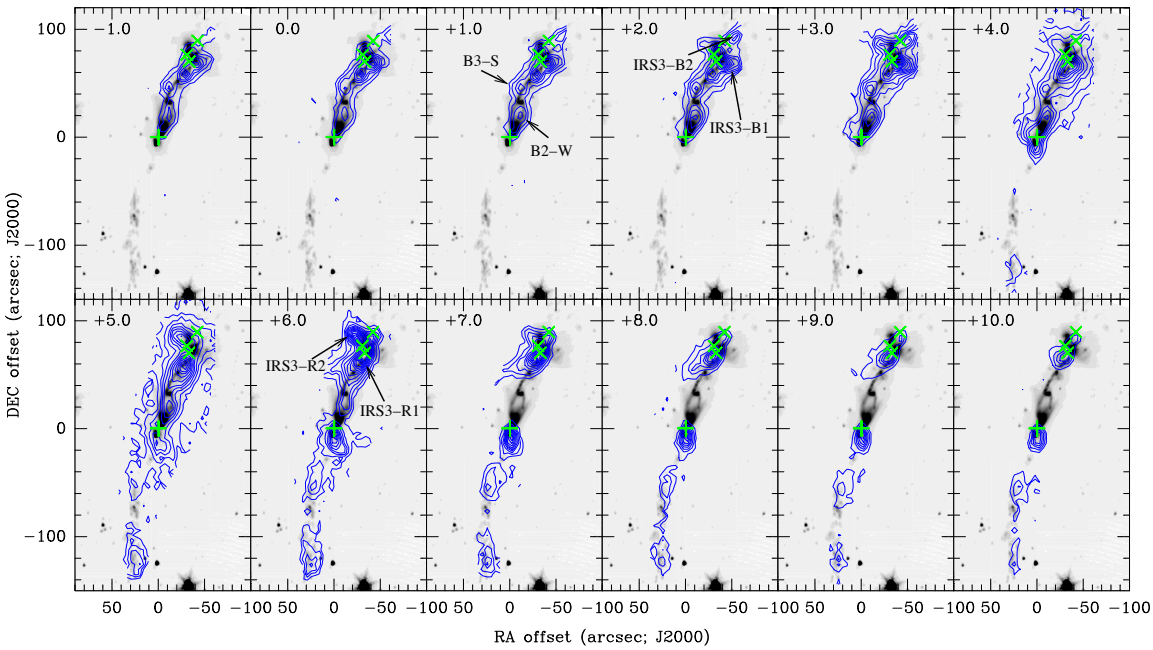

Figure 3.4: CO (6–5) low-velocity channel maps in L1448-mm/IRS3 region. Contours spacing is 2σ, with the first contour at 3σ (σ=0.62 K km s^{-1}). The green plus symbol and crosses as in Fig 3.3. The arrows indicate the clumps that are traced only at low velocities (positions reported in Table 3.3).

a curved-like structure that forms the red-lobe located to the south-east of L1448-mm. To the north-west of the central position a blue-shifted lobe terminates around the position of IRS3. Close to the position of IRS3 one also notes the presence of a red-shifted clump that, together with a blue-shifted elongated feature to the west, delineates the outflow system from IRS3. From the integrated intensity map it is seen that the CO (6–5) brightness distribution is more prominent within the inner 20″ around L1488-mm and around IRS3. Also, the red-shifted lobe from L1448-mm shows weaker emission than the blue-shifted lobe.

Figure 3.3 presents the CO (6–5) emission integrated in intervals of 10 km s^{-1}, from high to low velocities, overlaid on the 4.5μm mid-IR emission from *Spitzer/IRAC*, which is thought to trace shocked regions (Neufeld et al. 2009; Tobin et al. 2007; Smith et al. 2006). Most of all the clumps previously found in low$-J$ CO are present at the velocity intervals of the CO (6–5) emission, showing the characteristic blue-red correspondence. At high velocities, the clumps with the strongest emission are B1-R1 ($T_{MB} \sim 1$ K). The B2-R2 clumps are weakly detected at their nominal velocities; indeed R2 is barely detected in the interval between +60 km s^{-1} to +50 km s^{-1}. This behavior is the opposite to low$-J$ CO (2–1) emission, in which B2-R2 are stronger than B1-R1 at such high velocities. In addition, B4, a clump detected in CO (2–1) around -40 km s^{-1} to -20 km s^{-1} (see Bachiller et al. 1990), is not detected in our CO (6–5) observations in that velocity range. The remaining clumps (B3-R3 and R4) present a similar behavior in the CO (6–5) as in the (2–1) line.

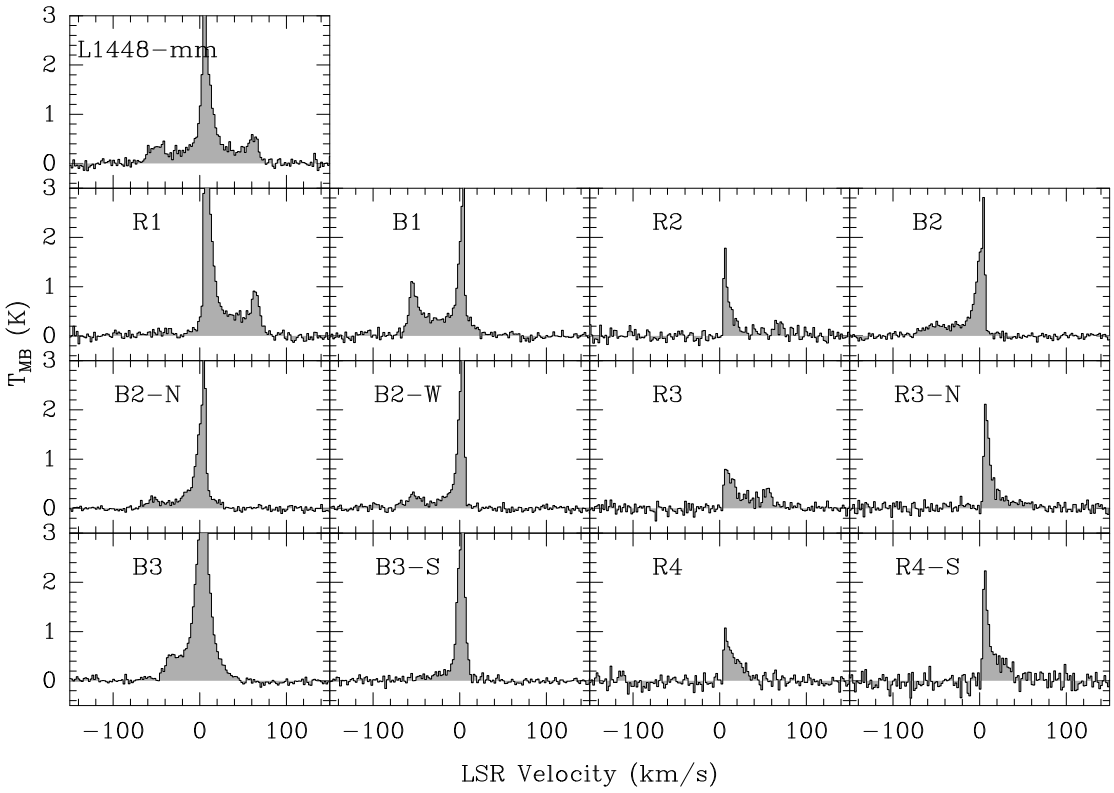

Figure 3.5: CO (6–5) spectra at the positions indicated in Fig.3.3. The spectral resolution is 1 km s^{-1}. Upper left corner of each panel indicates the position on which the spectrum was taken.

In Table 3.3 we report the position of the clumps obtained by a two-dimensional Gaussian fit to the CO (6–5) maps. For the Gaussian fits we have used the velocity interval, from Fig. 3.3, in which the clumps are the strongest. Table 3.3 also shows the deconvolved minor and major axis of the Gaussian fits, as well as their position angle (P.A.). As revealed by the deconvolved sizes, the high-velocity emission from B1/R1 is not resolved in the direction perpendicular to the jet axis. The clumps further away from the central position (e.g. R3, R4) are partially or fully resolved in the 9.0″ FWHM beam.

The last two lower velocity panels in Fig. 3.3 show the low-velocity CO (6–5) emission. At these velocities, outflow from IRS3 is seen mixed with emission from B3 clump of the L1448-mm outflow. At the velocity intervals centered at -15 and +25 km s^{-1}, two compact clumps (blue- and red-shifted clumps) are oriented in an almost east-west direction, likely tracing the high-velocity part of IRS3 outflow (marked by an arrow in Fig. 3.3).

3.4.2 Low-velocity CO (6–5) emission

In Fig.3.4 we show the low-velocity channels, in bins of 1 km s^{-1}, of the CO (6–5) emission in L1448-mm/IRS3. The outflow structures are clearly recognized in all the low-velocity channels. A rich clumpy structure is seen around the blue lobe of L1448-mm and IRS3 system (see, e.g., 2 and 3 km s^{-1} channels). A more diffuse and extended emission is also noted especially in the couple of channels around the cloud velocity (4 and 5 km s^{-1} channels). Several of the clumps seen in these low-velocity channels did not have counterparts at high velocities. These clumps are named B2-W and B3-S, for L1448 outflow, and IRS3-B1, IRS3-B2, IRS3-R1, and IRS3-R2 for the clumps related to the outflows excited by IRS3. The positions of these low-velocity clumps are also shown in Table 3.3.

3.4.3 CO (6–5) line profiles

Figure 3.5 shows a sample of spectra at different positions in L1448-mm/IRS3. Similar to previous low$-J$ CO observations, several spectral features are present. First, the peak of the CO emission at the cloud velocity (V_{LSR} =4.5 km s^{-1}), which is present in all the positions shown in Fig. 3.5. Second, the high-velocity broad wing, extending from -65 km s^{-1} to ∼+75 km s^{-1}. The third component is represented by the so-called EHV bullets, which are shown in the spectrum around L1448-mm, B1, and R1 positions as secondary peaks at ∼ -60 km s^{-1} in the blue lobe and ∼ +70 km s^{-1} in the red lobe. Important to note is also the characteristic shock profile at the positions R2, B2, and R3. This profile is represented by a peak at low velocities, with a gradual decrease of the intensity towards high velocities, while a sharp decrease in intensity is seen towards low velocities (Schilke et al. 1997).

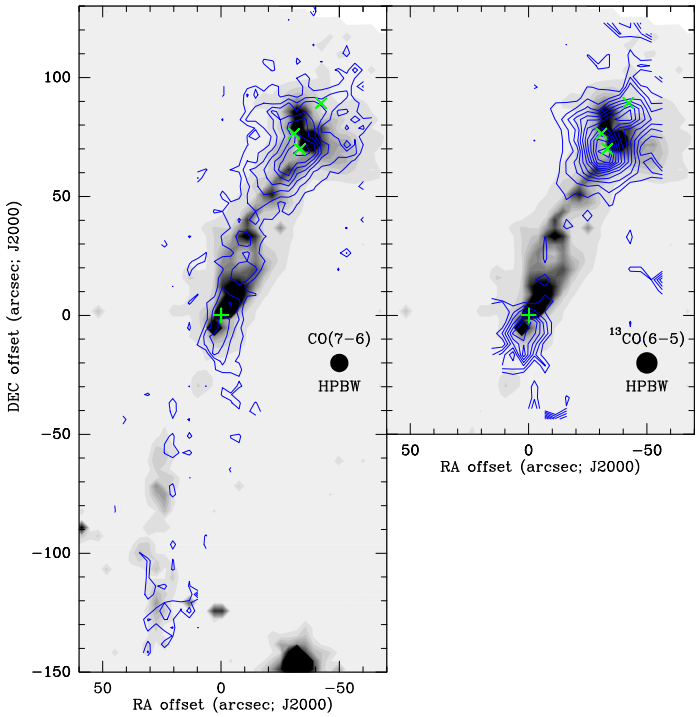

Figure 3.6: Integrated CO (7–6) (left panel) and ^{13}CO (6–5) (right panel) emission in L1448-mm/IRS3. Contours start at 3σ and then are spaced by steps of 2σ for both CO (7–6) and ^{13}CO (6–5). σ=8.55 K km s^{-1} for CO (7–6) and σ=0.62 K km s^{-1} for ^{13}CO (6–5). The green plus symbol and crosses as in Fig. 3.3.

3.4.4 ^{13}CO (6–5) and CO (7–6)

The ^{13}CO (6-5) map of L1448-mm/IRS3 includes the positions L1448-mm, R1, B1, R2, B2, B2-W, B2-N, B3, B3-S, and IRS3. Due to time constrains and the fact that the ^{12}CO (6–5) emission was found weaker towards the red lobe, the rest of this lobe was not covered by the ^{13}CO (6–5) map. The integrated intensity ^{13}CO (6–5) map is presented in Fig. 3.6 while the spectra at selected positions is shown in Fig.3.7. The ^{13}CO (6–5) emission was clearly detected only towards L1448-mm, R1, R2, B3, and IRS3. Marginal detections ($\sim 2\sigma$) are reported in B1, B2-N, B2-W, and B3-S. No detection was found in B2. In all the cases the ^{13}CO (6–5) emission is only detected in 1 to 3 channels around the systemic velocity.

On the other hand, owing to the simultaneous observations with the CO (6–5) line, the CO (7–6) map covered all the L1448/IRS3 system. The integrated intensity CO (7–6) map is shown in Fig.3.6 and the CO (7–6) spectra at selected positions is shown in Fig.3.8. The CO (7–6) emission was found mostly at low velocities. However, at L1448-mm, B1, and R1 positions, the CO (7–6) emission is detected at extremely high velocities (at a 6σ level). The total integrated emission is dominated by the low-velocity gas. The low velocity emission stronger around L1448-mm (including R1, B1, and B2 clumps) and around IRS3 (see Fig. 3.6).

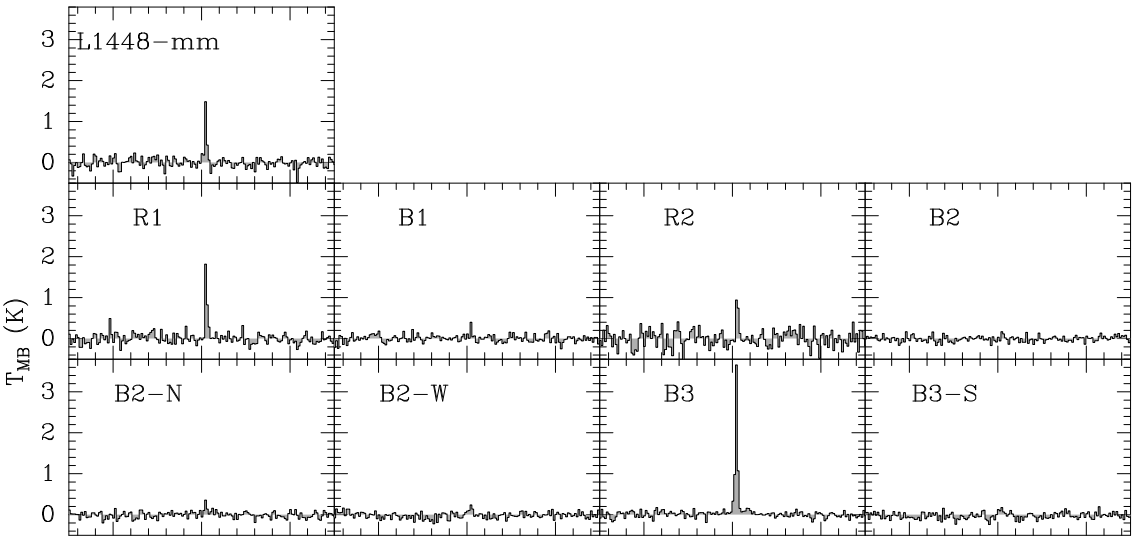

Figure 3.7: ^{13}CO (6–5) spectra at the observed positions in L1448/IRS3. The positions are indicated in each panel. The spectral resolution is 1 km s^{-1}.

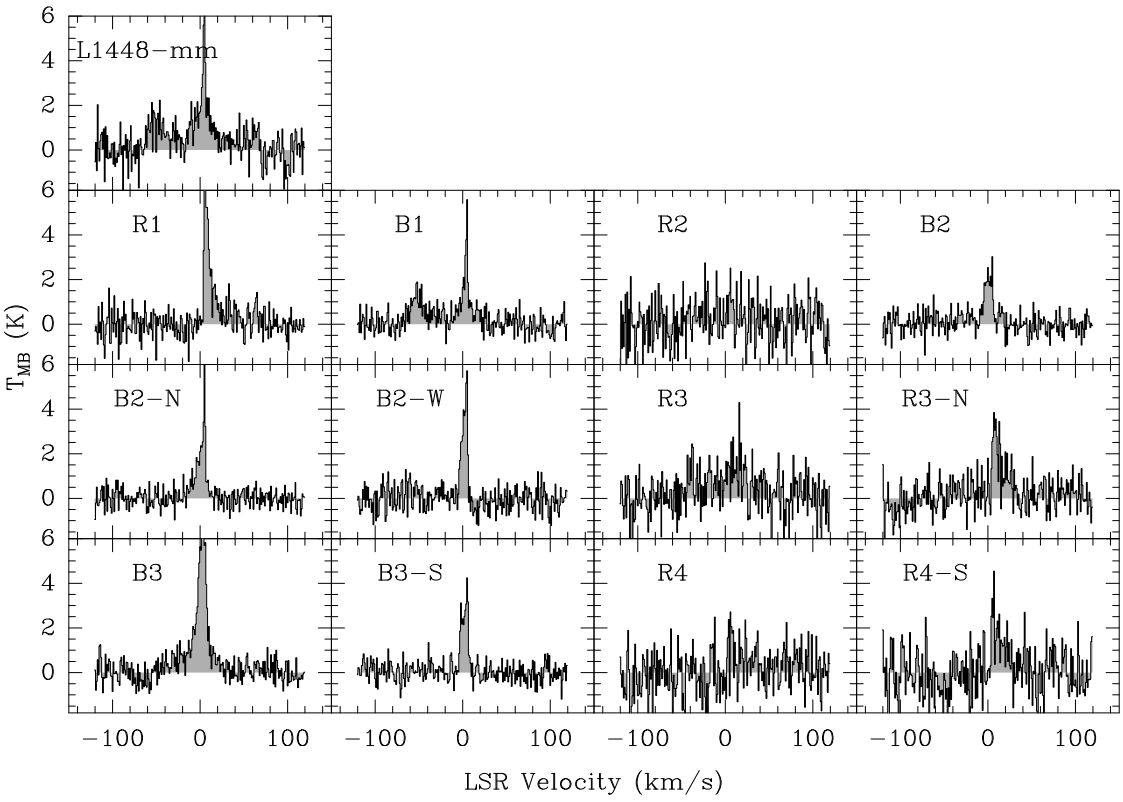

Figure 3.8: CO (7–6) spectra at the observed positions in L1448/IRS3. The positions are indicated with labels in each panel. The spectral resolution is 1 km s^{-1}.

Table 3.3: Clump characteristics derived from the CO (6–5) emission.

Clump	Velocity^{+} range (km s^{-1})	offset ($''$, $''$)	α(J2000) h m s	δ(J2000) $^\circ$ $'$ $''$	Deconvolved major axis ($''$)	Deconvolved minor axis ($''$)	P.A. ($^\circ$)	$\int T_{MB} dv^{*}$ K km s^{-1}
L1448-mm								
B1	-75,26	-6.9, 7.6	03:25:38.3	30:44:12.68	11.6	4.2	-17.5	103.7(1.4)
R1	-19,85	-1.0, -7.6	03:25:38.8	30:43:57.30	11.7	2.5	-15.3	146.1(1.7)
B2	-75,12	-13.4, 34.1	03:25:37.8	30:44:39.10	16.7	12.2	-9.8	70.2(1.1)
B2-N	-73,40	-21.6, 46.4	03:25:37.2	30:44:51.43	18.2	8.7	-33.6	81.6(1.1)
B2-W	-78,10	-8.8, 16.2	03:25:38.2	30:44:21.23	46.5	15.6	-30.4	77.2(1.2)
R2	-1,80	7.3, -21.1	03:25:39.4	30:43:43.82	*a*	*a*	*a*	38.4(2.2)
B3	-52,52	-34.6, 66.5	03:25:36.2	30:45:11.56	18.5	13.3	-69.4	185.8(1.1)
B3-S	-33,17	-12.7, 46.1	03:25:37.9	30:44:51.13	28.5	17.5	-36.8	72.6(1.0)
R3	-1,66	22.9, -73.6	03:25:40.6	30:42:51.31	24.7	9.7	4.3	40.1(1.9)
R3-N	0,68	18.9, -50.3	03:25:40.3	30:43:14.63	36.0	20.2	-17.1	49.7(1.9)
R4	0,66	27.1, -93.8	03:25:41.0	30:42:31.20	35.9	16.7	-23.9	33.1(2.3)
R4-S	-1,60	25.1, -117.4	03:25:40.8	30:42:07.50	42.5	16.8	6.7	54.8(3.0)
IRS3								
IRS3-B1	-40,20	-41.6, 68.5	03:25:35.6	30:45:13.58	19.3	12.4	86.0	158.1(2.5)
IRS3-R1	-47,35	-28.4, 62.6	03:25:36.6	30:45:07.64	30.2	13.6	-39.4	209.8(2.3)
IRS3-B2	-5,8	-52.0, 89.6	03:25:34.8	30:45:34.66	26.4	11.5	-38.3	36.7(1.8)
IRS3-R2	-8,15	-28.6, 82.7	03:25:36.6	30:45:27.74	26.7	11.3	59.2	60.7(1.4)
IRS3-B3	-33,26	-29.9, 58.8	03:25:36.5	30:45:03.89	16.0	13.9	-46.2	180.5(2.0)
HH211-mm								
B1-B2-B3	-10,15	11.6, -3.7	03:43:57.6	32:00:46.23	19.8	4.3	-66.7	75.6
R1-R2-R3	3,45	-7.2, 6.3	03:43:56.2	32:00:56.38	21.0	1.4	-58.2	72.9
B7	-3,16	29.0, -10.1	03:43:59.0	32:00:39.82	22.0	3.1	-78.6	70.0
R6	4,17	-22.0, 14.1	03:43:55.0	32:01:04.10	20.1	3.5	-73.1	45.3

a: convolution seems to produce a point source. $^{+}$ Total velocity range of the emission at 3σ level.
*: Total integrated emission within the specified velocity range.

3.5 The HH211 molecular outflow

3.5.1 High-velocity CO (6–5) emission

The CO (6–5) emission in HH211 was detected from -14 to +42 km s^{-1}. Figure 3.9 shows the CO (6–5) integrated intensity maps at low and high velocities, overlaid on the 4.5μm IRAC/Spitzer emission as a reference for shocked gas (Neufeld et al. 2009; Smith et al. 2006). The low-velocity emission (from 2 to 18 km s^{-1}) shows a shell-like structure surrounding the mid-IR features, but also noted are well defined peaks coincident with the mid-IR knots around the bow-shocks. On the other hand, at high velocities the CO (6–5) emission peaks close the central source, but also near the bow-shocks traced by the mid-IR emission. Important to note is that our CO (6–5) observations can not resolve spatially the individual clumps close to the central source. In particular, the inner bullets, B1, B2, B3 and R1, R2, R3, are shown as a single pair of knots in our CO (6–5) map. We refer to these knots as B1-B2-B3 and R1-R2-R3 in Fig. 3.9. Since in previous low$-J$ CO observations the clumps at the mid-IR bow-shock positions were not named, we call them B7 and R6, following the notation from previous works. Important to note is that these clumps at the mid-IR bow-shocks showed weaker emission in CO (3–2) than in our CO (6–5) observations (e.g. Palau et al. 2006; Lee et al. 2007). All the clump positions are reported in Table 3.3. In general, the morphology of the CO (6–5) emission is similar to that seen in low$-J$ CO observations.

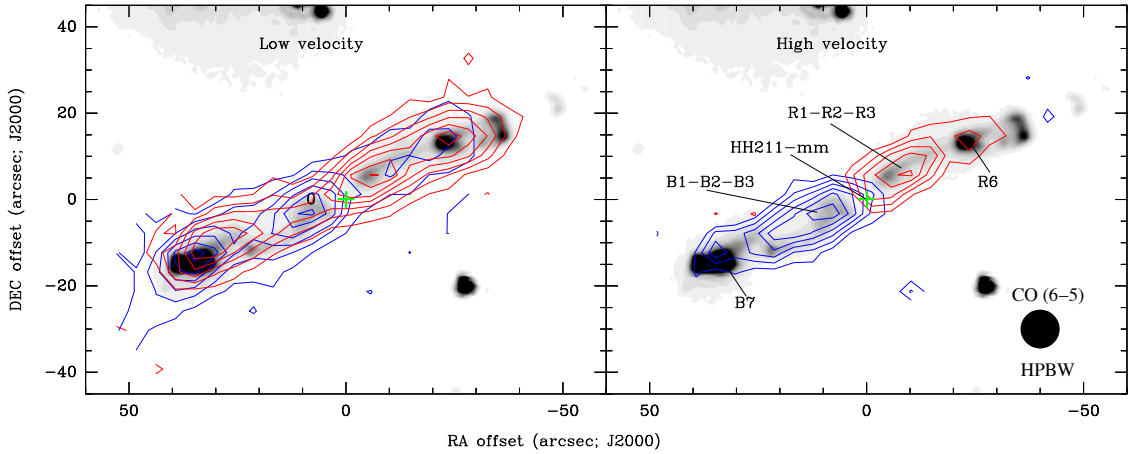

Figure 3.9: CO (6–5) emission in HH211 overlaid on the *Spitzer/IRAC* 4.5μm emission. Left: integrated low-velocity emission (2 to 8 km s^{-1} [blue] and 10 to 18 km s^{-1} [red]). Right: integrated high-velocity emission (-15 to 1 km s^{-1} [blue] and 19 to 41 km s^{-1} [red]). For low-velocity emission the contours spacing is 3σ, with the first contour at 3σ (σ=2.32 K km s^{-1}). For the high-velocity emission the contours spacing is 2σ, with the first contour at 3σ (σ=2.64 K km s^{-1} for blue and σ=3.17 K km s^{-1} for red). The green plus symbol indicates the position of HH211-mm source, located at offset (0,0) (see Table 1). Also shown by a black circle is the HPBW at the frequency of the CO (6–5) transition.

3.5.2 Low-velocity CO (6–5) emission

In Fig.3.10 we show the low-velocity channels, in bins of 1 km s^{-1}, of the CO (6–5) emission in HH211-mm. At these low-velocity channels the outflow's bipolar structure is clearly recognized in all the low-velocity channels. However, a more diffuse emission is also noted in channels 8 km s^{-1} and 9 km s^{-1} (i.e around the cloud velocity, V_{LSR} = +9.2 km s^{-1}). Interesting to note is that both outflow lobes are simultaneously present in channels 10 and 11 km s^{-1}. All the emission clumps found at high velocities are also visible in the low-velocity emission.

3.5.3 CO(6–5) line profiles

Figure 3.11 shows a sample of spectra taken at the positions indicated in Fig. 3.9. Although at all the positions the CO (6–5) emission peaks close to the cloud velocity, an important contribution from the high-velocity part of the spectra is noted as a broad "plateau" feature, from -14 to +42 km s^{-1}, towards the HH211-mm position. Important to note is that at this central position the CO (6–5) emission does not show secondary peaks at high velocities as in the case of L1448-mm. The latter may be due to a projection effect, since the axis of HH211 outflow is closer to the plane of the sky than in the case of L1448, which then causes that the secondary peaks "merge" with the broad "plateau" component. Another spectral feature is the wing-like emission at the B1-B2-B3 and R1-R2-R3 positions, which actually resembles the

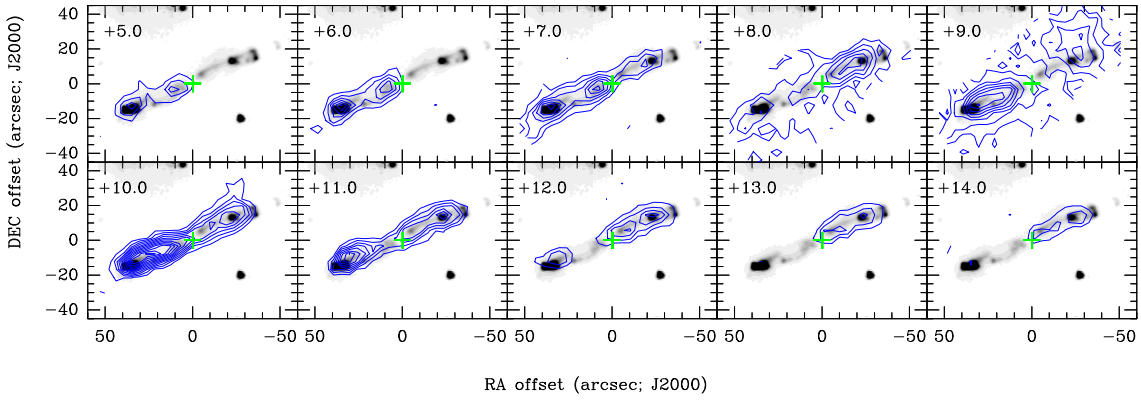

Figure 3.10: CO (6–5) low-velocity channel maps in HH211-mm. The contours spacing is 2σ, with the first contour starting at 3σ (σ =0.79 K km s^{-1}). The green plus symbol as in Fig 3.9.

characteristic shock profile (i.e. slow decrease in intensity towards high velocities). In B1-B2-B3, the emission extends up to $\sim$ -10 km s^{-1}, while in R1-R2-R3 up to $\sim$+40 km s^{-1}. At the R6 position two spectral components are clearly defined: a narrow (FWHM$\sim$5 km s^{-1}) and low-velocity (V_{LSR} $\sim$9 km s^{-1}) component and a broad (FWHM$\sim$10 km s^{-1}) and high-velocity (V_{LSR} $\sim$40 km s^{-1}) component. The low-velocity component shows stronger emission (T_{MB} $\sim$9 K) than the high-velocity one (T_{MB} $\sim$2 K). An indication of a similar two-component feature is suggested in the spectrum at B7 position, but the high-velocity component is not as strong in intensity as in the R6 position. This two velocity component feature in the spectra at the apex positions is the mean difference between our mid$-J$ CO data and the previous low$-J$ CO observations which only show a weak emission at this position (e.g. Lee et al. 2007, G99). Finally, at all positions shown in Fig. 3.11, a narrow absorption feature can be seen at the cloud velocity, which likely comes from the contamination of the reference position.

3.5.4 ^{13}CO (6–5) and CO (7–6)

Figure 3.14 shows the ^{13}CO (6–5) spectra taken at three different positions in HH211, namely HH211-mm, B7, and R6. Towards the HH211-mm position, the ^{13}CO (6–5) emission is detected from 7 to 14 km s^{-1}, while around the B7 position the emission is present from 7 to 11 km s^{-1}. At R6, the ^{13}CO (6–5) emission is only detected from 9 to 11 km s^{-1}. The spectra of the CO (7–6) emission at selected positions is shown in Fig. 3.12. The low-velocity CO (7–6) emission (from $\sim$ 0 km s^{-1} to 10 km s^{-1}) is detected at all the positions, and at high-velocities only towards B1-B2-B3 (up to ~ -10 km s^{-1}) and R1-R2-R3 (up to $\sim +30$ km s^{-1}). The integrated CO (7–6) map of the low-velocity range (were the emission is stronger) is presented in Fig. 3.13. The CO (7–6) map shows that the emission is tracing the same structures revealed by CO (6–5).

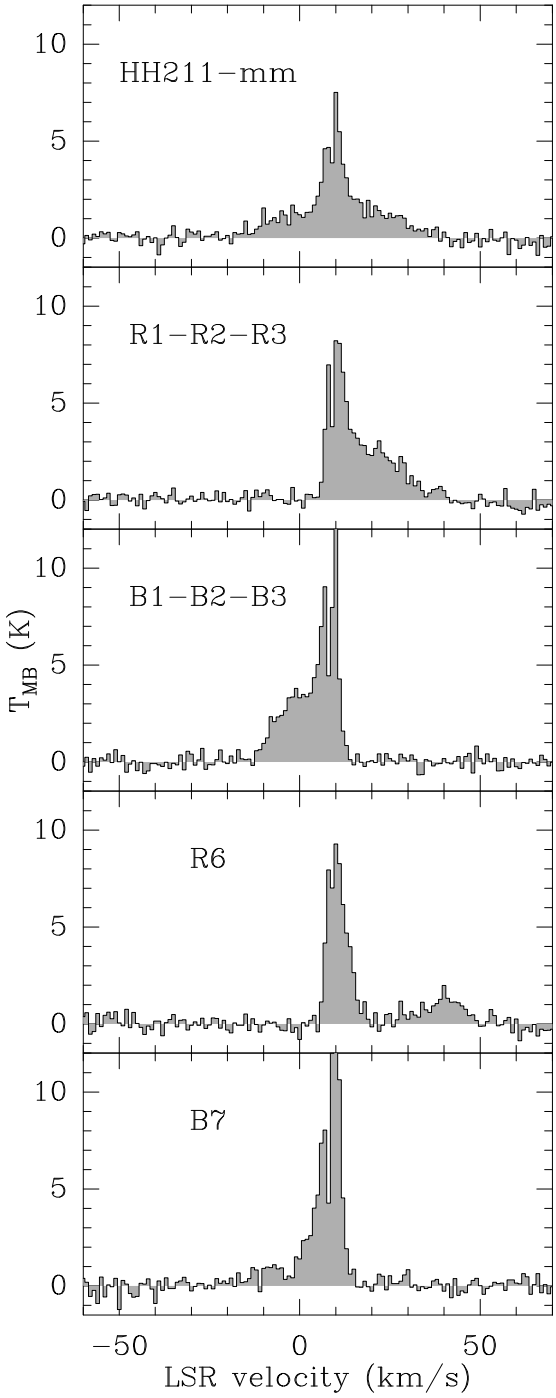

Figure 3.11: CO (6–5) sample of spectra at selected positions in HH211. The spectral resolution is 1 km s^{-1}. Upper left corner of each panel indicates the position on which the spectrum was taken. Such positions are indicated in Fig. 3.9. Note that the clumps B7 and R6 show secondary peaks at high velocities. Note also the absorption feature at the cloud velocity (V_{LSR} =9.2 km s^{-1}), seen in all the positions shown here, which likely comes from the contamination of the reference position.

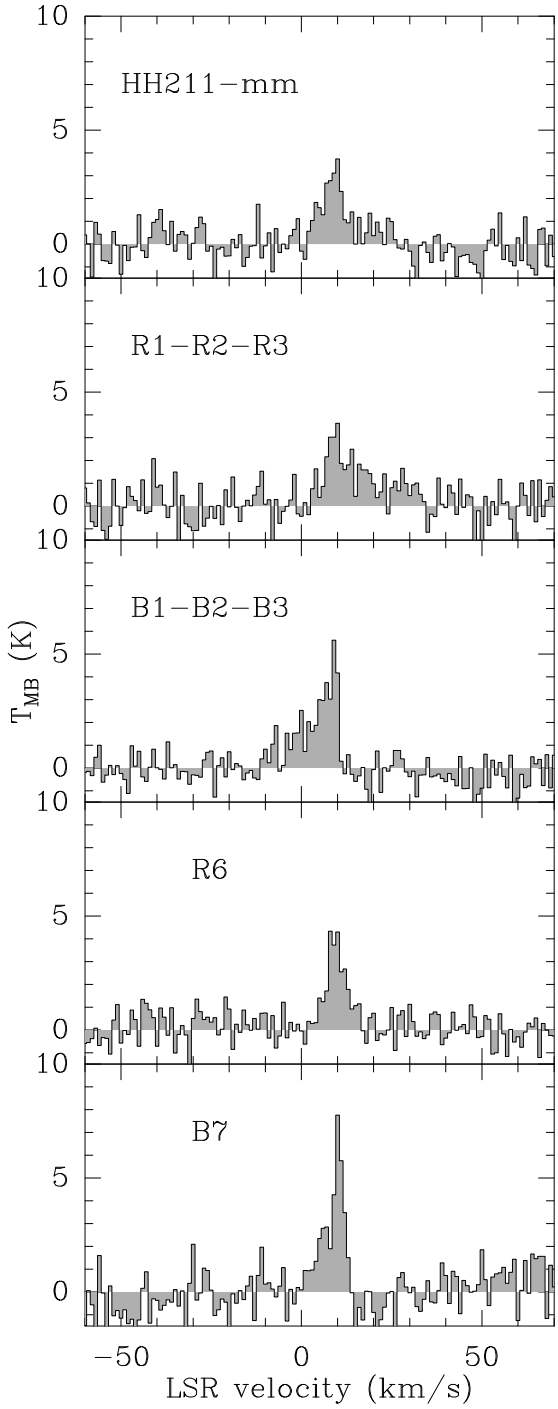

Figure 3.12: CO (7–6) sample of spectra at selected positions in HH211. The spectral resolution is 1 km s^{-1}. Upper left corner of each panel indicates the position on which the spectrum was taken. Such positions are indicated in Fig. 3.9. Note that the secondary peaks at high velocities revealed by the CO (6–5) transition are not detected in CO (7–6). Note also the absorption feature at the cloud velocity that, as in the case of the CO (6–5) emission, likely comes from the contamination of the reference position.

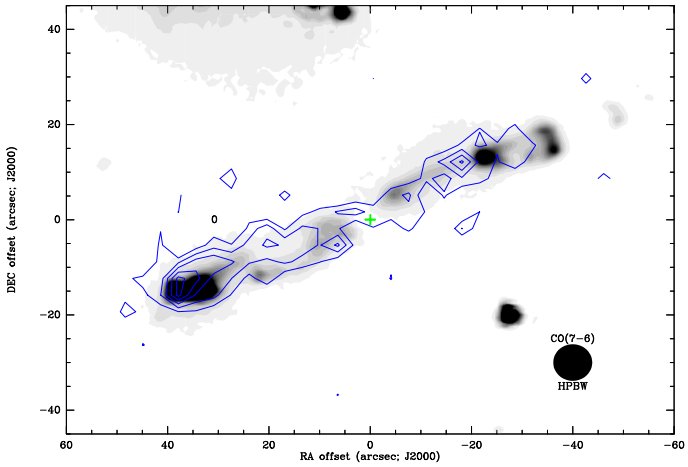

Figure 3.13: The CO (7–6) emission integrated from 8 km s^{-1} to 12 km s^{-1}. Contour spacing is 1σ with the first contour at 3σ (σ=5.6 K km s^{-1}). The green plus symbol and grey scale as in Fig 3.9.

3.6 Optical depths

We estimate the ^{12}CO (6–5) optical depth (τ_{12}) using the ^{12}CO (6–5)/^{13}CO (6–5) line ratio. Assuming that the ^{13}CO (6–5) is optically thin (which is usually the case for the line wings, e.g. Leurini et al. 2006), and that the ^{12}CO (6–5) and ^{13}CO (6–5) have the same excitation temperature, the following relation holds:

$$\frac{T_A^{12}}{T_A^{13}} = \frac{\nu_{12}}{\nu_{13}} \frac{[^{12}CO]}{[^{13}CO]} \left(\frac{1 - e^{-\tau_{12}}}{\tau_{12}} \right). \quad (3.1)$$

In equation (1), T_A^{12} and T_A^{13} refer to the antenna temperature of ^{12}CO (6–5) and ^{13}CO (6–5) lines, respectively, with ν_{12} and ν_{13} their corresponding rest frequencies. [^{12}CO]/[^{13}CO] is the abundance ratio that in our case we assume to be 62 (Langer & Penzias 1993). Therefore, equation (1) can be solved numerically to obtain τ_{12}.

From the spectra shown in Fig. 3.5 and 3.7, we have computed the ^{12}CO/^{13}CO (6–5) line ratio at different positions in L1448/IRS3. As already discussed, the ^{13}CO (6–5) emission was mostly detected at low velocities, with its peak at the cloud velocity. In table 3.4 we show the ^{12}CO/^{13}CO (6–5) line ratio at the cloud velocity and the corresponding τ_{12}. At the channel corresponding to the cloud velocity, the ^{12}CO/^{13}CO (6–5) line ratio is in between 1.5 - 2.5, for L1448-mm, R1, R2, B3 and IRS3. Consequently, τ_{12} is > 30, and thus optically thick. On the other hand, at the positions where the ^{13}CO (6–5) was marginally detected around the cloud velocity (B1, B2-N, B2-W, and B3-S), τ_{12} is in between 1 - 3, and therefore moderately optically thick. The upper limit computed around the extremely high-velocity range suggest that ^{12}CO is at most moderately optically thick, i.e. $\tau_{12} < 6$ at R1 and $\tau_{12} < 3$ at B1. At the position B2, where ^{13}CO (6–5) was not detected at

Table 3.4: ^{12}CO opacities at the cloud velocity.

Position	^{12}CO/^{13}CO	τ_{12}	Position	^{12}CO/^{13}CO	τ_{12}
L1448-mm	2.2(0.2)	28.2	HH211-mm	1.5(0.2)	41.3
B1	8.5(1.6)	7.3	B7	7.6(1.0)	8.1
R1	1.8(0.1)	34.4	R6	4.3(0.6)	14.4
B2	>41.9	<0.8			
R2	2.4(0.6)	25.8			
B2-N	19.4(4.1)	3.0			
B2-W	26.7(9.8)	2.0			
B3	2.2(0.07)	28.2			
B3-S	31.9(14.5)	1.5			
IRS3	1.5(0.04)	41.3			

all, the upper limit indicates that the emission should be optically thin (^{12}CO/^{13}CO ratio > 41, thus $\tau_{12} < 0.8$). In summary, the information provided by the ^{13}CO (6–5) observations indicates that the ^{12}CO (6–5) low-velocity emission is optically thick around the central objects (L1448-mm and IRS3) and at R1, R2, and B3. On the other hand, at low velocities the ^{12}CO (6–5) emission is moderately optically thick at B1, B2-N, B2-W, and B3-S, or even optically thin at B2. The upper limits for the extremely high-velocity gas suggest that the ^{12}CO (6–5) emission is at most moderately optically thick **(<5)** at such velocities.

From the ^{12}CO and ^{13}CO (6–5) spectra in Fig. 3.11 and 3.14, we calculate the ^{12}CO/^{13}CO (6–5) line ratios. The line ratio values at the cloud velocity are presented in Table 3.4. The ^{12}CO/^{13}CO (6–5) line ratios varies from 1.5 to 7.6 at the tree different positions observed. Such ratios indicate that τ_{12} at the cloud velocity is $\sim$ 41, 8, and 14, in HH211-mm, B7, and R6, respectively. Additionally, in channels adjacent to the cloud velocity, τ_{12} can get down to 10 and 3, in HH211-mm and B7, respectively. These results show that the ^{12}CO (6–5) line is optically thick around at the cloud velocity in HH211-mm, B7, and R6; while it can be moderately optically thick in adjacent channels in B7. Finally, upper limits to the ^{12}CO opacity in the high-velocity gas are $\lesssim$ 12, 13, and 8, for HH211-mm, B7, and R6, respectively. Therefore our ^{13}CO (6–5) observation were not sensitive enough to prove whether or not the ^{12}CO (6–5) emission is optically thin at high velocities.

The calculation of the ^{12}CO opacities in L1448-mm/IRS3 and HH211-mm have demonstrated that the CO (6–5) emission is optically thick around the central objects. On the other hand, the upper limits estimated for the high-velocity gas suggest that this emission is at most moderately optically thick in the outer line wings. Moreover, in the case of L1448-mm, even the low-velocity gas in the blue lobe presents moderately optically thick emission. In the following calculations for the outflow physical parameters we will assume that the ^{12}CO(6–5) emission at high velocities is optically thin. Thereafter, assuming an average optical depth from the upper limit calculations of the high-velocity range, give an estimation of the correction factor due to optical depths effects.

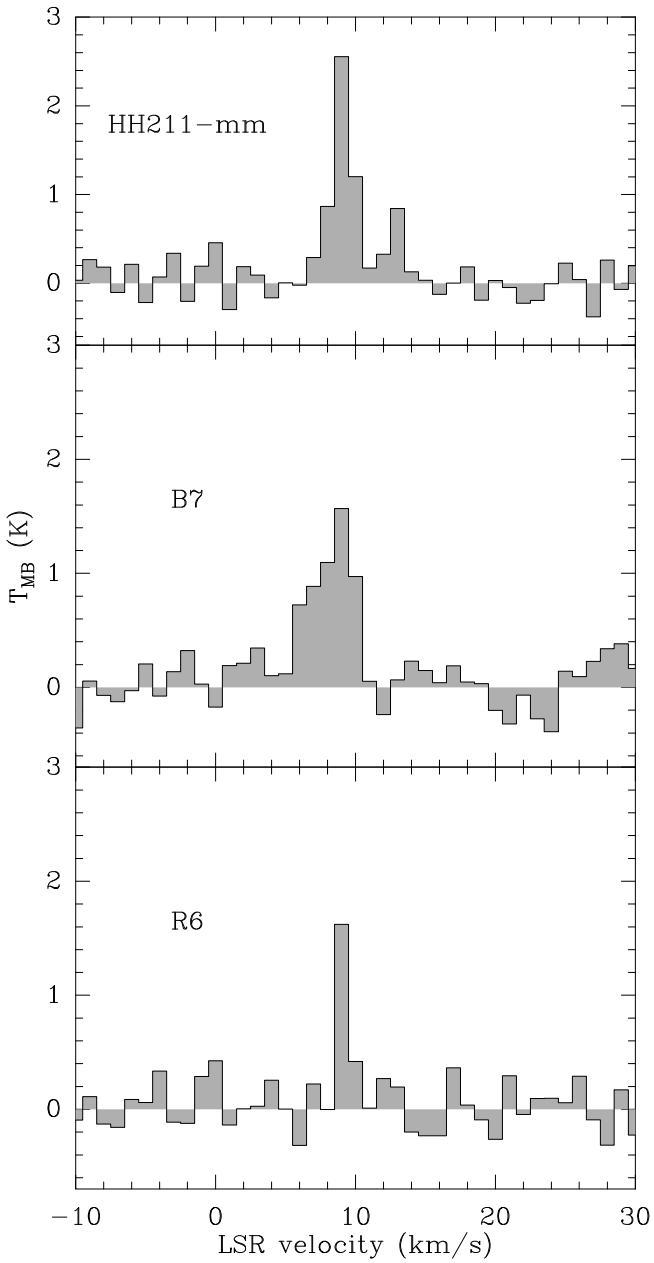

Figure 3.14: ^{13}CO (6–5) spectra at the positions HH211-mm, B7 and R6 (see Fig. 3.9). The spectral resolution is 1 km s^{-1}.

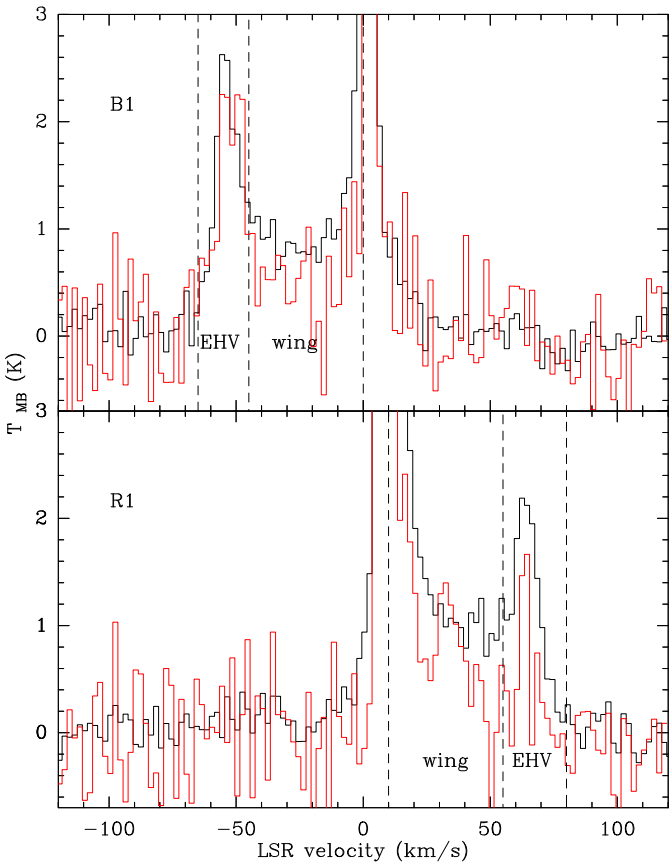

Figure 3.15: CO 6–5 (black) and 7–6 (red) spectra (2 km s^{-1} spectral resolution) at B1 and R1 positions in L1448-mm. Velocity ranges in which the emission is divided to study the physical conditions are indicated by vertical dashed lines (EHV and wing).

3.7 Excitation and physical conditions

3.7.1 Population diagram

We produced population diagrams to estimate the rotational temperature, T_{rot}. Under the assumption that the gas is in LTE, the population of each level follows the Boltzmann law, that in the optically thin case can be expressed as $\log(N_u/g_u)=\log(N/Q)-\log(e)/T_{rot}$, where N_u and g_u are the column density and statistical weight of the upper state level, respectively, N the total column density, and Q the partition function (e.g. Goldsmith & Langer 1999). N_u is related to the integrated intensity (W) by $N_u=8\pi k\nu^2 W/hc^3 A_{ul}$, where k and h are Boltzmann and Planck constants, respectively, c the speed of light, ν the rest frequency, and A_{ul} the Einstein coefficient (see Table 1). The partition function is approximated by $Q\sim T/(4.8\times10^{-2}B_e)$, where B_e (57.6 GHz for CO) is the rotational constant (e.g. Rohlfs & Wilson 2004).

At the B1 and R1 positions in L1448-mm, complementary low-J CO (4–3) observations are available in the literature (Nisini et al. 2000) and henceforth we have

Table 3.5: CO integrated intensities at B1 and R1 clumps in L1448-mm outflow

Velocity	$\int$ Tdv(σ) (K km s^{-1})		
interval	4–3	6–5	7–6
		B1	
EHV	33.4(0.9)	21.8(0.7)	13.5(2.4)
Wing	86.6(1.2)	33.8(1.0)	13.2(3.1)
		R1	
EHV	26.4(0.8)	19.8(0.9)	9.7(3.0)
Wing	138.1(1.1)	59.5(1.2)	30.0(4.0)

EHV:-45 to -70 km s^{-1} (B1); 55 to 80 km s^{-1} (R1)
Wing: 0 to -44 km s^{-1} (B1); 10 to 54 km s^{-1} (R1)

used them in our calculations. We have then convolved our CO (6–5) and CO (7–6) observations to the same angular resolution of CO (4–3) observations, HPBW $\sim 11''$ (Nisini et al. 2000). In order to compare with a previous analysis made on these positions by Tafalla et al. (2010), we have divided the spectra at those positions into two velocity regimes: the Extreme High Velocity (EHV) (-45 to -65 km s^{-1} for B1; 55 to 80 km s^{-1} for R1), and the wing (0 to -44 km s^{-1} for B1; 10 to 54 km s^{-1} for R1). Table 4.4 shows the CO (4–3, 6–5, 7–6) integrated intensities, at $11''$ resolution, and in Fig. 3.16 we present the results of the least-square fits to the rotational diagrams for the two velocity regimes. Within the EHV range, a T_{rot} of $\sim$ 56 K and N$\sim$ 1.5$\times$10^{16} cm^{-2} is found for B1; while for R1 we obtain $T_{rot} \sim$ 49 K and N$\sim$ 1.3$\times$10^{16} cm^{-2}. On the other hand, the wing emission shows T_{rot} of $\sim$ 58 K and N$\sim$ 2.5$\times$10^{16} cm^{-2} for B1, while $T_{rot} \sim$ 62 K and N$\sim$ 3.5$\times$10^{16} cm^{-2} are found for R1. Therefore, a higher T_{rot} and a lower total column density are found in the EHV range compared to the wing emission. This tendency was also found by Tafalla et al. (2010) with low$-J$ CO transitions. We note however that assuming the τ_{12} upper limits for the EHV emission calculated in sect. 6, the computed column densities would increase by a factor 6 and 3, for R1 and B1, respectively.

For all the other positions in L1448-mm outflow we have used the total integrated intensities of CO (6–5) and (7–6) to produce the rotational diagram. The results of the least-square fits to the rotational diagrams are shown in Table 5 together with the results obtained in the same way for the different positions in HH211-mm outflow. The column densities calculated from the rotational diagram analysis are used in the following non-LTE calculations.

3.7.2 Large Velocity Gradient

Radiative transfer calculations with RADEX (van der Tak et al. 2007) were made in the Large Velocity Gradient (LVG) approximation and plane-parallel geometry. The molecular data was retrieved from the LAMBDA data base [3], which uses the

[3]http://www.strw.leidenuniv.nl/ moldata/

Table 3.6: Rotational diagram results for total integrated intensities

Position	T_{rot}(K)	N_T (10^{16} cm^{-2})
L1448-mm		
R1	42±5%	15.5±22%
B1	38±6%	13.1±23%
R2	70±23%	2.14±84%
B2	39±11%	5.24±41%
B2-N	40±10%	9.95±39%
B2-W	53±9%	5.00±34%
R3	132±9%	2.30±34%
R3-N	129±8%	2.31±31%
B3	54±4%	14.0±13%
B3-S	40±13%	8.39±49%
R4	79±15%	1.66±53%
R4-S	70±11%	2.96±40%
HH211-mm		
B1-B2-B3	44±4%	5.70±13%
R1-R2-R3	52±10%	4.25±40%
B7	44±9%	5.20±34%
R6	50±10%	2.74±35%

energy levels, transition frequencies and Einstein A coefficients from the CDMS and JPL catalogs. The collisional rate coefficients are adopted from Yang et al. (2010) and include energy levels up to J=40 for temperatures ranging from 2K to 3000K.

Thermal pressure. A linear molecule such as CO can be a tracer of density or temperature. CO line ratios are density tracers at low densities, when collisions compete with radiative decay. At higher densities, the excitation becomes thermalized and the line ratios are sensitive to temperature (van der Tak et al. 2007). However, a quantity than can be better constrained by CO line ratios is the thermal pressure, defined as $T_{kin} \times n$, since usually ratios that use CO (6–5) and (7–6) transitions show a flatter curve than in a T_{kin} vs n plot (see, e.g. van der Tak et al. 2007).

A series of LVG calculations were performed to reproduce the CO (6–5)/CO (7–6) line ratio, at different positions within the outflow lobes. In our calculations we have used the column densities previously derived from the rotational diagrams (Table 5). The results at some selected positions are shown in Fig. 4.9 as thermal pressure vs. temperature plots. Although the 6–5/7–6 line ratio cannot put severe constraints on the physical conditions of the clumps, a tendency of increasing thermal pressure towards positions further away from the central object is suggested in L1448-mm (e.g. R4-S compared to B1). In the case of L1448-mm, a tendency of higher thermal pressure is suggested in the EHV gas (black-dashed line in Fig. 4.9a,b) compared to the total integrated emission (green line in Fig. 4.9a,b). On the other hand, in HH211-mm the thermal pressure seems to be no different than in the

inner/outer positions, whereas such difference is seen between red-shifted and blue shifted emission. A tendency of higher thermal pressure in the red-shifted clumps compared to the blue-shifted is suggested, as seen from Fig. 4.9.

Spectral Line Energy Distribution (SLED). In order to study the importance of APEX/CHAMP+ mid$-J$ CO observations in constraining the outflow's physical parameters, we have added to our LVG analysis the high$-J$ CO data observed with ISO (Nisini et al. 1999, 2000). Thus we have constructed the CO-SLED for the EHV gas, from J=2 to J=22, and fitted LVG models from RADEX. Since ISO-LWS observations were not able to resolve the EHV contribution from red and blue lobe, both in space and velocity, only the averaged blue-red emission can be analyzed. Therefore, for low and mid$-J$ CO we sum the flux from red and blue, while for ISO-LWS we adopt the same assumption as Nisini et al. (2000) that the high$-J$ CO emission comes from the EHV gas only. Figure 3.18 shows the CO-SLED together with several LVG model fits. First we tried to fit the high$-J$ CO data as made in previous works (Nisini et al. 2000), resulting in a hot component as previously found (n_{H_2} $\sim$6.5$\times$10^4 cm^{-3} and T_{kin} $\sim$ 1250 K). However this best fits to the high$-J$ CO data does not match the mid$-J$ CO observations. In fact the best fit to the high$-J$ CO emission over-predict the flux of the mid$-J$ CO lines, which therefore indicates that such fit is incorrect. The data points suggest that low$-$ and mid$-J$ CO emission may be tracing a different component compared with the high$-J$ CO emission. The different components that can explain the low- and mid$-J$ CO observations are indicated in Fig. 3.18 as two LVG fits, which show lower temperatures (i.e. up to T_{kin} $\sim$ 100 K) than the best fit for high$-J$ CO lines. Since a slightly different excitation conditions between blue-shifted and red-shifted clumps are suggested by the different CO intensity of both clumps (CO 6–5 emission is about 1.5 stronger in B1 than in R1) we have also tried to fit a LVG model to the individual clumps. Figure 3.18 presents also the CO-SLED for B1 only and the LVG model which better fits the low- and mid$-J$ data points. Note that for the high$-J$ CO lines, fluxes are scaled down by a factor 1.5, the intensity ratio between B1 and R1 in CO (6–5). In this case, temperatures $>$ 1200 K and densities $>$5$\times$10^5 are the conditions of the high-velocity gas. Again, it seems not to be possible to fit mid$-J$ and high$-J$ CO lines with the same LVG model, which means that they probably trace a different gas.

We have also constructed the CO-SLED around the central position of HH211-mm. ISO data has been taken from Giannini et al. (2001), and we have used the CO (6–5) and (7–6) total integrated emission around the central position. The resulting CO-SLED is shown in Fig. 3.19 along with different LVG models obtained with RADEX. From the figure it is seen that the mid$-J$ and high$-J$ CO emission cannot be reproduced by the same LVG model. High$-J$ CO emission is consistent with densities between 8$\times$10^4 to 2$\times$10^6 cm^{-3}, and kinetic temperatures between 230 to 950 K (see also Giannini et al. 2001). On the other hand, mid$-J$ CO observations are consistent with densities of $\sim$ 5$\times$10^4 cm^{-3} and T_{kin} $\sim$20 K. We have again a similar situation as in L1448, in which mid$-J$ and high$-J$ CO emission cannot be explained by a single LVG model, which then may imply that they probably trace

a different gas.

In the literature, only few protostellar outflows have reported CO observations from low- to high$-J$ ladders. Among them, recent examples that include Herschel high$-J$ CO and ground-based mid$-J$ CO observations are the low-mass outflows HH46 and HH52-54 (van Kempen et al. 2010b; Bjerkeli et al. 2011). In both cases the CO SLEDs are fitted with at least two different components, although the fitted physical parameters are slightly different from our results for L1448 and HH211 (e.g. higher temperatures found in L1448/HH211 compared to HH52-54).

3.8 Outflow properties

Using the velocity integrated CO (6–5) map we calculate the outflow mass. In the optically thin case, the relation between the total column density (N) with the velocity integrated emission (W) is given by:

$$N = \frac{1.4 \times 10^{14}}{(J+1)\mu^2 B_e} \frac{e^{(4.8\times10^{-2} B_e J(J+1)/T_{ex})}}{1 - e^{(-4.8\times10^{-2}\times 2B_e(J+1)/T_{ex})}} \times W, \tag{3.2}$$

that, for the CO (6–5) becomes:

$$N(CO) = 3.92 \times 10^4 \frac{e^{82.94/T_{ex}}}{1 - e^{-33.18/T_{ex}}} \times W. \tag{3.3}$$

We use the standard ISM value for the relative ^{12}CO abundance, X(H_2/CO) $\sim 10^4$, to obtain the H_2 column density and finally calculate the H_2 mass,

$$M = 2 \times m_H \times X(H_2/CO) \times \Omega \times N \times D^2. \tag{3.4}$$

In the latter, m_H is the hydrogen mass, Ω the solid angle of the lobe, and D the distance to the source. Note that to correct for opacity effects, the above expression for the mass should multiplied by $\tau_{12}/(1 - e^{-\tau_{12}})$. We measure ΩN by summing up the contribution of each pixel with a S/N ratio above 3. For both outflows we use a T_{ex} of 50 K for the calculation, based on the results of the rotational temperatures given in Table 5. For L1448-mm, with a total extension of 0.40 pc (blue: 0.19 pc; red:0.21 pc) the total outflow mass is 0.03 $M_\odot$. For HH211-mm, with an extension of 0.107 pc (blue: 0.058 pc; red: 0.049 pc), the total outflow mass is 0.003 $M_\odot$. We have also estimated the mass of IRS3 outflow, under the same assumption of T_{ex}= 50 K. In this case, the integrated intensity maps were done from -20 to +1 km s^{-1} for the blue-shifted emission and from 25 to 9 km s^{-1} for the red-shifted emission. The total mass of IRS3 outflow is 6.86E-3 $M_\odot$. The outflow mass assuming a T_{ex} of 50 K for all outflows are summarized in Table 4.6. Since it is possible that the emission in the low-velocity wings, which contribute considerable in total wing integrated emission, maybe at least moderately optically thick, we take the average τ_{12} values determined for the low-velocity emission (sect. 6) and calculate the correction factor to the mass estimation to account for opacity effects. The average τ_{12} are 3 and 6, for L1448/IRS3 and HH211-mm, respectively.

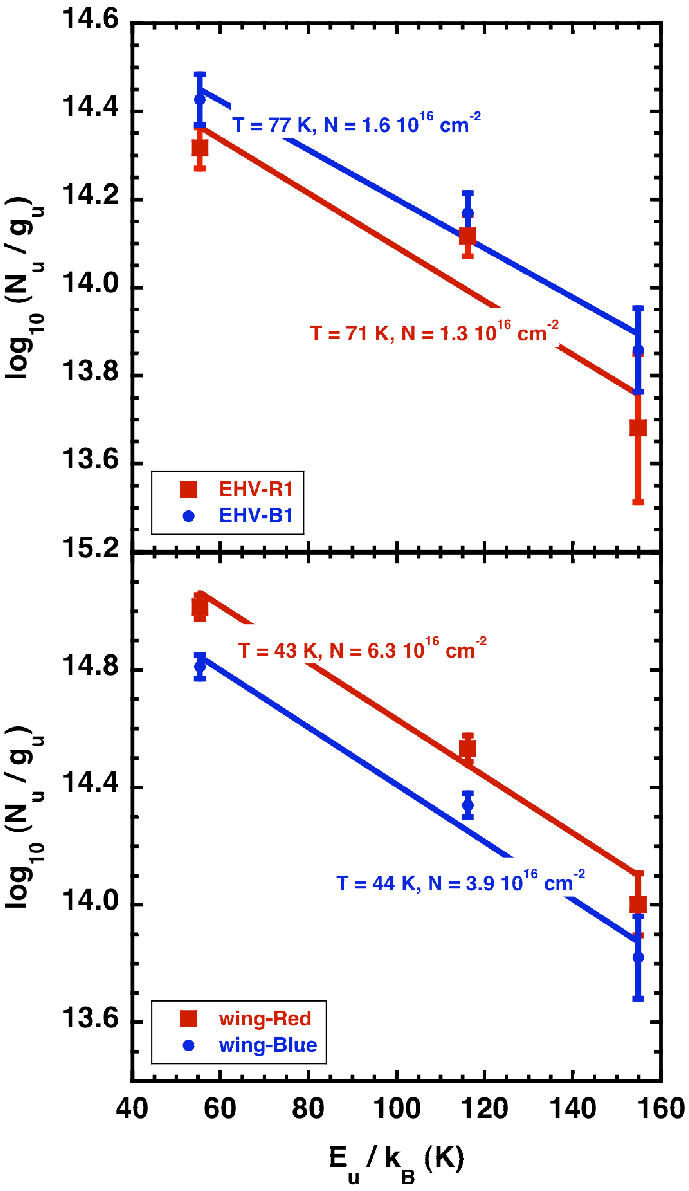

Figure 3.16: Population diagram for the CO emission in the L1448 B1/R1 clumps. The upper panel shows the rotational diagram for the EHV range, while the lower panel corresponds to the wing range. Blue and red colors for symbols and lines represent B1 and R1, respectively.

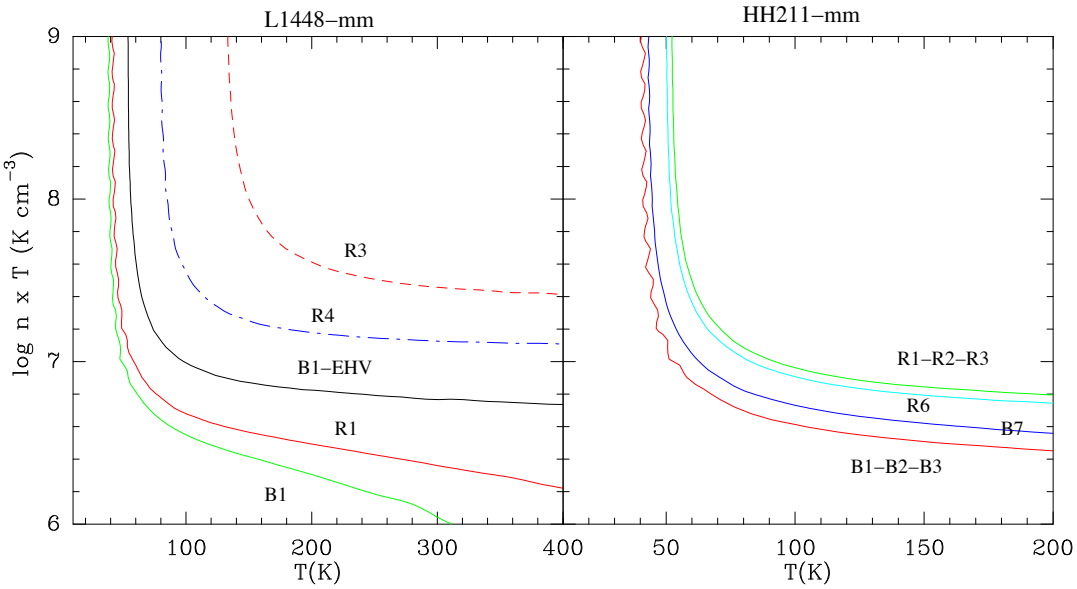

Figure 3.17: Thermal pressure vs temperature plot from LVG calculations. The panels show the 6–5/7–6 observed ratios at different positions in L1448-mm (left) and in HH211-mm (right). Note that with the exception of B1-EHV in L1448-mm, line ratios are computed from the total integrated emission.

Therefore, accounting for opacity effects, the masses would be ∼3 and ∼6 times higher than the ones computed assuming optically thin emission, for L1448/IRS3 and HH211-mm, respectively.

From previous CO (2–1) observations in L1448-mm the total mass was estimated to be 0.056 $M_\odot$, by using a T_{ex} of about 15 K (Bachiller et al. 1990). Assuming the same T_{ex} of 15 K in our calculations, a total outflow mass of 0.14 $M_\odot$ is obtained, which is a factor of only ∼ 2.5 higher than the result from CO (2–1). A larger discrepancy is found for HH211-mm, that with a T_{ex} of 50 K, previous mass estimate from CO (2–1) observations resulted in a value of ∼0.02 $M_\odot$ (GG99), which is then a factor of ∼13 higher than our calculations based on the CO (6–5) emission. On the other hand, Curtis et al. (2010) reported, from CO (3–2) observations, a mass estimate of 0.009 $M_\odot$, that within the error is in agreement with our results based on the CO (6–5) emission. The discrepancy with the results from GG99 may be due to larger amount of gas that is excited in CO (2–1) compared to the CO (4–3) or (6–5) transitions. Our mass estimation for IRS3 outflow is also consistent within the errors with previous results from Kwon et al. (2006).

We also determine other parameters such as dynamical time scale (t_d), mass outflow rate ($\dot{M}$), mechanical force (F_m), kinetic energy (E_k), and mechanical luminosity (L_{mech}). We define these quantities as follows: t_d=R_{max}/δ_{max}, $\dot{M}$=M/t_d, P=$M\times\delta_{max}$,F_m=$M\times\delta_{max}/t_d$, E_k=$M\times\delta^2_{max}/2$, L_{mech}=E_k/t_d (e.g. Beuther et al. 2002a). In the above expressions R_{max} and δ_{max} are the maximum extension and maximum relative velocity of the lobes. In Table 4.6 we show the summary of the results we

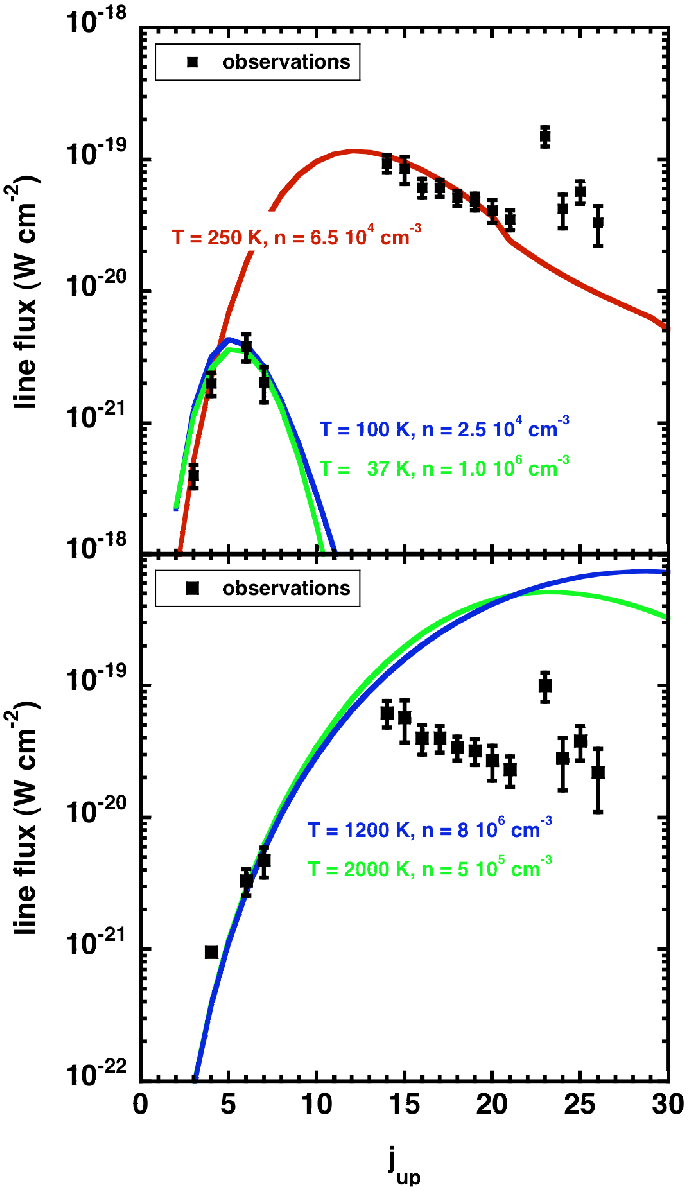

Figure 3.18: LVG model fits to CO-SED in the EHV range in L1448: Combined blue-red emission (upper panel) and blue-lobe only (lower panel). The red line shows the best fit to the ISO high-JCO data, while blue and green lines show the fits to the low- and mid-J CO data.

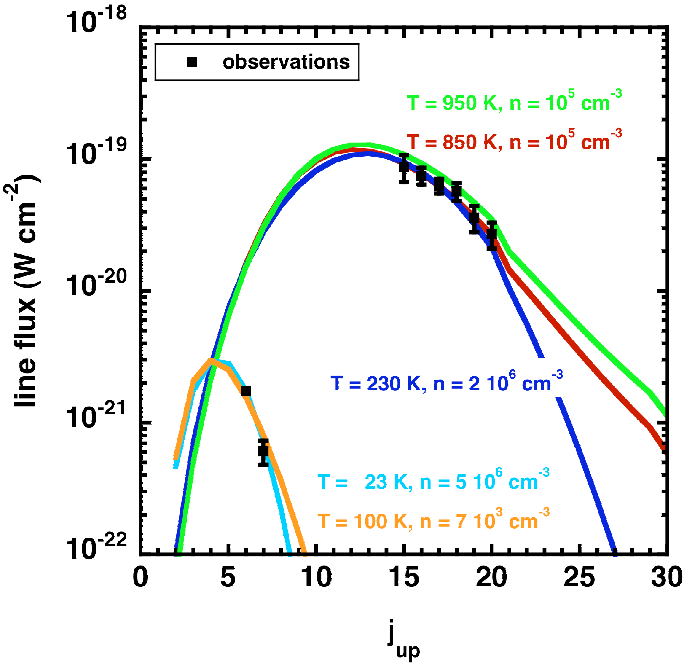

Figure 3.19: LVG model fits to CO-SED for the total integrated emission in HH211. Red, green and blue, show the LVG fits to the high$-J$ CO emission. Orange and light-blue lines are the LVG fits to the mid$-J$ CO emission.

have obtained. In general, the estimated outflow parameters are, within the typical errors that include also opacity effects, consistent with previous results for other class 0/I objects (see, e.g., results from CO (3–2) data by Curtis et al. 2010). A more detailed discussion on the comparison of the outflow properties for our full sample (low-, intermediate-, and high-mass protostars) will be given in a forthcoming paper.

3.9 Discussion

3.9.1 Comparison with Mid-IR observations

Mid-IR observations with Spitzer have been recently used as a tool to study shocks in a diverse type of objects (see, e.g. Reach et al. 2006, Smith et al. 2006). In the case of protostellar outflows, several low-mass protostars have been observed with the IRAC camera (e.g. Seale & Looney 2008). With four channels at 3.6, 4.5, 5.8 and 8.0 μm, the IRAC camera covers several H_2 transitions (indeed, several transitions per channel) that can be excited in shocked regions in outflows. In particular, H_2 emission has been found to dominate band 2 (4.5 μm) emission (Neufeld et al. 2009; De Buizer & Vacca 2010).

Spitzer/IRAC observations in L1448-mm have been presented previously by Tobin et al. (2007) and Neufeld et al. (2009). Such observations indicate that in fact H_2 transitions dominate the emission in all four IRAC bands. However, a particular behavior of the L1448-mm outflow is that the emission in the red lobe is considerably

Table 3.7: Outflow properties derived from the CO (6–5) emission

Vel range	δ_{max}	R_{max}	t_d	$M(H_2)$	F_m	E_k	L_{mec}
		(10^{-2})	(10^3)	(10^{-3})	(10^{-4})	(10^{43})	
	(km s^{-1})	(pc)	(yr)	($M_\odot$)	($M_\odot$ km s^{-1} yr^{-1})	(erg)	($L_\odot$)
L1448-mm							
Blue	69.5	19.0	2.67	16.7	4.34	80.3	2.44
Red	75.5	21.0	2.72	12.6	3.50	71.5	2.13
Total				29.3	7.84	152	4.57
IRS3							
Blue	24.5	4.87	1.94	3.46	0.436	2.07	0.086
Red	20.5	8.23	3.93	3.40	0.177	1.42	0.029
Total				6.86	0.613	3.49	0.115
HH211-mm							
Blue	23.2	5.80	2.45	1.62	0.154	0.871	0.029
Red	32.8	4.90	1.46	1.13	0.253	1.21	0.067
Total				2.75	0.407	2.08	0.096

weaker than the emission in blue lobe. A recent analysis by Giannini et al. (2011) performed on the H_2 line emission has proven that such a behavior is produced by a difference in the properties of the gas in each of the outflow lobes. These authors found higher densities in the northern (blue) lobe, with a density peak close to outflow tip and to the IRS3 source, with values close to 10^7 cm^{-3}. In contrast, the southern lobe was found with a more constant density values, which never exceeds $\sim$(1–2)$\times$ 10^6 cm^{-3}.

The CO (6–5) emission shows a similar morphology and brightness distribution to that of the mid-IR observations. Most of the CO (6–5) clumps have a counter-part in the mid-IR image of both HH211-mm and L1448-mm/IRS3. In particular, the clumps at the highest velocity range in L1448-mm are well positionally correlated with the apex of each of the ejection events clearly traced by the mid-IR emission (see, e.g., the blue-lobe in the top-left panel of Fig. 3.3). Also the CO (6–5) emission in L1448-mm seems to be weaker in the red-lobe than in the blue-lobe, as is the case for the mid-IR emission. The CO (6–5) clumps in HH211-mm also present a counter part in the mid-IR image, however a difference in the brightness distribution in red and blue lobes is not seen, neither in CO (6–5) nor in the mid-IR.

A more quantitative comparison can be done by contrasting the results of the rotational diagram analysis obtained from the mid$-J$ CO emission and from the pure rotational H_2 lines in the mid-IR. Although the mid-IR H_2 rotational lines are intrinsically tracing warmer gas than the sub-millimeter CO rotational lines, and thus different excitation conditions than the latter, a trend on the variation of the rotational temperature through different positions can be compared. By using IRS/Spitzer spectroscopy data Dionatos et al. (2009) have presented the mid-IR H_2 rotational diagram around four positions in L1448 (L1448-mm, B1, B2, and R1). We note that the rotational temperatures are similar in B1 and B2 as traced by

H_2 (∼630 K) and CO (∼40 K). On the other hand, at the R1 position the H_2 rotational temperature is higher at R1 (∼ 900 K) compared to B1 and B2, while in CO the rotational temperature at R1 is similar to that at B1 and B2. HH211-mm has been observed with IRS/Spitzer in H_2 pure rotational transitions by Dionatos et al. (2010). Three positions in HH211-mm can be compared with our results, namely B1-B2-B3, B7, and R6. We note that the highest rotational temperature determined from H_2 is towards the position of clump R6 (∼1100 K), while slightly lower temperatures are reported for B1-B2-B3 (∼ 860 K) and B7 (∼ 980 K). A similar trend is found from our analysis of the mid−J CO transitions, in which the rotational temperature is higher towards clump R6 (∼ 50 K) than towards B1-B2-B3 and B7 (both with $T_{rot} \sim 44$ K). We therefore see in both objects a similar trend in the change of the excitation condition as a function of position, as measured in our mid−J CO and in mid-IR pure rotational H_2 lines.

3.9.2 The CO (6–5) and (7–6) lines as tracer of the warm gas in outflows

The LVG results presented in sect. 7.2 may give support to recent studies in other outflow sources in which the CO-SLED is explained only by invoking multiple physical components. The profiles of the CO-SLED shown here for HH211-mm and L1448-mm are similar to that shown for HH46 by van Kempen et al. (2010b). In HH46, the CO-SLED has been fitted with at least three physical components by these authors, with the low−J and mid−J CO dominated by passive and UV heating. However, to clearly assess this possibility for the sources under study in this paper, complementary observations of higher−J CO transitions are needed. Particular useful will the observations of high−J CO transitions with Herschel that are under way in some of the key programs. However, despite the lack of these observations, the CO (6–5) and (7–6) APEX data presented here show the relevance of such transitions, since as seen from the CO-SLED, they are close to the peak of a relatively warm component likely dominated by the passive and/or UV heating (see also van Kempen et al. 2010b).

Another important characteristic of the CO (6–5) and (7–6) emission in the outflows under study is the fact that even at low velocities (i.e. close to the cloud velocity) the outflow region is still clearly seen, in contrast to low-J CO observations in which the low-velocity emission from the cloud drastically hide the low-velocity emission from the outflow. In the particular case of L1448-mm/IRS3, in which our observations provide a high enough spatial resolution, more CO clumps than the previously reported in low−J CO have been found through the CO (6–5) low-velocity emission. Some of these clumps may be related with the L1448-mm main outflow or with the outflows from the IRS3 system.

Finally, we have also shown that the CO (6–5) and (7–6) emission is a particular tracer of terminal bow shocks. In L1448-mm, the terminal bow-shock at R4-S position is brighter in CO (6–5) than in low−J CO observations. At the terminal bow-shock positions B7 and R6 in HH211-mm a similar behavior was found. From

the LVG calculations we have shown that at such positions a higher thermal pressure occurs, compared to other positions inside the outflow lobes.

3.10 Summary and conclusions

In the following we summarize the main results from this study:

- The CO (6–5)/(7–6) emission in L1448-mm/IRS3 and HH211-mm was found tracing the low- and high-velocity emission from the outflows related to those objects.
- The Extremely High Velocity emission in L1448-mm was detected in both CO (6–5) and (7–6) transitions from the clumps inside a radius of about 10" from the central object.
- High-velocity emission was detected in CO (6–5) around the central source in HH211-mm and also at the bow-shock positions.
- By a comparison with previous observations it has been found that the mid-J CO (6–5) and (7–6) emission is stronger towards the central region of L1448-mm than the low-J CO emission. Similarly, the terminal bow shocks in both objects are stronger in mid-J CO (6–5) and (7–6) than in low$-J$ CO.
- The LVG model that fits the mid$-J$CO emission in L1448-mm shows that the densities and kinetic temperatures of this EHV gas are, respectively, $n > 5\times10^5$ cm^{-3} and $T_{kin} > 1200$ K.
- A LVG analysis that includes far-IR CO lines from ISO shows that is not possible to fit simultaneously the mid$-J$ and high$-J$ CO lines with only one component, for both L1448-mm and HH211-mm outflows. This may support recent studies which propose multiple physical components to account for the CO-SLED around the central regions in protostellar outflows.
- In both outflows, even around the cloud velocity the outflow structures are clearly seen, in contrast with low$-J$ CO observations in which the low-velocity gas from the outflow is hidden by the emission from the cloud.
- Complementary observations of far-IR CO lines are needed to disentangle between the different emission components at work in protostellar outflows.

Chapter 4

Warm gas in protostellar outflows II. Intermediate-mass sources in OMC-2/3

4.1 Introduction

Intermediate-Mass (IM) protostars, i.e. protostars whose mass is in the range from 2 to 8 $M_{\odot}$, provide crucial information on the star formation process because they provide the link between low- and high-mass star formation (e.g. Crimier et al. 2010). IM protostars share some properties of massive protostars, such as their existence in clusters and their ability to ionize the surrounding gas. On the other hand, they present the advantage that they are more numerous and therefore located at closer distances ($\lesssim$1 kpc) than most of the massive star-forming regions and offer less complex spatial structures. Despite their relevance, very little is known about the formation and early evolutionary stages of IM protostars (e.g. class 0 type objects). Although some detailed studies have been conducted in the last years (e.g., Crimier et al. 2010; Beltrán et al. 2008; Takahashi et al. 2006; Fuente et al. 2007, 2001), little information is available in particular about outflows from class 0 type sources.

In the last few years observations have shown that outflows from IM protostars (hereafter IM outflows) share some characteristics of outflows from low-mass protostars, such as the high collimation factor in early evolutionary phases (Beltrán et al. 2008). On the other hand, in general, IM outflows are intrinsically more energetic than those driven by low-mass sources (Beltrán et al. 2008; Takahashi et al. 2008). The values of the outflow momentum rate, $F_{\rm out}$, are higher in IM protostars than in low-mass objects, which may be an indication that IM young stellar objects (YSOs) accrete material faster than the low-mass ones (Beltrán et al. 2008). However, in only few IM YSOs the outflows' physical conditions, such as kinetic temperature and density, have been determined (e.g., Cep-E and NGC2071: Lefloch et al. 2011; Chernin & Masson 1992; Hatchell et al. 1999). In these few cases, densities and temperatures seem to be similar to those found in low-mass outflows (>100 K and

$>10^4$). Clearly, studies toward larger samples and in higher excitation lines are needed to properly determine how these quantities compare with the low-mass case.

In a previous paper (Gómez-Ruiz et al. 2011a; hereafter Paper I), we have presented a study of the CO (6–5) and (7–6) emission (throughout the paper referred to as mid$-J$ CO transitions) in two low-mass class 0 outflows, namely L1448 and HH211. In both objects we found the CO (6–5) and (7–6) emission tracing terminal bow-shocks and also high-velocity emission likely related with the jet component. In the case of L1448, extremely high velocity emission (EHV), i.e. emission at relative velocities >50 km s^{-1} with respect to the cloud velocity, was detected in both transitions. When determining the excitation conditions we found that indeed the EHV emission shows higher excitation than the high-velocity emission. In addition, by performing a large velocity gradient (LVG) analysis, we infer that the gas related with the outflow structures is dense ($>10^5$ cm^{-3}) and warm (T$>$ 200 K). Also from the LVG modeling, we determined the thermal pressure along the outflow lobes. In L1448 we found higher thermal pressure values towards EHV gas (i.e. jet component) and the bow-shock region. Based on the LVG results and the position-velocity distribution of the emitting gas, we concluded that these mid$-J$ CO transitions are good tracers of molecular material likely related to the primary jet and the highly excited bow-shock region in protostellar outflows.

In the present paper we extend the study of mid$-J$ CO emission to outflows from IM protostars in the Orion molecular cloud-2/3 (OMC-2/3), including Class 0 and I type objects. The main purpose of this paper is to study the distribution of the CO (6–5) and (7–6) emission in comparison with lower$-J$ CO transitions, and combine all such data to determine the excitation and physical conditions of IM outflows as traced by these mid$-J$ CO transitions. Finally, we compare these results with our previous observations of low-mass outflows. This paper is organized as follows. In sect. 2 and sect. 3 we introduce the regions we have selected and the APEX observations we have performed on them, respectively. In sect. 4 and sect. 5 we show the results we have obtained and provide a comparison with previous observations. In sect. 6 and sect. 7 we present the calculation of the excitations, physical conditions and outflow properties. In sect. 8 we discuss our results and in sect. 9 we present a summary and conclusions.

4.2 The target regions

OMC-2/3 is located north of the larger Orion Molecular Cloud 1 complex (OMC 1) at a distance of $\approx$ 400 pc (Menten et al. 2007). This region is one of the nearest cluster-forming sites that includes intermediate-mass protostars (e.g. Takahashi et al. 2006, 2008, here after T08). In this region, filamentary molecular clouds were discovered in the millimeter/sub-millimeter continuum observations with the IRAM-30m telescope and the JCMT (Chini et al. 1997; Johnstone & Bally 1999). Within the filaments, millimeter/sub-millimeter continuum sources are found, presumably tracing prestellar and protostellar cores (e.g Chini et al. 1997, T08). Follow-up CO

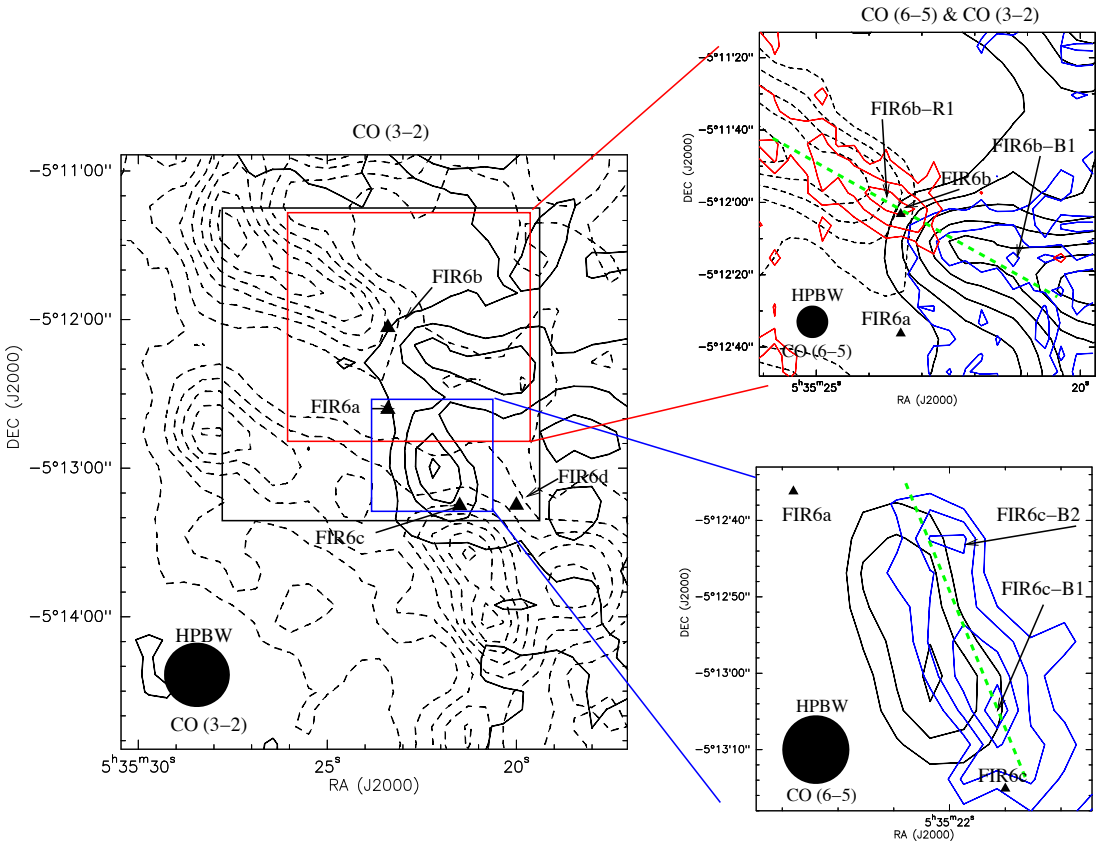

Figure 4.1: The OMC-2 FIR 6 region. *Left*: CO (3–2) high-velocity emission from T08. The velocity ranges are from -4 to +7 km s^{-1} for the blue-shifted emission (solid contours) and from +14 to +22 km s^{-1} for the red-shifted emission (dashed contours). First contour and contour spacing is 5σ, with σ =1.5 K km s^{-1} for blue-shifted emission and σ =1.0 K km s^{-1} for red-shifted emission. The black square shows the whole field covered by the CO (6–5) and (7–6) observations. The velocity ranges in this panel were chosen to best display the outflow structures of the whole region, however the exact velocity ranges of each outflow is different. The two right panels described next show the real velocity range of each outflow. *Upper-Right*: CO (6–5) high-velocity emission (blue and red contours) overlaid on the CO (3–2) emission (black solid and dashed contours). The velocity ranges, for both transitions, are from +4 to +8 km s^{-1} for the blue-shifted emission and from +14 to +30 km s^{-1} for the red-shifted emission. First contour is 3σ for CO (6–5) and 5σ for CO (3–2), while contour spacing is 2σ for both transitions (σ =2.4 K km s^{-1} for CO (6–5) and 2.5 K km s^{-1} for CO (3–2)). *Lower-Right*: same as *Upper-Right* but for the blue-shifted emission from -12 to +4 km s^{-1} (σ =2.4 K km s^{-1} for CO (6–5) and σ =1.0 K km s^{-1} for CO (3–2)). Black contours for CO (3–2) and blue contours for CO (6–5). Note that the red-shifted emission is not shown in *Lower-Right* panel, since our map did not cover the red-shifted lobe of FIR 6c outflow. The cloud velocity is at V$_{LSR}$ =11 km s^{-1}. Filled triangles show the positions of the continuum sources FIR 6a, 6b, 6c, and 6d (positions taken from T08). In the right panels also the CO (6–5) outflow peaks area marked, named FIR 6b-B1, FIR 6b-R1, FIR 6c-B1, and FIR 6c-B2 (see text). The green dashed lines show the PV cuts discussed in sect. 6.

and H_2 molecular line observations have revealed the presence of a number of outflows originated from some of the continuum sources (T08; Yu et al. 1997; Aso et al. 2000; Stanke et al. 2002; Williams et al. 2003). One of the most extensive molecular outflow surveys in the OMC-2/3 region has been conducted by T08. By observing the CO (3–2) transition with ASTE, these authors have reported 14 molecular outflows, indicative of a high ongoing star formation activity in this region.

From the CO (3–2) outflow survey of T08 and its follow-up observations, we have selected the most promising sources in terms of outflow activity (bipolar morphology and high-velocity emission) and early evolutionary stage (class 0 type sources). Under these criteria, the regions around FIR 6 in OMC-2 and MMS 1-6 in OMC-3 (hereafter OMC-2 FIR 6 and OMC-3 MMS 1-6, respectively) have been selected for follow up observations in mid$-J$ CO lines. For these sources, T08 derive luminosity ranges of 6–251 and 9–150 $L_{\odot}$, respectively, which makes them very likely IM protostars. The large uncertainties of the luminosities of these sources results from their poorly determined spectral energy distributions (SEDs). The envelope masses determined by T08 (> 3 $M_{\odot}$) are consistent with values for IM protostars.

OMC-2 FIR 6 contains at least four millimeter continuum sources named FIR 6a, 6b, 6c, and 6d (Fig. 4.1). T08 have reported FIR 6b source as being likely a Class I type object, based on their SED, while the rest of sources do not have sufficient information to clearly assess their evolutionary status. The CO (3–2) data towards OMC-2 FIR 6 region revealed that two molecular outflows are driven by FIR 6b and 6c (see Fig. 4.1). As a follow-up study, Shimajiri et al. (2009) observed the OMC-2 FIR 6 region with the Nobeyama Millimeter Array in the 3 millimeter continuum, CO (1–0), and SiO (2–1) transitions. The two outflows found in CO (3–2) were confirmed in CO (1–0), in addition to a third outflow emanating from FIR 6d. The SiO (2–1) emission was found only at the blue-lobe of FIR 6c outflow, but no SiO emission was clearly detected towards FIR 6b outflow. From the line ratio between the CO (3–2) and (1–0) transitions it has been found that kinetic temperatures in the outflow lobes are $\sim$50 K (T08; Shimajiri et al. 2009).

The OMC-3 MMS 1-6 region consists of six millimeter continuum sources named MMS (Fig. 4.3). A clear identification of the evolutionary status through the SED has been given for MMS 2 and MMS 5, which are class I and class 0 type, respectively (T08; Takahashi et al. 2009). T08 have reported clear bipolar outflow morphologies originated from MMS 2 and MMS 5 in the CO (3-2) emission. In the case of MMS 6, no clear star formation signatures such as large scale molecular outflow and ionized jets are detected (T08 Matthews et al. 2005; Takahashi et al. 2009). However, the latest sub-arcsec observations with the SMA by Takahashi & Ho (2012) have revealed the extremely compact molecular outflow (lobe size of $\approx$800 AU) associated with the continuum peak, MMS 6-main. Furthermore, Takahashi et al. (2012b) reported that the continuum main peak, MMS 6-main, is most likely in the protostellar phase. No clear molecular outflow signatures are detected in other MMS sources, so that they are likely in the prestellar phase.

Table 4.1: Transitions observed.

Line	ν_0 GHz	A 10^{-5} s^{-1}	E_u/k K	HPBW ”
CO (6–5)	691.473	2.137	116.16	9.0
CO (7–6)	806.651	3.422	154.87	7.7
^{13}CO (6–5)	661.067	299.0	111.05	9.4
SiO (5–4)	217.107	51.96	31.26	30.5

Table 4.2: Source information and map rms.

Source	α(J2000) (^{h} ^{m} ^{s})	δ(J2000) (° ′ ″)	RMS (K)[a] ^{12}CO (6–5)	^{12}CO (7–6)	SiO (5–4)
OMC-2 FIR 6b	05:35:23.4	−05:12:03	0.73	3.0	0.05
OMC-3 MMS 5	05:35:22.5	−05:01:15	0.55	1.9	-

[a]Average rms (T_{MB}) in a channel map of 1.0 km s^{-1}.

4.3 APEX observations

4.3.1 CHAMP+ observations

Submillimeter observations towards OMC-3 MMS 1-6 and OMC-2 FIR 6 were performed with the MPIfR principal investigator (PI) instrument CHAMP+ (Kasemann et al. 2006) on the APEX telescope (Güsten et al. 2006) during 2008 November and 2010 July, respectively. CHAMP+ is a dual-color 2 × 7 pixels heterodyne array for operation in the 450 μm (low frequency array, LFA) and 350 μm (high frequency array, HFA) atmospheric windows. The optics allow simultaneous observations in both colors. Both sub-arrays present an hexagonal arrangement. The front-end was connected to a Fast Fourier Transform Spectrometer (FFTS, Klein et al. 2006).

The CO (6–5) and (7–6) lines were mapped simultaneously in the On-The-Fly (OTF) mode, with an ON time of 0.5 seconds per position, with steps of 3″. For OMC-2 FIR 6 a map of 60″×120″ was centered at the position of the FIR 6b source, while for OMC-3 MMS 1-6 a map with of 280″×150″ was centered at the position of MMS 5. Additional single-pointing observations were done on two selected positions of OMC-2 FIR 6 (called FIR 6b and FIR6c-B1) in a third setup consisting of ^{13}CO (6–5) and HCO^+ (9–8). No emission was detected in the HCO^+ (9–8) line, with upper limits of 186 mK (T_A^*). For all observations, the backend was set to provide a total bandwidth of 2.8 GHz divided in 8192 channels for each pixel. The final spectra were re-sampled to 1.0 km s^{-1} spectral resolution for all transitions in both sources.

During the observations, the precipitable water vapor (PWV) was in the range of 0.3 to 0.7 mm. The pointing was determined by CO (6–5) cross-scan observations on IK Tau. Pointing corrections were always within 3″. Focus was checked on Jupiter

and Mars. The calibration was done by observing hot and cold loads. In our observations the OFF position was not checked for emission, however this position was selected, in most of the cases, to avoid regions known to present emission in low$-J$ CO transitions, and therefore reasonable free of emission, as can be inferred from the results present below. However, due to a different selection of the OFF position during the ^{13}CO(6–5) and HCO$^+$(9–8) single-pointing observations of the FIR 6b position, contamination of the OFF position was found in its spectra (see below). Since FIR 6c-B1 position was observed afterwards, the correct OFF position was selected and thus likely not affected by such contamination. Standard data reduction procedures such as flagging bad spectra and base line subtraction were done with CLASS, while images were produced with the XY-MAP task in GReG, both programs being part of the GILDAS software [1]. The griding procedure in XY_map was made to provide a final resolution equal to the HPBW of the telescope at the observed frequency. Table 4.1 and 4.2 show a summary of the observations, including the observed transitions, their corresponding HPBW, and the coordinates (right ascension and declination) of the central positions of the maps presented in this paper.

The images and spectra are presented in main beam brightness temperature scale, $T_{MB} = T_A^*/\eta_{MB}$ ($\eta_{MB} = \eta_s/F_{eff}$), for which we have used a forward efficiency (F_{eff}) of 0.95 and a beam coupling efficiency (η_s) measured on Jupiter. During the OMC-2 observations the measured η_s was 0.48 for both LFA and HFA, while during the OMC-3 observations η_s was 0.48 and 0.45 for LFA and HFA, respectively. The rms noise levels are summarized in Table 4.2.

4.3.2 APEX-1 observations

Complementary mapping observations in the SiO (5–4) line were done towards OMC-2 FIR 6 with the APEX-1 facility instrument during 2010 September. The receiver is connected to a FFTS that provides a bandwidth of 1 GHz and 4096 channels, which at the rest frequency of SiO (5–4) resulted in a spectral resolution of 0.3 km s^{-1}. The OTF map with a size of $70'' \times 70''$, in steps of $9''$, was centered at the position of the FIR 6b source. The pointing accuracy was checked by CO (2–1) cross-scan observations on IK Tau. Pointing corrections were always within $5''$. The focus was checked on Jupiter and Mars. The calibration was done by observing hot and cold loads. The data reduction and image processing is similar to the procedure described for the CHAMP+ observations, using CLASS and GReG. The final spectra were re-sampled to 1.0 km s^{-1} spectral resolution. In order to convert to T_{MB} scale, the instrumental (or nominal) values of 0.95 and 0.75 we adopted as forward and beam coupling efficiency, respectively.

[1] http://iram.fr/IRAMFR/PDB/gildas/gildas.html

Table 4.3: Outflow peak positions.

Position	α(J2000) ($^{\rm h}$ $^{\rm m}$ $^{\rm s}$)	δ(J2000) ($^\circ$ $'$ $''$)	v_{min}/v_{max} (km s^{-1})
FIR 6b-B1	05:35:21.2	−05:12:15	0/8
FIR 6b-R1	05:35:23.7	−05:11:59	14/30
FIR 6c-B1	05:35:21.6	−05:13:00	-16/8
FIR 6c-B2	05:35:21.7	−05:13:00	-10/8
MMS 5-B1	05:35:21.3	−05:01:16	-95/7
MMS 5-R1	05:35:22.5	−05:01:14	16/75
MMS 2-B1	05:35:18.2	−05:00:32	-12/7
MMS 2-R1	05:35:17.7	−05:00:34	16/30

4.4 CO outflows in OMC-2 FIR 6 and OMC-3 MMS 1-6

In order to define the outflow velocity range, we use the CO (6–5) channel maps and the spectra taken at different outflow positions. We define the lower boundary limit (v_{min}) by looking for outflow morphologies clearly separated from the ambient diffuse emission. At higher velocities it is usually difficult in the channel maps to distinguish the outflow emission since it is relatively weaker than at lower velocities, i.e. velocities closer to the systemic LSR velocity. An integrated spectrum of the whole outflow lobe provides a first guess of the upper boundary limit (v_{max}). An integrated intensity map inside these boundary limits reveals the emission peaks within the lobes. From the spectra taken at the positions of these peaks we can finally establish v_{max}. In our case, v_{max} is defined as the velocity in which the emission in the spectrum drops below the 3σ level. The velocity limits for all identified outflows as well as the positions of the outflow peaks are reported in Table 4.3. Throughout the paper we assume the LSR velocity (V_{LSR}) of the cloud as 11 km s^{-1}, and the terms "high-velocity" and "outflow emission" refer to the emission with velocities within the range defined by v_{min} and v_{max} as defined in Table 4.3.

4.4.1 CO (6–5) in OMC-2 FIR 6

Figure 4.1 shows the CO (6–5) emission detected in the FIR 6 region, integrated along the blue- and red-shifted wings. Figure 4.1 also shows the CO (3–2) wing emission from T08. We have found the two outflows related to FIR 6b and FIR 6c, reported previously in CO (3–2) by T08. Both outflow lobes from FIR 6b are detected in CO (6–5), as is also the blue-shifted lobe from FIR 6c (the red-shifted lobe was not covered by our map). The CO (6–5) outflow emission from FIR6b seems to peak closer to the central source than the CO (3–2) one. Convolving to the CO (3–2) beam, confirms this tendency. On the other hand, the peak position of the CO (6–5) emission in the blue lobe of FIR 6c outflow is close to the location

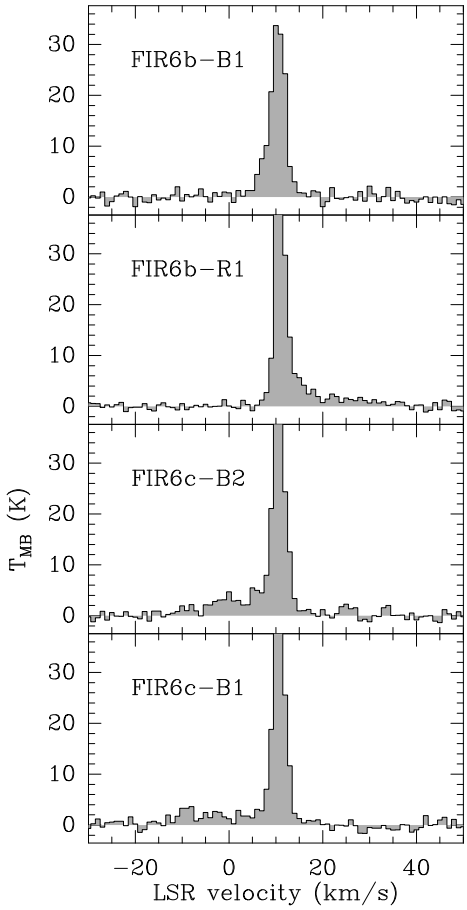

Figure 4.2: CO (6–5) sample spectra at selected positions within FIR 6 outflows. The spectral resolution is 2 km s^{-1}. The positions are indicated in the top-left corner of each panel.

of the CO (3–2) emission peak. The CO (6–5) emission from FIR 6b outflow is seen from V_{LSR} = +3.0 to +30 km s^{-1}, while the blue-shifted CO (6–5) emission of the FIR 6c outflow reaches up to a V_{LSR} of −15.0 km s^{-1}. No high-velocity emission tracing outflows from FIR 6a and FIR 6d was found.

Figure 4.2 shows a sample of spectra at different positions within the lobes of FIR 6b and FIR 6c outflows. The spectra were taken at the position of the emission peak of each lobe. In the case of the FIR 6c outflow, since two (blue-shifted) peaks were found at different positions (named FIR 6c-B1 and FIR 6c-B2 in Fig. 4.1), we show the spectra at each of the two positions in Fig. 4.2. In all the positions, the peak of the CO (6–5) emission is found at the cloud systemic velocity (V_{LSR} =11.0 km s^{-1}). Another spectral component is identified by the wings and/or secondary peaks at high-velocities. At the peak position in the red lobe of the FIR 6b outflow a broad wing is noticed up to velocities of V_{LSR} = 30 km s^{-1}. On the other hand, at the peak of the blue lobe there is no evidence for a broad wing, with the emission reaching velocities only up to V_{LSR} =3 km s^{-1}. At the FIR 6c-B1 and FIR 6c-

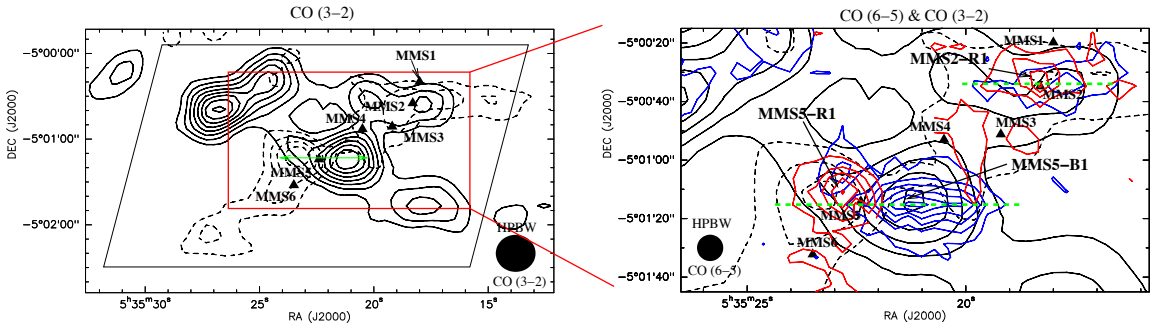

Figure 4.3: The OMC-3 MMS 1-6 region. *Left*: CO (3–2) high-velocity emission from T08. The velocity ranges are from -4 to +7 km s^{-1} for the blue-shifted emission (solid contours) and from +14 to +22 km s^{-1} for the red-shifted emission (dashed contours). First contour is 6σ and contour spacing is 3σ, with σ =1.5 K km s^{-1}, for blue-shifted emission, and σ =1.0 K km s^{-1}, for red-shifted emission. The green arrow shows the direction of outflow from MMS 5 source. The black square shows the whole field on which the CO (6–5) and (7–6) observations were done. *Right*: CO (6–5) high-velocity emission overlaid on the CO (3–2) emission from the left panel. The velocity ranges are from -25 to +7 km s^{-1} for the blue-shifted emission (blue contours) and from +16 to +31 km s^{-1} for the red-shifted emission (red contours). First contour is 3σ and contour spacing is 2σ, with σ =2.4 K km s^{-1} for both blue-shifted and red-shifted emission. On both panels the filled triangles show the position of the continuum sources reported by T08. The green dashed lines show the PV cuts discussed in §6.

B2 positions, secondary peaks are recognized at high-velocities. At the FIR 6c-B2 position the secondary peak is found at V_{LSR} =0 km s^{-1}, while at FIR 6c-B1 the secondary high-velocity peak is found at $V_{LSR} = -10$ km s^{-1}.

4.4.2 CO (6–5) in OMC-3 MMS 1-6

In Fig. 4.3 we show the region covered by our CO (6–5) and (7–6) maps. We have clearly identified CO (6–5) outflow emission originating from the sources MMS 5 and MMS 2. These two outflows were previously reported by T08. No clear evidence of outflow activity towards the remaining MMS objects was found. The outflow emanating from MMS 5 seems to be orientated along the East-West direction, while for the outflow from MMS 2 the observations can not clearly disentangle a tendency in the outflow direction. The most intense CO (6–5) emission is related to the MMS 5 outflow. A close-up view of this outflow is presented in Fig. 4.3, showing the extended and relatively highly collimated structure of the blue lobe. On the other hand, the red lobe shows a more compact structure.

The most important result from our CO (6–5) observations is the detection of EHV emission from the MMS 5 outflow. The EHV range is defined as V_{LSR} =-95 to -80 km s^{-1} for the blue-shifted lobe and V_{LSR} =60 to 70 km s^{-1} for the red-shifted lobe. In Fig. 4.4 we show the velocity integrated emission in the EHV range and also the spectra taken at the position of the peak intensity of the EHV structures. The

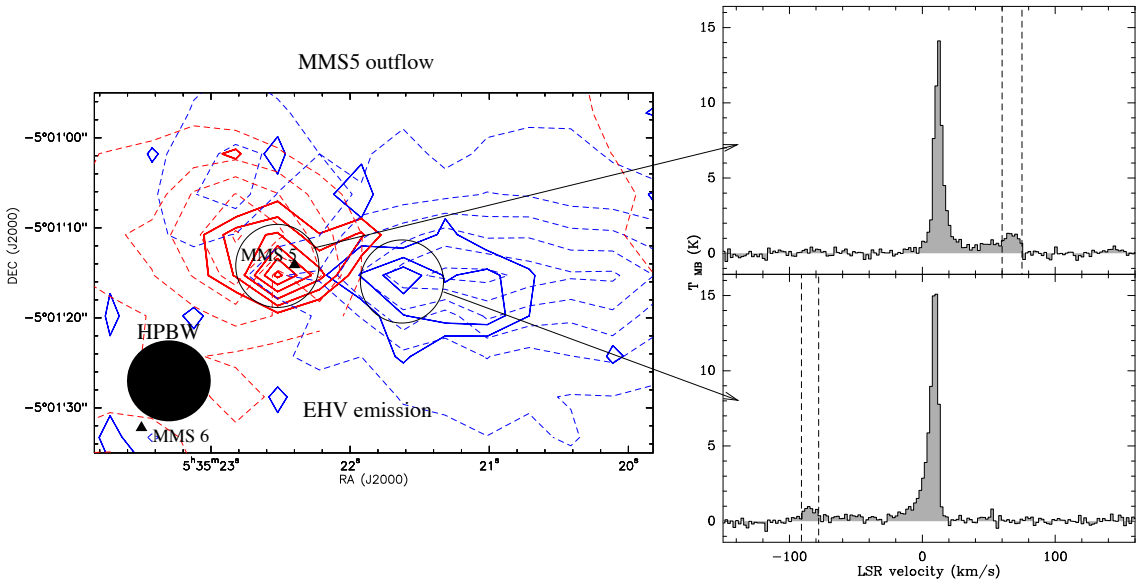

Figure 4.4: *Left:*The EHV CO (6–5) emission from MMS 5 outflow. Solid blue contours show the CO (6–5) emission integrated from V_{LSR} =-95 to -80 km s^{-1} (blue-shifted EHV range), while the solid red contours show the CO (6–5) emission integrated from V_{LSR} = 60 to 70 km s^{-1} (red-shifted EHV range). Contour spacing is 2.2 K km s^{-1} (σ), with the first contour at 6.6 K km s^{-1} (3σ). The dashed contours show the high-velocity CO (6–5) emission as presented in Fig. 4.3. *Right:* CO (6–5) spectrum taken at the positions indicated by the circles (see Table 4.3 for the coordinates of the center of the circles). The vertical lines show the boundaries of the EHV range.

integrated intensity maps show that the EHV emission is concentrated to within few arc-sec of MMS 5. The CO (6–5) spectra clearly show secondary peaks related to these EHV features, with the red-shifted EHV component stronger than the blue-shifted one. The compact morphology and the characteristic line profile suggest that these components are the equivalent of the so-called EHV bullets found in class 0 low-mass outflows (e.g. L1448-mm: Bachiller et al. 1990, paper I).

4.4.3 ^{13}CO (6–5) and CO (7–6)

In OMC-2 FIR 6 the CO (7–6) emission was detected only at low velocities, from V_{LSR} = 8 to 14 km s^{-1}. The emission was found mainly tracing the diffuse cloud emission, with the outflow morphologies barely seen. On the other hand, CO (7–6) high-velocity emission was detected in the MMS 5 and MMS 2 outflows. However, the EHV component from the MMS 5 outflow was not found. In Fig. 4.5 we show the CO (7–6) emission integrated over the blue- and red-shifted wings. Both outflow lobes from MMS 5 are seen, showing a similar structure as traced by CO (6–5). In the case of the MMS 2 outflow, the CO (7–6) high-velocity emission is coming mainly from the red-shifted lobe.

In Fig. 4.6 we show the ^{13}CO (6–5) spectra taken at two positions within the FIR 6 region: the FIR 6b source and FIR 6c-B1. As in the case of the CO (7–6) emission, ^{13}CO (6–5) emission is only detected at low velocities. All spectra in Fig. 4.6 show the emission to peak at the systemic velocity (V_{LSR} =11 km s^{-1}), with a FWHM of ∼2 km s^{-1}. However, important to note is that at the FIR 6b position an absorption feature is also present at the V_{LSR} =9 km s^{-1}, which is more evident in the external pixels. As described in the observation's section, this absorption feature is likely due to contamination from the OFF position, and thus then ^{13}CO (6–5) emission detected at the FIR 6b position should be taken as lower limit.

Based on the ^{13}CO (6–5) observations, we estimate the ^{12}CO (6–5) opacity at the FIR 6b and FIR 6c-B1 positions. We follow the formulation introduced in Paper I, in which under the assumption that the ^{13}CO emission is optically thin and that ^{12}CO and ^{13}CO have the same excitation temperature, the ^{12}CO to ^{13}CO line ratio gives the ^{12}CO opacity, τ_{12} (see equation 1 of Paper I). As we have reported above, the ^{13}CO (6–5) was detected only in two or three 1 km s^{-1} wide channels around the cloud velocity. The ^{12}CO to ^{13}CO line ratios for the 10, 11, and 12 km s^{-1} channels are, respectively, 8.6, 4.8, and 7.3 for the FIR 6b position, and 10.1, 7.5, and 18.2 for the FIR 6c-B1 position. Our opacity calculations were made assuming a [^{12}CO]/[^{13}CO] abundance ratio of 62 (Langer & Penzias 1993). Line ratios of 5, 10, and 20 gives τ_{12} of ∼ 12, 6 and 3, respectively. Therefore we see that at the cloud velocity the ^{12}CO is optically thick, while at the adjacent channels the emission can only be moderately optically thick. On the other hand, upper limits in the outflow velocity range suggest that the emission can be optically thin. For example, in FIR 6c at V_{LSR} =1 km s^{-1} the line ratio is >50, which means that τ_{12} is <0.4. A similar line ratio (>50) is found at V_{LSR} =14.0 km s^{-1} in FIR 6b, suggesting also that τ_{12} is <0.4. Based on these results, in the following calculations to determine the outflow

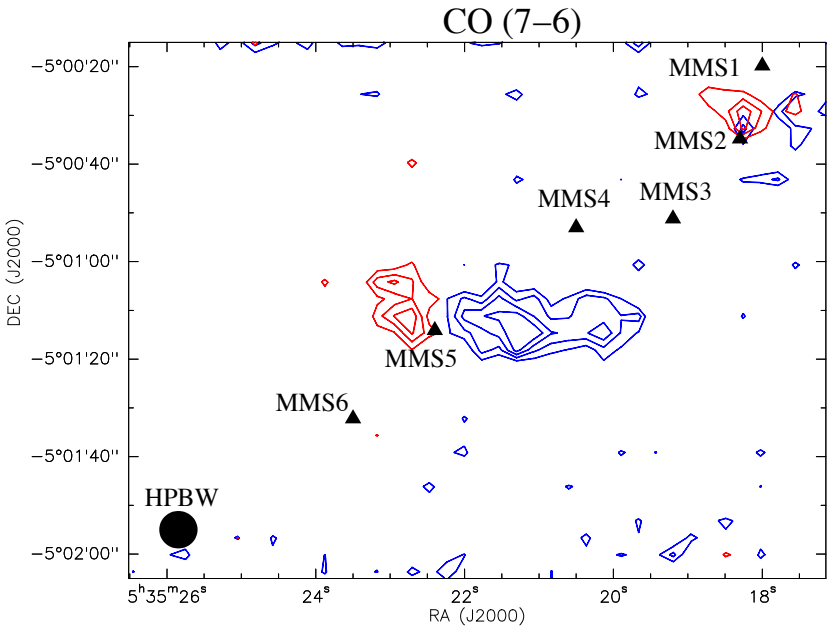

Figure 4.5: The CO (7–6) high-velocity emission map centered at MMS 5 source. Blue and red contours show the blue- and red-shifted high-velocity emission, respectively. Contour spacing is 1σ, with 3σ as the first contour (σ=7.4 K km s^{-1} for blue-shifted emission and σ =6.7 K km s^{-1} for red-shifted emission). Filled triangles show the position of the MMS sources.

excitation and properties we assume that the ^{12}CO (6–5) high-velocity emission is optically thin in the FIR 6 outflows. Although we did not observe the ^{13}CO (6–5) line in MMS 1-6 region and therefore we are not able to estimate the ^{12}CO opacity, we will also assume that the ^{12}CO (6–5) high-velocity emission from the outflows in that region is optically thin.

4.5 The SiO emission in OMC-2 FIR 6

Contrary to the case of the CO (6–5) and (7–6) emission, the angular resolution (∼30″) of the SiO (5–4) observations is not sufficient to allow a clear identification of outflow structures and thus properly define the outflow velocity range. However, since the SiO molecule is known to be an exclusive shock tracer (e.g., Gusdorf et al. 2008a), in principle any emission from this molecule may be related to outflows and/or jets. From the integrated SiO (5–4) intensity map shown in Fig. 4.7a we can see the overall distribution of the SiO (5–4) emission in the region. As seen from the Fig. 4.7a, the SiO emission is located towards the region that corresponds to the blue-lobe of FIR 6c outflow. In Fig. 4.7b we show the SiO (5–4) spectrum averaged over the area in which the emission is detected (green polygon in Fig. 4.7), which shows that the emission extends in velocity (V_{LSR}) from ∼-12 to +15 km s^{-1}.

Previous interferometric SiO (2–1) observations by Shimajiri et al. (2009) showed

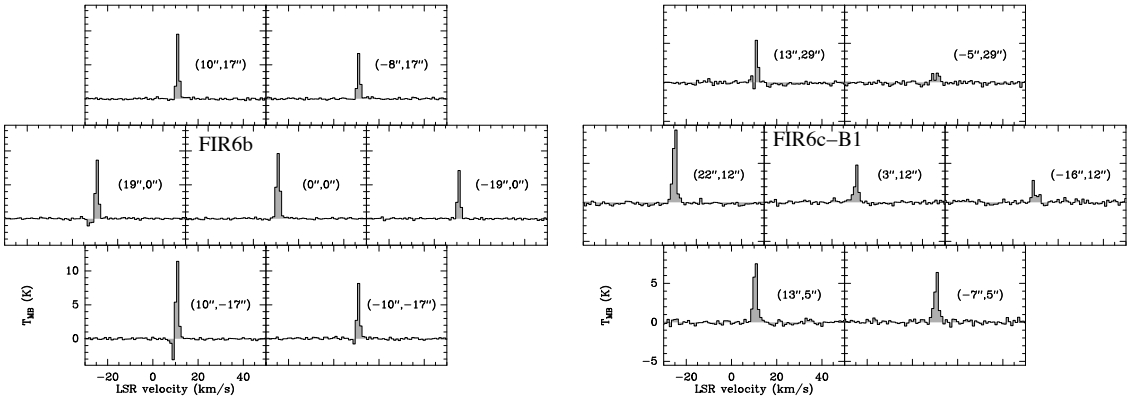

Figure 4.6: ^{13}CO (6–5) spectra taken at selected positions within FIR 6 region. The figure shows the seven CHAMP+ pixels for each pointing observation. *Left:* observation centered on the FIR 6b source (offset labels given with respect to FIR 6b source). *Right:* observation centered on the FIR 6c-B1 position (offset labels given with respect to FIR 6c source).

a similar distribution to what we have found in our APEX SiO (5–4) observations. As in our case, the SiO (2–1) emission was found only towards the region that corresponds to the blue-lobe of FIR 6c outflow. Our somewhat larger map confirms that no SiO emission is clearly detected from the FIR 6b outflow, at the rms of our observations ($T_A^* = 40$ mK). There are at least four scenarios that can explain the non-detection of SiO from the FIR 6b outflow. (1) Neither our SiO (5–4) observations nor the SiO (2–1) observations by Shimajiri et al. (2009) covered the outflow tips, were we expect to see the terminal bow shocks. Since the SiO emission in protostellar outflows is seen from both the high-velocity emission close to the central source and from terminal bow shocks (Dutrey et al. 1997; Gusdorf et al. 2011), it is likely that SiO emission may be present at the outflow tips that were not covered by the observations. (2) The SiO (2–1) and (5–4) observations were not sensitive enough to detect the emission. This is unlikely since our SiO (5–4) observations are sensitive to column densities of few 10^{12} cm^{-2}. This means we should have seen at least the weakest SiO outflows reported in the literature (see, eg. Martin-Pintado et al. 1992b). (3) The FIR 6b source is a more evolved young stellar object compared with FIR 6c, probably in the class I stage. Observations and models show that the SiO molecule does not survive up to the time scales of class I objects (Gusdorf et al. 2008a), thus the non-detection of SiO in FIR 6b outflow indicates its more evolved evolutionary status. Indeed, based on multi-wavelength data, T08 have classified FIR 6b as a class I object. (4) The associated shock is not powerful enough to release Si or SiO from the grain mantles and therefore no SiO is formed in the outflow. Based on the results of T08, we may favor scenario in which the SiO emission is not seen from the FIR 6b outflow because its driving source is a class I object. However, we can not rule out the possibility of SiO emission at the terminal bow shocks that have not been observed yet.

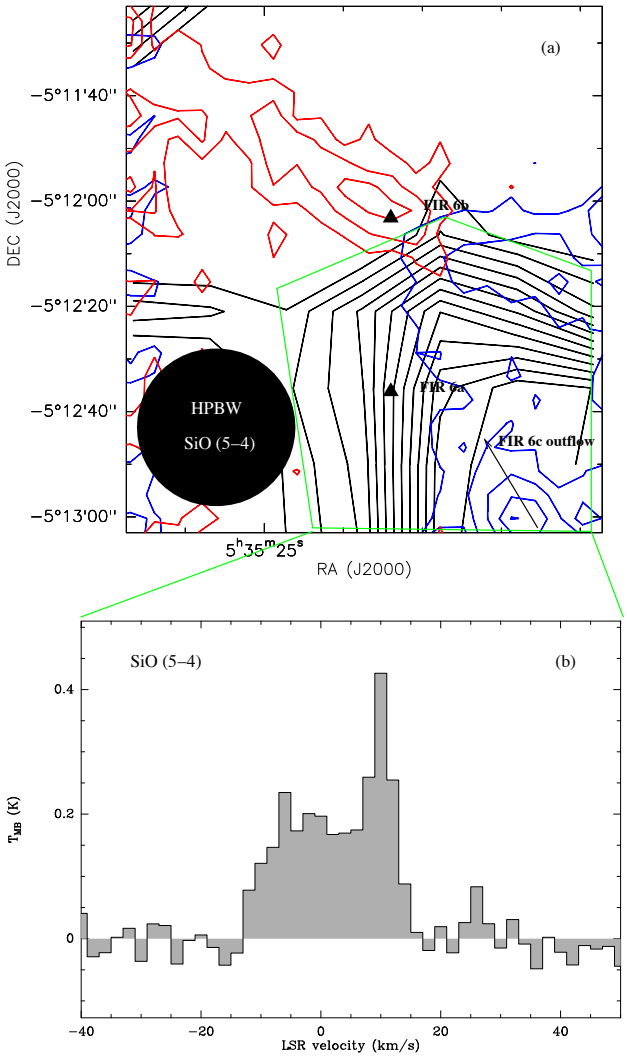

Figure 4.7: (a) SiO (5–4) emission integrated from -12 to 15 km s^{-1} (black contours) overlaid on the CO (6–5) outflow emission (blue and red contours). SiO contour step is 1σ, with the first contour at 3σ (σ=0.38 K km s^{-1}). Blue and red contours are the same as in Fig. 4.1. Note that, except for the noise edges, the whole field observed in SiO (5–4) is included in this image. (b) SiO (5–4) spectrum averaged over the region indicated by the green polygon. The spectral resolution has been smoothed to 2 km s^{-1}.

Table 4.4: CO integrated intensities at selected positions[a].

Position	Velocity (km/s)	$\int T_{MB}dv(\sigma)$ (K km s^{-1})		
	(v_{min}/v_{max})	3–2	6–5	7–6
FIR 6b-B1	0/8	32.0(1.5)	17.3(1.2)	<4.3
FIR 6b-R1	14/30	21.8(1.2)	26.9(1.2)	19.5(3.5)
FIR 6c-B1	-16/8	23.4(1.1)	27.3(1.8)	20.1(5.3)
FIR 6c-B2	-10/8	33.3(1.4)	39.2(0.8)	19.7(4.9)
MMS 5-B1	-25,7	35.7(1.9)	60.8(1.4)	42.2(3.5)
	-95/-75	<9.9	10.8(1.1)	3.3(2.8)
MMS 5-R1	16,31	5.9(1.8)	16.1(1.1)	7.7(2.4)
	60/75	<7.4	14.4(1.1)	7.5(2.4)
MMS 2-B1	-12/7	16.0(1.6)	18.4(1.2)	11.8(2.9)
MMS 2-R1	16,30	9.1(1.4)	10.8(0.9)	7.9(2.5)
	31/50	<7.5	6.6(1.1)	<2.9

a) Data convolved to 26″ ASTE beam (i.e. CO (3–2) transition).

4.6 Outflow kinematics

In order to have an overall view of the kinematics of the outflowing gas, in Fig. 4.8 we show the position-velocity (PV) diagrams of the CO (6–5) emission obtained along the axes drawn in figures 4.1 and 4.3. In these PV plots, the high-velocity structures are clearly distinguishable from the ambient emission (the main high-velocity structures are labeled in Fig. 4.8). In the case of the OMC-3 MMS 5 outflow one can clearly see that the EHV features are located close to the central source, and in the red-shifted lobe we notice a trend of decreasing velocity going further away from the center. The other interesting case is the OMC-2 FIR 6c outflow, in which the velocity of the gas increases going further away from the FIR 6c source, i.e. opposite to the trend seen in MMS 5 outflow. The tendency of high-velocity towards larger distance from the central object has been observed in other objects, but so far lacks a satisfactory explanation (see, e.g., the case of NGC2071 in Chernin & Masson 1992). The OMC-2 FIR 6b and OMC-3 MMS 2 outflows show a more "standard" velocity distribution, better exemplified in the red lobe of FIR 6b outflow in which the high-velocity emission in mostly concentrated towards the central object with additional structures at lower velocities further away from the center. In general, with the exception of the OMC-2 FIR 6c outflow, the position-velocity structures of the outflows presented here are consistent with the scenario of jet-driven outflows as in low-mass protostars (see, e.g., Lee et al. 2000).

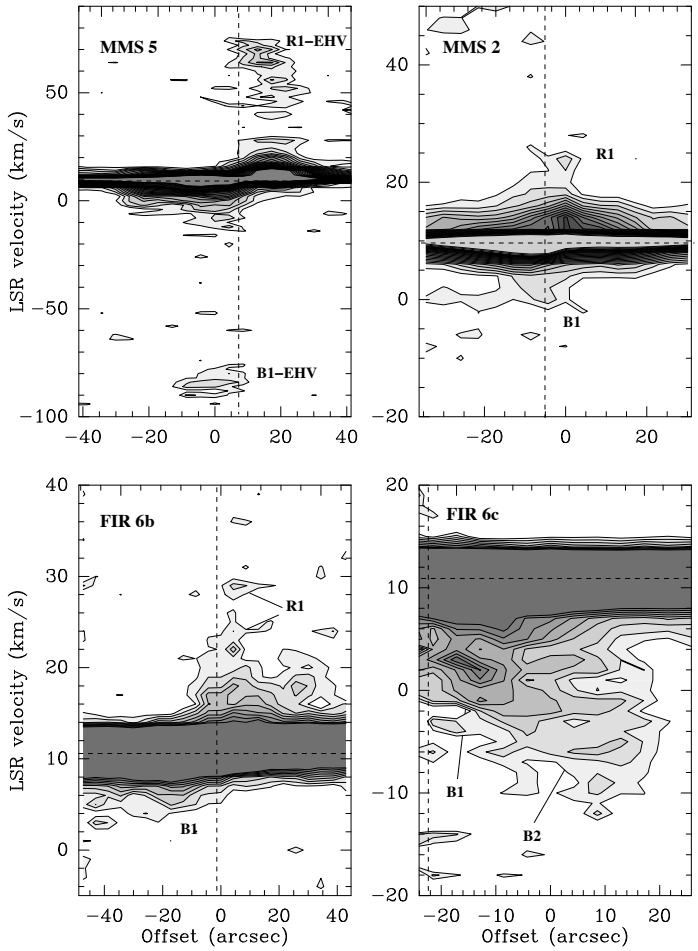

Figure 4.8: Position-velocity diagrams of the CO (6–5) emission along the outflow axes indicated in figures 4.1 and 4.3. The name of the central source is given at the at the upper left corner of each panel. The main outflow features are indicated with labels. Note that the reference offset position is the geometrical center of the PV cut, not the position of the central objects. The black dashed lines represent the systemic velocity (V_{LSR} =11 km s^{-1}) and the offset position of the central source.

4.7 Excitation and physical conditions

4.7.1 Population diagram

Under the assumption that the gas is in LTE and that the ^{12}CO emission is optically thin, we use the Boltzmann relation for the level populations to estimate the rotational temperature (T_{rot}) and the total column density (N) at selected positions within the outflow lobes: $\log(N_u/g_u)=\log(N/Q)-\log(e)/T_{rot}$. Here, N_u and g_u are the column density and statistical weight of the upper state level, respectively, N is the total column density, and Q is the partition function (e.g. Goldsmith & Langer, 1999). Under the adopted assumptions, N_u is related to the integrated intensity (W) by $N_u=8\pi k\nu_{ul}^2 W/hc^3 A_{ul}$, where k and h are Boltzmann and Planck constants, respectively, c the speed of light, ν_{ul} the rest frequency, and A_{ul} the Einstein coefficient (see Table 1). The partition function is approximated by $Q\sim T/(4.8\times10^{-2}B_e)$, where B_e (57.6 GHz for CO) is the rotational constant (e.g. Rohlfs & Wilson, 2004).

The selected outflow positions are FIR 6b-B1, FIR 6b-R1, FIR 6c-B1, FIR 6c-B2, MMS 5-B1, MMS 5-R1, MMS 2-B1, and MMS 2-R1 (see Fig. 4.1 and Fig. 4.3). In order to include in our analysis the CO (3–2) data taken with ASTE by T08, we have convolved our CO (6–5) and (7–6) observations to the angular resolution of the CO (3–2) observations (i.e. 26″). Table 4.4 shows the CO (3–2, 6–5, 7–6) integrated intensities convolved to 26″ resolution at the selected positions. We have only included the wing emission in our analysis, and in the case of the FIR 6 outflows where the high-velocity CO (7–6) emission was not detected we use the rms as an upper limit. We have also produced the rotational diagram for the EHV emission from the MMS 5 outflow. In Table 4.5 we show the results, T_{rot} and N_{total}, obtained from the rotational diagram analysis. In general, outflow positions within the OMC-2 FIR 6 region have lower rotational temperatures than positions within the OMC-3 MMS 1-6 outflows. As expected, the opposite tendency is seen for the total column density values, i.e. higher column densities in the OMC-2 FIR 6 outflows. In addition, when comparing the EHV with the wing emission, we found that T_{rot} is similar in both velocity ranges for MMS 5-R1, but a slightly higher T_{rot} is measured in the wing range than in the EHV range of MMS 5-B1. We note that this behavior is different from what we have found in L1448-mm (paper I), for which higher T_{rot} are found in the EHV range than in the wing range. However, we should consider that the EHV emission is not spatially resolved in our observations, so beam filling effects may play a role in the our results which have not accounted for this factor.

4.7.2 Large Velocity Gradient

Radiative transfer calculations with RADEX (van der Tak et al. 2007) were made in the Large Velocity Gradient (LVG) approximation and plane-parallel geometry.

Table 4.5: Rotational diagram results.

Position	T_{rot}(K)	N_T (10^{16} cm^{-2})
FIR 6b-B1	31±23%	1.6±2.4%
FIR 6b-R1	68±3%	1.1±0.1%
FIR 6c-B1	66±2%	1.2±0.1%
FIR 6c-B2	57±15%	1.7±0.9%
MMS 5-B1	82±14%	2.2±0.5%
MMS 5-B1(EHV)	46±25%	0.51±1.8%
MMS 5-R1	95±51%	0.43±1.8%
MMS 5-R1(EHV)	77±30%	0.46±1.3%
MMS 2-R1	68±2%	0.48±0.1%
MMS 2-B1	62±6%	0.83±0.3%

The molecular data was retrieved from LAMDA data base [2], which uses the energy levels, transition frequencies and Einstein A coefficients from CDMS and JPL data bases. The collisional rate coefficients are adopted from Yang et al. (2010) and include energy levels up to J=40 for temperatures ranging from 2K to 3000K.

As we have discussed in Paper I, one quantity that can be well constrained by CO line ratios is the thermal pressure, defined as $T_{kin} \times n$, since for a wide range of temperatures the line ratio curve in a thermal pressure vs. temperature plot stays constant. We have therefore performed LVG calculations with RADEX to reproduce the CO (3–2)/ CO (6–5) line ratio, at different positions within the outflow lobes. In our calculations we have used the column densities previously derived from the rotational diagrams (Table 4.5). The results at some selected positions are shown in Fig. 4.9 as thermal pressure vs. temperature curves. The observed (3–2)/(6–5) line ratios presented in Fig. 4.9 show a tendency of higher thermal pressure in the MMS 5 outflow than in the MMS 2 and FIR 6 outflows, which possibly means that the outflow from MMS 5 injects more energy into the surrounding gas (our outflow parameters estimates described in sect. 7 also support the idea). Unfortunately, we cannot provide an analysis of the thermal pressure as a function of distance from the exciting source, as we have done for the low-mass sources of Paper I, since usually a complete outflow lobe falls into the 26″ beam on which we make the (3–2)/(6–5) line ratio analysis. However, it is interesting to note that for MMS 5 a high kinetic temperature lower limit has been found. From Fig. 4.9 it can be seen that T_{kin} >200 K for the wing emission at MMS 5-R1, and T_{kin} >100 K for the EHV component at the same position. This result is consistent with the lower limits that have been reported for some low-mass class 0 outflows (e.g. Paper I). We can therefore conclude that the MMS 5 outflow shows excitation conditions similar to the low-mass class 0 outflows.

[2]http://www.strw.leidenuniv.nl/ moldata/

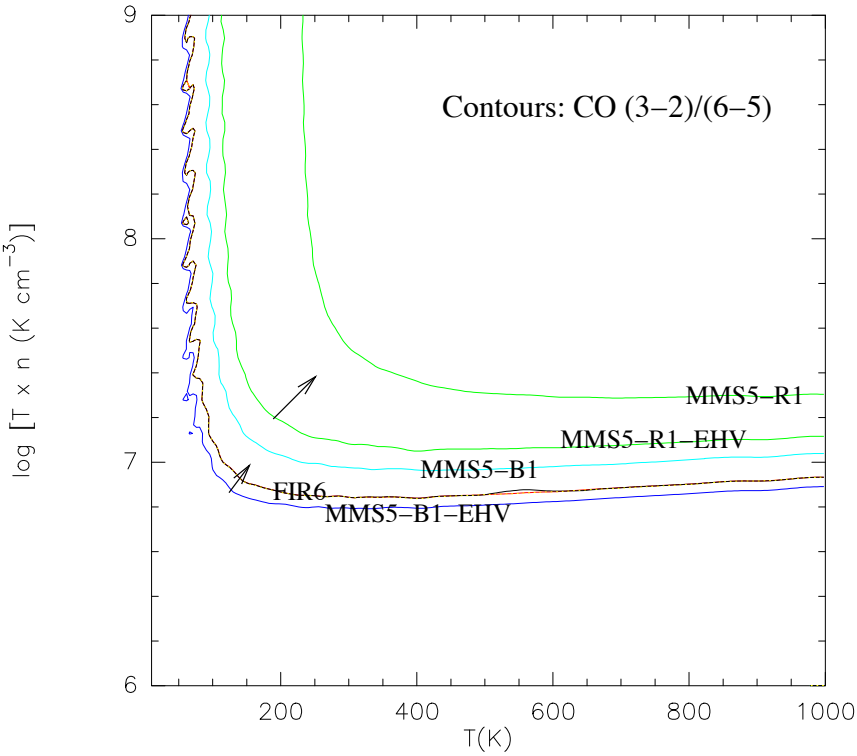

Figure 4.9: Thermal pressure (T_{kin} × n) vs. kinetic temperature plot from LVG calculations. The curves show the (3–2)/(6–5) observed ratios at different positions in FIR 6 and MMS 5 outflows. The positions are indicated by the labels on top of the curves. Note that the curves labeled MMS 5-R1-EHV and MMS 5-B1-EHV, and marked also with arrows, show the lower limits for the EHV range in the MMS 5 outflow. Note also that the curves for all FIR 6 outflow positions (FIR 6b-B1, FIR 6b-R1, FIR 6c-B1, FIR 6c-B2) overlap each other and are labeled simply FIR 6.

Table 4.6: Outflow properties derived from CO (6–5).

Velocity range	δv_{max} (km s^{-1})	R_{max} (10^{-2}) (pc)	t_d (10^3) (yr)	$M(H_2)$ (10^{-3}) ($M_\odot$)	F_m (10^{-5}) ($M_\odot$ km s^{-1} yr^{-1})	E_k (10^{43}) (erg)	L_{mec} ($L_\odot$)
				FIR 6b			
Blue	8	2.99	3.651	6.04	1.8	0.75	0.02
Red	19	4.36	2.246	2.89	3.4	2.0	0.07
Total				8.93	5.3	2.8	0.09
				FIR 6c			
Blue	26	3.59	1.349	5.02	13	6.6	0.39
				MMS 5			
Blue	106	6.38	0.588	9.09	230	200	27.50
Red	59	3.59	0.594	4.95	69	34	4.59
Total				14.04	300	230	32.09
				MMS 2			
Blue	23	3.49	1.485	1.00	2.1	1.0	0.06
Red	19	4.38	2.256	0.40	0.48	0.28	0.01
Total				1.40	2.6	1.3	0.07

4.8 Outflow Properties

Using the velocity integrated CO (6–5) maps of the outflow emission, we calculate the mass of the outflow gas. Assuming that the ^{12}CO is optically thin, the relation between the total column density (N) and the velocity integrated emission (W) is given by:

$$N = \frac{1.4 \times 10^{14}}{(J+1)\mu^2 B_e} \frac{e^{(4.8\times10^{-2} B_e J(J+1)/T_{ex})}}{1 - e^{(-4.8\times10^{-2}\times 2B_e(J+1)/T_{ex})}} \times W, \tag{4.1}$$

which, for the CO (6–5) line becomes:

$$N(CO) = 3.92 \times 10^4 \frac{e^{82.94/T_{ex}}}{1 - e^{-33.18/T_{ex}}} \times W. \tag{4.2}$$

We use the standard ISM value for the relative ^{12}CO abundance, X(H_2/CO) $\sim 10^4$, to obtain the H_2 column density and finally calculate the H_2 mass,

$$M = 2 \times m_H \times X(H_2/CO) \times \Omega \times N \times D^2. \tag{4.3}$$

In the latter, m_H is the hydrogen mass, Ω the solid angle of the lobe, and D the distance to the source. We measure ΩN by summing up the contribution of each pixel with a S/N ratio above 3. In the calculation we use for T_{ex} the values of T_{rot} obtained from the rotational diagram analysis (Table 4.5). First, we calculate the mass detection limit of our CO (6–5) observations. For this, we assume a typical T_{ex} of 50 K, and the rms at 1 km s^{-1}. We calculate a mass detection limit of 1.3×10^{-5} $M_\odot$ within one beam. For the detected outflows, the calculated masses are 1.4×10^{-2}

$M_\odot$ and 1.4×10^{-3} $M_\odot$, for the MMS 5 and MMS 2 outflows, respectively; while we find 8.9×10^{-3} $M_\odot$ and 5.0×10^{-3} $M_\odot$ for FIR 6b and FIR6 c(blue-lobe), respectively (see Table 4.6 for a summary). In order to compare our mass estimates to those calculated by T08, we re-compute the outflow mass using the same T_{ex} assumed by these authors, i.e. 30 K for all outflows. In this case, the total masses are 4.0×10^{-2} $M_\odot$ and 3.7×10^{-2} $M_\odot$, for MMS 5 and MMS 2 respectively, while it is 1.4×10^{-2} $M_\odot$ and 1.3×10^{-2} $M_\odot$ for FIR 6b and FIR6 c(blue-lobe), respectively. We note that our mass estimates based on the CO (6–5) emission are consistent within a factor of 4 with those reported by T08 for MMS 5, MMS 2, and FIR 6c (blue-lobe), while it differs by a factor of 9 for FIR 6b outflow. The high discrepancy between the mass estimate from CO (3–2) and CO (6–5) in FIR 6b outflow may be related to the fact that, as we have found in the previous analysis, this shows lower excitation conditions than the other outflows we have studied. Therefore, due to the lower excitation, we have more high-velocity gas excited in the CO (3–2) transition than in the CO (6–5). We also note that our mass estimates from CO (6–5) in OMC-2/3 outflows are similar or lower than those obtained from the CO (3–2) line in the Perseus region outflows reported by Curtis et al. (2010). The average outflow masses in Perseus are 0.09 $M_\odot$ for Class 0 objects and 0.06 for Class I objects (Curtis et al. 2010). Note that the outflow masses in Class 0/I objects in this Perseus survey are not statistically different (Curtis et al. 2010). Therefore for a Class 0 type object such as MMS 5, the outflow mass determined from CO (6–5) is similar to the outflow mass measured from CO (3–2) in Class 0/I low-mass objects. On the other hand, our mass estimates for Class I type objects are lower up to a factor of 10 with respect to the value reported in low-mass outflows. The later may be also an effect of the low excitation of class I type outflows.

We also determine other parameters such as dynamical time scale (t_d), mass outflow rate ($\dot{M}$), mechanical force (F_m), kinetic energy (E_k), and mechanical luminosity (L_{mech}). These quantities are defined as follows: t_d=R/V, $\dot{M}$=M/t_d, P=M$\times\delta v_{max}$, F_m=M$\times$V/t_d, E_k=M$\times\delta v_{max}^2/2$, L_{mech}=E_k/t_d (e.g. Beuther et al. 2002a). In the above expressions, R=R_{max}/sin i and V=δv_{max}/cos i, where R_{max} and δv_{max} are the maximum extension and maximum relative velocity of the lobes, and i the angle of the lobe with respect to the plane of the sky. Following T08, and in order to compare with their results, we assume i = 45 degrees for all outflows, although it may not be the real inclination angle for some of them. In Table 4.6 we show the summary of our results. It is important to point out that considering uncertainties such as data calibration, definition of the velocity boundary limits for the integrated emission, opacity corrections, and others, mass determinations are usually accurate within a factor 2-3, while kinematic parameters should be approximately correct within a factor 10-30 (see, e.g., discussion in Cabrit & Bertout 1990).

Within the uncertainties mentioned above, we note that the outflows properties we have determined for our set of intermediate-mass outflows are similar to the values found by other authors in class 0/I low-mass outflows (e.g., Paper I; Curtis et al. 2010). In particular, F_m and E_k values for the intermediate-mass class 0 outflow MMS 5 (3.0×10^{-3} $M_\odot$ km s^{-1} yr^{-1} and 2.3×10^{45} erg, respectively) are

similar to those we have reported in Paper I for the low-mass class 0 outflow L1448-mm (7.8×10^{-4} $M_\odot$ km s^{-1} yr^{-1} and 1.5×10^{45} erg, respectively). In fact, due to the larger velocity range in which we see the outflow emission from MMS 5 outflow compared to L1448-mm outflow, the mechanical luminosity of the former seems to be larger by a factor of $\sim$7 with respect to the latter. We therefore conclude that the EHV outflow in the intermediate-mass outflow MMS 5 is at least as energetic as its low-mass counterpart L1448-mm.

4.9 Discussion

4.9.1 Comparison with Near Infrared (NIR) H_2 observations

The molecular hydrogen v=1-0 S(1) line at 2.12 μm has proven to be an important shock tracer in molecular outflows (for a review see Eisloffel et al. 2000). A large number of observations have shown that this line is a useful tool to search for outflows in YSO's and indeed to search for YSO's themselves (e.g., **?**Stanke et al. 2002; **?**). Recently, Stanke et al. (2002) have presented a survey of the whole Orion star forming region in the H_2 2.12 μm line. These authors have identified a total of 76 candidate flows in the cloud. T08 have also presented NIR observations of the J(1.25μm), H(1.63μm), and K_s(2.14μm) bands (the later including the 2.12 μm line) in the OMC-2/3 region. We use the observations from T08 to compare our CO observations with possible outflows traced in H_2. For details of the NIR observations see T08.

In Fig. 4.10 we show a composite image with our mid$-J$ CO observations (contours) overlaid on the 3 color NIR (J, H, K_s) image. Figure 4.10 shows the individual outflows that we have reported in previous sections. At least some part of the outflow structures in MMS 2, MMS 5, and FIR 6b outflows are clearly associated with NIR structures; while this seems not be the case for FIR 6c outflow, whose blue lobe is mostly in a region apparently without NIR emission (at the limit of the observations).

The outflow from MMS 5 source is the clearest case of an association between NIR emission and a CO outflow structure. For MMS 5 in Fig 4.10 we show the CO (7–6) high-velocity emission (cyan and magenta contours) together with the CO (6–5) EHV emission (blue and red contours). The main NIR structure in this region has a monopolar morphology that coincides with the CO (6–5) EHV blue-shifted lobe. To the west of this monopolar structure, at least three NIR knots can be seen. These three NIR knots are seen superimposed on the CO (7–6) blue-shifted lobe, with the westernmost one coincident with the westernmost CO (7–6) high-velocity emission peak. On the other hand, no NIR structure is coincident with the red-shifted CO lobe, neither high-velocity CO (7–6) nor EHV CO (6–5). Due to the positional coincidence and the velocity distribution suggested by the CO observations, it is likely that the monopolar structure and the knots are part of the same outflow.

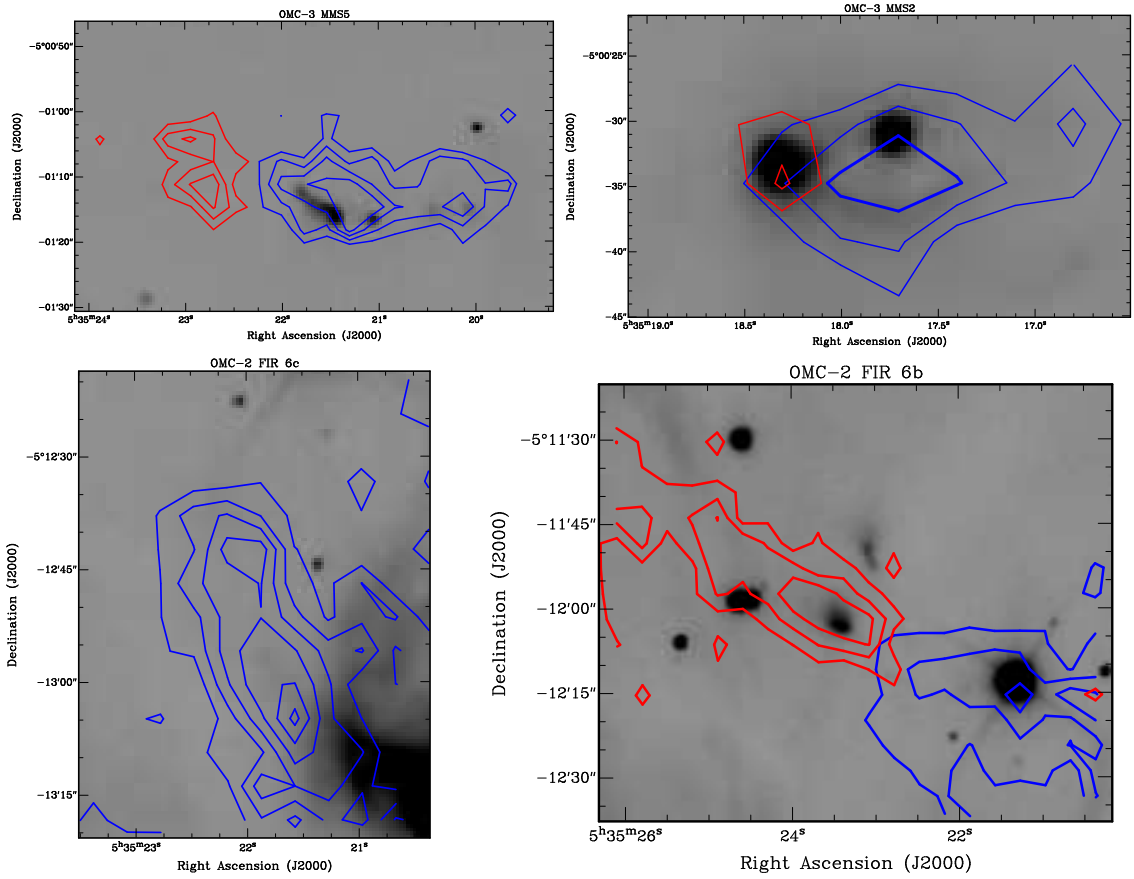

Figure 4.10: Composite image showing the outflows from OMC-2 FIR 6 and OMC-3 MMS 1-6 regions overlaid on the K-band (2.12μm) emission (grey scale) from T08. Each image is labeled with its corresponding object. Except for OMC-2 MMS 5, blue and red contours show the blue- and -red-shifted CO (6–5) high-velocity emission that have been presented in previous figures. In the case of OMC-2 MMS 5, blue- and red-shifted contours show the CO (7–6) high-velocity emission.

Since the knots are not well aligned with the monopolar structure, it is likely that the MMS 5 outflow is precessing. The NIR observations have proven the jet nature of the EHV emission in MMS 5 outflow, since the EHV blue-shifted lobe is mostly coincident with the monopolar NIR structure, which also show a high collimation typical of jets.

FIR 6b and MMS 2 are the other two outflows that show a positional coincidence with NIR structures. In Fig. 4.10, it is seen that the inner part of the red-lobe of FIR 6b outflow is coincident with a NIR compact source. In addition, a diffuse weak NIR emission can be barely seen extending along the outflow direction. It is possible that the compact plus the diffuse NIR emission are tracing the central source plus the outflow cavity, as observed in other YSOs, but deeper NIR observations are needed to probe this possibility. In the case of the MMS 2 outflow, its red lobe seems to be coincident with a NIR structure, but it is not clear whether the NIR emission is related to the outflow or to the central source. Therefore, in FIR 6b and MMS 2 outflows we can not confirm a relation between the NIR emission and the CO outflow emission.

4.9.2 CO (6–5) as a tracer of young and excited jets/outflows

From the observational point of view, a clear advantage of SiO observations compared with the traditional low$-J$ CO observations in protostellar outflows is that the SiO emission is in most cases an exclusive tracer of jets and shocks, while the low$-J$ CO is usually contaminated by the low-velocity emission from the ambient core. This is a critical issue in particularly for jets/outflows whose axis are close to the plane of the sky, which may be completely missed for low$-J$ CO observations. Another important characteristic is that at sub-millimeter transitions the SiO traces relatively dense and/or warm gas that has been suggested to be related with the primary jet (Palau et al. 2006). However, in Paper I we have shown that indeed sub-millimeter CO observations, in particular the CO (6–5) emission, can also trace dense and/or warm gas in the jet component of class 0 protostellar outflows. In addition, we found that even at velocities close to the ambient cloud it is still possible to distinguish outflow structures.

The observations presented in this paper may also add yet another important characteristic of the CO (6–5) emission in protostellar outflows, which is the identification of highly excited outflows when mapping large areas in molecular clouds. Here we have shown that highly excited outflows are better traced by CO (6–5) and (7–6) than with the CO (3–2) transition. In fact our observations revealed the EHV emission from a class 0 outflow that was not detected in sensitive CO (3–2) observations.

The results of our LVG analysis have shown that the high-velocity emission in the class 0 intermediate-mass source shows physical conditions that are similar to what we have found in our previous study of class 0 low-mass protostars (i.e. T_{kin} >200 K and n $\sim$10^5–10^6 cm^{-3}). The discovery of extremely high-velocity gas towards the class 0 intermediate-mass outflow related to MMS 5 gives also evidence of a

kinematics similar to class 0 low-mass outflows.

Since high excitation gas is usually observed during the early phases of protostellar outflows (Nisini et al. 2007), the CO (6–5) transition may be among the best tracers of the earliest phases of the outflow evolution. Our observations may support this view, since within the mapped regions we have covered class I and class 0 type intermediate-mass YSO's, and we have found that the CO (6–5) and (7–6) emission is strongest towards outflows from class 0 sources (e.g. MMS 5). However, observations of a statistical significant sample are needed to confirm this suggestion.

4.10 Summary and conclusions

In the following we summarize the main results from this study:

- The CO (6–5)/(7–6) emission in OMC-2 FIR 6 and OMC-3 MMS 1-6 was found tracing outflows related to class 0 intermediate-mass objects within those regions.
- Extremely High Velocity CO (6–5) emission was detected from the MMS 5 outflow in the OMC-3 region. The CO (7–6) transitions was detected at the 3σ level from the red lobe of the same outflow.
- By a comparison with previous observations, it has been found that the CO (6–5) and (7–6) emission is stronger towards the location of the central objects than the low-J CO (3–2) emission.
- Using LVG calculations we found that the densities and kinetic temperatures of the high-velocity gas are, respectively, $n > 5\times10^5$ cm^{-3} and $T_{kin} > 200$ K.
- In the detected outflows, even at around the cloud velocity the outflow structures are clearly seen, in contrast with low−J CO observations in which the low-velocity gas from the outflow is hidden by the emission from the cloud.
- The kinematics and physical conditions of MMS 5 outflow suggest that it is the counterpart of the young class 0 low-mass outflows (e.g. L1448), and therefore that young intermediate-mass outflows are as energetic as their low-mass counterparts.

Chapter 5

Warm gas in protostellar outflows III. High-mass objects from ATLASGAL

5.1 Introduction

Understanding the formation of high-mass stars is one of the main problems of modern astrophysics. Accretion and outflow are the two related processes that characterize star-formation. Both phenomena have been widely confirmed in low-mass protostars. However, although outflows in massive regions have been widely studied, the presence of an accretion disk is still under debate (e.g. Cesaroni et al. 2007). That has lead to a controversy on whether high-mass stars form via the collapse-accretion/outflow process or by competitive accretion including possibly stellar mergers in dense clusters (Bonnell & Bate 2005; Zinnecker & Yorke 2007). Given the typical distances of massive regions (several kpc), and since high mass protostars usually form in clusters, the direct observation of massive disks is currently very challenging. Only a few cases are known to provide some evidence of the presence of disks in massive star formation, although whether they are the definite prove is still under debate (Cesaroni et al. 2007). In this regard, new techniques/facilities are the promise to truly give strong evidence on their existence. Examples are the recent near-IR interferometric observations by (Kraus et al. 2010) and in the near future millimiter/submillimeter observations with ALMA. On the other hand, bipolar molecular outflows extend to larger distances from the protostar than the disk systems, and they are therefore another tool to prove the accretion/outflow process in the formation of high-mass stars and investigate their properties.

Outflows with high velocities and collimation are a common characteristic of early low-mass protostars. Within the last decade high-velocity outflows have been observed towards high-mass protostars as well, and in some cases showing collimated structures similar to the low-mass case (Beuther et al. 2004), pointing to a common formation mechanism in both mass regimes. Indeed, observations have also suggested an evolutionary scheme in which massive outflows are collimated in

early phases and de-collimate as the protostar evolves (Beuther 2005), as it is also known to occur in low-mass outflows (Bachiller 1996). Although observations have covered a significant number of massive objects (Zhang et al. 2001, 2005; Beuther et al. 2002b), only few early B type sources have been studied. Recently, early O type stars have started to be covered by single-dish studies (López-Sepulcre et al. 2009).

In recent years, unbiased surveys in the Mid-IR and sub-mm have given us new samples of candidates of high-mass protostars in the earliest phases of formation. Systematic studies trying to characterize such objects are underway. Examples of these surveys are the MSX (Price et al. 2001) and GLIMPSE (Benjamin et al. 2003) surveys in the Mid-IR, ATLASGAL (Schuller et al. 2009) and HiGAL (Molinari et al. 2010) in the sub-mm. Moreover, follow-up observations of these surveys have started (e.g. RMS survey: Urquhart et al. 2007).

ATLASGAL is the APEX telescope large area survey of the galaxy at 870 μm. Initial results have revealed thousand of compact sources with no bright IR counterparts, some of them likely corresponding to precursors of high-mass protostars or proto-clusters (Schuller et al. 2009). An ATLASGAL sample was recently studied by Wyrowski et al. (in prep) with the Mopra telescope at 3mm. Among others, the SiO molecule, one of the best shock/outflow tracers (Gusdorf et al. 2008b), was observed.

The GLIMPSE survey with IRAC/Spitzer has also revealed outflow activity. The emission excess of the 4.5 μm channel with respect to the 3.6 and 8.0 μm channels is interpreted as a shock tracer, due to the presence of ro-vib H_2 lines within this channel. Extended green emission (4.5 μm coded as green), the so called *green fuzzies*, has been suggested to trace massive outflows (Smith et al. 2006). A catalog of such objects in the GLIMPSE survey has been made by Cyganowski et al. (2008, hereafter C08). Interestingly, the most prominent ATLASGAL-Mopra SiO sources are not so prominent *green fuzzies*. The best example is NGC 6334 I(N), one of the two strongest SiO sources. Arc-sec resolution observations by Brogan et al. (2009) show a compact bipolar SiO outflow, but no prominent *green fuzzy* (indeed not in the C08 catalog). That might suggest the presence of a compact early outflow revealed by SiO but hidden to H_2 due to the high mid-IR opacity of the embedded objects.

The current knowledge of the physical properties of massive outflows comes mainly from CO observations in low$-J$ transitions (Zhang et al. 2005; Beuther et al. 2002b). However, as we have seen in this thesis, mid$-J$ CO observations are revealing interesting properties in low- and intermediate-mass outflows that are desirable to test in massive regions as well. With the aim of studying the warm gas in massive protostars mid$-J$ CO observations have been carried out towards a sample of 4 prominent SiO sources observed in the follow-up studies of the ATLASGAL survey. We complement these observations with archival data from the GLIMPSE survey, since most of these sources were not reported as *green fuzzies* by Cyganowski et al. (2008). In addition, for one source we obtained interferometric CO (2–1) and SiO (5–4) observations with the SMA.

5.2 The sample

The sources under study were selected based on the SiO (2–1) emission observed with the Mopra telescope by Wyrowski et al. (in prep). The selection method consisted in choosing the most prominent sources in terms of integrated intensity and high-velocity wings. Due to time constrains, only four sources were possible to observe. These are among the 10 strongest sources in SiO (2–1) emission. The four sources and their properties are shown in Table 5.1. In the following a summary of the information available for the sources is given.

G328.81+0.63. This region is known to have a cometary HII region seen at centimeter wavelength (Ellingsen et al. 2005), which present a counterpart in the mid-infrared (De Buizer 2003). In addition, a more compact HII region is located to the northeast of the cometary HII region, but has no associated mid-infrared emission. Nine linearly distributed methanol masers lie between these two centimeter continuum sources, and at the edge of the emission from the brightest mid-infrared source.

G340.97−1.02. Few information is available for this source. Cyganowski et al. (2008) listed it as a *green fuzzy* and Peretto & Fuller (2009) cataloged this source as a Spitzer infrared dark cloud.

G351.16+0.69. This is a relatively well studied source, specially at infrared and centimeter wavelengths. It is related to the infrared source NGC 6334 V (McBreen et al. 1979; Kraemer et al. 1999), at a distance of ∼1.7 kpc (Neckel 1978). The total luminosity range from 6.5×10^4 $L_\odot$ to 1.9×10^5 $L_\odot$ (Harvey & Gatley 1983; Loughran et al. 1986). A bipolar reflexion nebula has been revealed in infrared emission, which is likely related to a bipolar outflow driven by an unidentified, possibly massive, protostar (e.g. Chrysostomou et al. 1994; Simpson et al. 2009). Evidence for an unidentified massive protostar in the region includes photodissociated-region emission (e.g. Burton et al. 2000).

G353.41−0.36. Radio emission from this source has been found arising from two components: an extended H II region with a shell-like morphology (labeled B), and a bright compact source (labeled A), with an angular size of ∼1.5″, located near the western edge of the extended structure (Garay et al. 2006). At 1.4 GHz the emission arises mainly from the shell component, which is associated with an IRAS source (IRAS 17271-3439). At higher frequencies (i.e. 8 GHz) the emission is dominated by the compact source (Garay et al. 2006). As derived from the radio continuum and far-IR observations, component A correspond to spectral type O9.5 - 05.5, and luminosity in the range of 3.7×10^4 $L_\odot$ to 3.7×10^5 $L_\odot$.

5.3 Observations

5.3.1 APEX observations

Mid−J CO observations towards four ATLASGAL sources were performed with the MPIfR PI instrument CHAMP+ (Kasemann et al. 2006) on the APEX telescope

Table 5.1: Source properties.

Source	870μm peak (Jy beam^{-1})	870μm Flux (Jy)	Dist. (kpc)	T_k[a] (K)	Mass[b] (10^3 $M_\odot$)	Luminosity[c] (10^4 $L_\odot$)	Ref.
G328.81+0.63	22.8	65.0	3.0	24	2.5	4.0-21.5	1,2
G340.97−1.02	10.6	27.7	2.3	36	0.4	-	3,4
G351.16+0.69	22.0	124.9	1.7	37	0.9	6.5-19.0	5,6
G353.41−0.36	21.7	142.8	3.1	16	1.1	3.7-37.5	7

(1) Ellingsen et al. (2005), (2) De Buizer (2003), (3) Cyganowski et al. (2008)
(4) Peretto & Fuller (2009), (5) Kraemer et al. (1999), (6) Neckel (1978)
(7) Garay et al. (2006). [a]Kinetic temperatures from NH_3 observations (Wienen et al. in prep).
[b] From 870μm Flux, assuming optically thin emission and using T_k from NH_3.
[c] Taken from the literature.

Table 5.2: Source information and map rms.

Source	α(J2000) (h m s)	δ(J2000) (° ′ ″)	V_{LSR} (km s^{-1})^2	^{12}CO rms (K)[1] (6–5)	(7–6)
G328.81+0.63	15:55:48.56	−52:43:08.4	−52.0	0.38	0.63
G340.97−1.02	16:54:57.30	−45:09:04.0	−25.0	0.38	0.57
G351.16+0.69	17:19:57.70	−35:57:50.0	−8.0	0.43	0.58
G353.41−0.36	17:30:26.86	−34:41:50.5	−17.0	0.44	0.79

(Güsten et al. 2006) during July 2010. Details of the array have been given in previous chapters. In our observations the front-end was connected to a Fast Fourier Transform Spectrometer (FFTS, Klein et al. 2006).

The CO (6–5) and (7–6) lines were mapped simultaneously with CHAMP+ in the On-The-Fly (OTF) mode, with an ON time of 1.0 seconds per position, and steps of 3″. For all sources a map of size 60″×60″ was centered at the position of the ATLASGAL continuum peak. The backend was set to provide a total bandwidth of 2.8 GHz (for each pixel, for CHAMP+). The final spectra were re-sampled to 1.0 km s^{-1} spectral resolution for all transitions in both sources.

The precipitable water vapor (PWV) during the CHAMP+ observations was in the range of 0.5 to 0.6 mm. The pointing was determined by continuum cross-scan observations on NGC 6334-I. Pointing corrections were always within 3″. The focus was checked on Jupiter. The calibration was done by observing hot and cold loads. The data reduction was done in the same way as the CHAMP+ observations presented in previous chapters, using the GILDAS package.

The images and spectra are presented in main beam brightness temperature scale, for which we have used a forward efficiency (F_{eff}) of 0.95 (for both receivers) and a beam coupling efficiency (η_s) measured on Jupiter, appropriate for the spatial scales of the observed outflows. The measured η_s was 0.48 for both LFA and HFA of the CHAMP+ array. The source coordinates and rms noise levels are summarized in Table 5.2.

5.3.2 SMA observations

Simultaneous SiO (5–4) and CO (2–1) observations were carried out on 2011 May 11 with the SMA on Mauna Kea, Hawaii (Ho et al. 2004). We used the compact array configuration that provides baselines ranging from 16.4 m to 77.0 m. The primary-beam size (HPBW) of the 6 m diameter antennas at 217 GHz (i.e. the rest frequency of the SiO (5–4) transition) is $\sim$54″. The spectral correlator covers 4 GHz bandwidth in each of the two sidebands. The frequency coverage was from 216.7 to 220.7 GHz in the lower sideband (LSB) and from 228.7 to 232.7 GHz in the upper sideband (USB). Each band is divided into 48 "chunks" of 104 MHz width. We used a uniform spectral resolution of 406.25 kHz across an entire 4 GHz band. The corresponding velocity resolution was 0.561 km s^{-1}. The visibility data were calibrated using the MIR software package, which was originally developed for the Owens Valley Radio Observatory (Scoville et al. 1993) and adapted for the SMA [3]. The absolute flux density scale was determined from observations of Neptune. A pair of nearby compact radio sources, 1626-298 and 1802-396, were used to calibrate the relative amplitude and phase. We used 3C279 to calibrate the bandpass.

The calibrated visibility data were imaged using MIRIAD. We used natural weighting that provided a synthesized beam of 3.4″×2.3″ with a position angle of 63°. The rms noise level of the line data was 88.5 mJy beam^{-1} at 1 km s^{-1} spectral resolution. The continuum map was obtained by averaging the line-free chunks of the both sidebands. To improve the signal-to-noise ratio, the upper and lower sidebands were combined after the consistency of the images of two sidebands was confirmed. With natural weighting, the synthesized beam size was 3.4″× 2.2″ with a position angle of 63°. The rms noise level of the 1.4 mm continuum map was 16.1 mJy beam^{-1}.

5.3.3 *Spitzer* IRAC data

Images of all four IRAC bands (3.6μm, 4.5μm, 5.8μm, 8.0μm), obtained in the framework of the GLIMPSE survey, were retrieved from the NASA/IPAC Infrared science data archive. We have used the post-basic calibrated data (BCD) images for our study. The mean FWHM of the point respond functions are 1.66″, 1.72″, 1.88″, and 1.98″ for bands 1, 2, 3 and 4, respectively.

5.4 Results

5.4.1 IRAC images

Figure 5.1 shows the three color images (blue: 3.6μm, green: 4.5μm, red: 8.0μm) from GLIMPSE for each of the four massive sources. G351.16+0.69 is the only one case in which the IRAC maps have been already published (Simpson et al. 2009). Except possibly for G353.41−0.36, outflow morphologies can be inferred

[3] http://cfa-www.harvard.edu/ cqi/mircook.html

from the IRAC 3 color images. The *green excess* is more remarkable in G340.97−1.02 and G351.16+0.69, and is less evident in G328.81+0.63 and G353.41−0.36. In the following we describe each case:
G328.81+0.63. The mid-IR emission shows mainly a monopolar structure in a north-south direction, with the southern lobe showing most of the emission. This lobe shows no evident *green excess*, and the 870μm emission from ATLASGAL seems to be centered at the base of the lobe.
G340.97−1.02. The mid-IR emission in this source shows a more complicated structure, with possible multiple outflow lobes. A main structure with a clear *green excess* is located in the middle of a region that is infrared dark at 8μm. The 870μm emission seems to be centered at this main structure.
G351.16+0.69. This source shows a clear (partially) bipolar structure with the emission showing a *green excess*, orientated in a east-west direction. This structure is located inside a region that is dark at 8μm. The 870μm emission seems to be centered at the bipolar structure, but it also shows extended emission to the west and north-west, following the infrared dark region. Among the sources presented here, G351.16+0.69 shows the most peculiar features in the mid-IR. In particular, the 4.5μm image very clearly shows a bow shock structure in the west lobe (see Fig. 5.2). Additionally, a collimated structure is seen in the 8μm channel, but pointing towards a direction different to the 4.5μm bow-shock (see Fig. 5.2). The latter may indicate that either the east-west outflow is precessing or the collimated 8μm structure is tracing an outflow different to the one that has produced the 4.5μm bow-shock.
G353.41−0.36. The mid-IR emission in this region is the most complicated to interpret, among the sources under study. No evident outflow morphologies can be identified, although *green excess* is barely suggested close to the center of the field, but in very localized regions. The 870μm emission is centered in a region that is infrared dark.

5.4.2 Mid−J CO emission

The average CO (6–5) and (7–6) spectra for each source are shown in Fig. 5.3. The mid−J CO emission has been detected up to high velocities in both transitions, although slightly weaker in the CO (7–6). The CO (6–5) maps of the outflow emission is presented in Fig. 5.4, overlaid on the 3 color images from GLIMPSE. To define the outflow's velocity range we have proceeded as in previous chapters, by looking for outflow morphologies in the channel maps and for line wings in the spectra (see sect. 4.4). In Fig. 5.4, blue and red contours show the blue- and red-shifted emission with respect to the LSR velocities shown in Table 5.2. The velocity ranges of integration are indicated in 5.4. In the case of G351.16+0.69, we have used a high- and intermediate-velocity range, since each of the two may trace different structures, as will be discussed below. In general, the blue- and red-shifted emission traces structures that are difficult to relate with a single outflow, since in each region we see multiple blue- and red-shifted lobes. In the following we describe

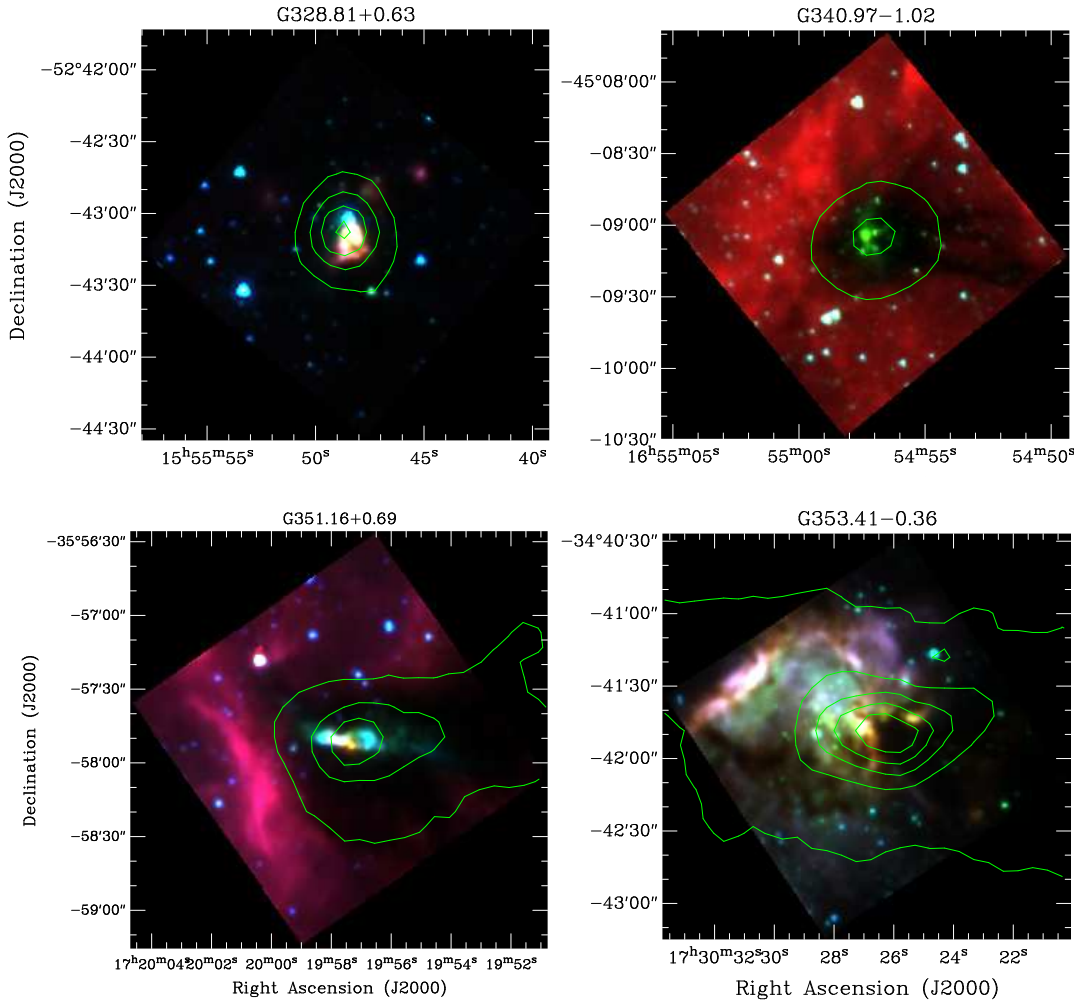

Figure 5.1: IRAC 3 color images from the GLIMPSE survey with overlays of the 870 μm emission (green contours) from the ATLASGAL survey. Contour spacing is 10% of the peak intensity, with the maximum contour at 90% of the peak (see Table 5.1 for the peak intensity of each source).

each case:

G328.81+0.63. The blue- and red-shifted CO (6–5) emission shows several peaks in this region. At least three peaks are found in the blue-shifted emission, while at least two peaks are clearly seen in the red-shifted emission. From the morphologies it is not straightforward to distinguish outflow structures as clearly as in low-mass outflows. However, due to the distribution of the emission, it is likely that we have more than one outflow in the region. Clearly, higher angular resolution observations are needed to distinguish the different outflow members.

G340.97−1.02. At least three peaks are found in the CO outflow emission from this source. In particular a prominent red-shifted structure extending in a north-south direction resemble quiet well the usual morphology of an outflow lobe. Al-

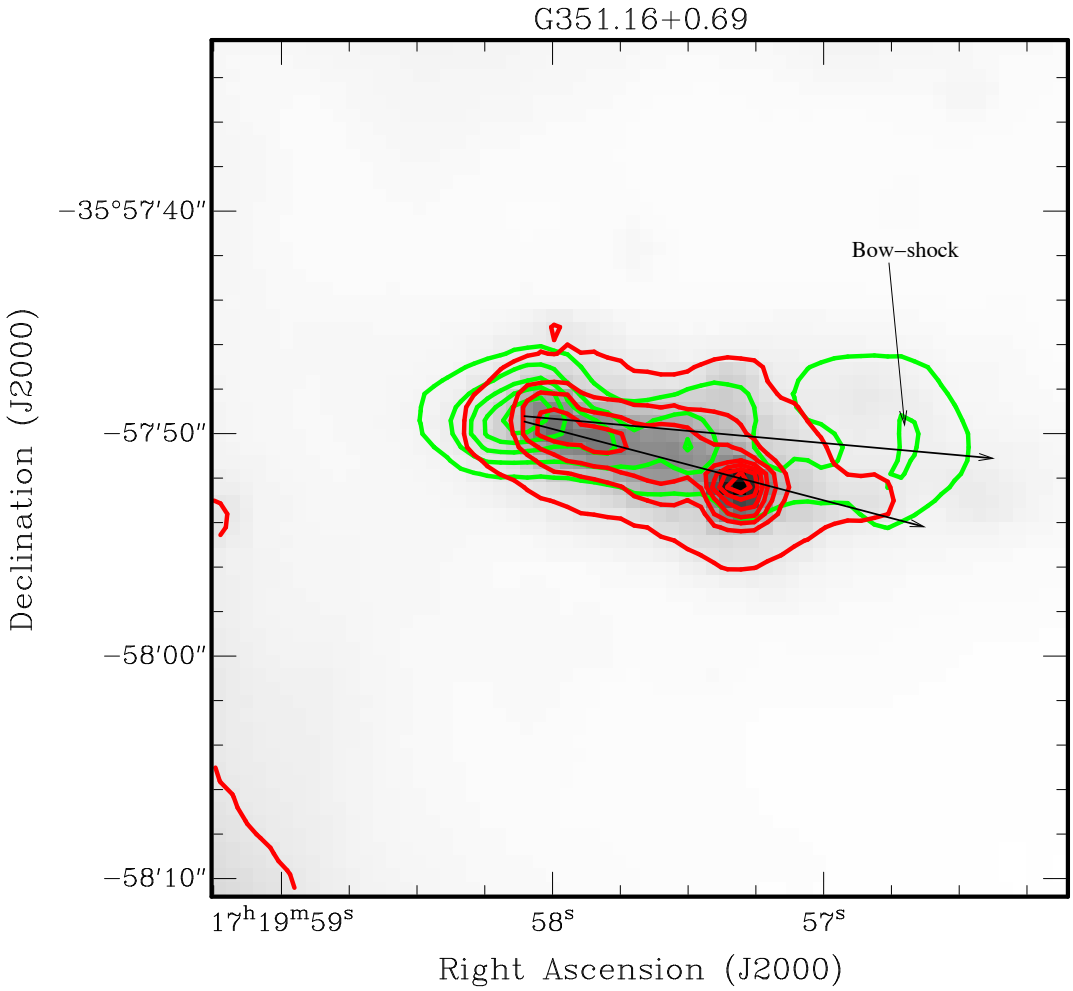

Figure 5.2: The 4.5 μm (green contours) and 8.0μm emission (grey scale and red contours) in G351.16+0.69. Contour spacing and first contour is 10% of the flux peak (2135 and 4653 MJy sr^{-1}, for 4.5 μm and 8.0 μm, respectively). Arrows show the axes of the two possible ejection events. Also indicated by an arrow is the bow-shock structure.

though the blue-shifted peak is offset from the direction of the previously mentioned red lobe, the extended blue-shifted emission may be tracing the counter-lobe of such system. However, since a second red-shifted peak appears perpendicular to the direction of the main red lobe, it is possible that a second outflow is present in the region.

G351.16+0.69. In this source we have found that the high- and intermediate-velocity CO emission are tracing different structures. The intermediate-velocity range trace a clear bipolar structure in the east-west direction. On the other hand, the high-velocity red-shifted emission appears offset from the axis of the the east-west outflow. However, from these observations it is not clear whether the the high-velocity blue-shifted emission traces a different lobe than the one revealed by

Table 5.3: Velocity range and map's rms.

	velocity range (km s^{-1})	rms (K)
	G328.81+0.63	
blue	-80 to -48	2.64
red	-36 to -16	1.39
	G340.97−1.02	
blue	-60 to -40	2.06
red	-15 to +10	1.30
	G351.16+0.69	
HV-blue	-50 to -30	
HV-red	+15 to +25	
inter-blue	-14 to -12	0.811
inter-red	-10 to -7	4.90
	G353.41−0.36	
blue	-70 to -25	2.21
red	-8 to +30	2.06

the intermediate-velocity emission. Evidence for such additional outflow traced by the high-velocity CO emission is presented in the next section, by means of higher angular resolution SMA observations.

G353.41−0.36. In the western part if this region blue- and red-shifted emission clearly trace a north-south outflow whose center coincide with the ATLASGAL continuum peak. To the east, additional blue- and red-shifted structures may be tracing at least one more outflow in the region.

5.4.3 Interferometric maps of G351.16+0.16

The continuum millimeter emission from G351.16+0.69 is displayed in Fig 5.5 on the 3 color GLIMPSE image. The 1.4 millimeter continuum shows at least two peaks that are separated by a few arc-sec. In addition, extended emission is seen mainly toward the north of the continuum peaks. However, the extended emission to the north-west revealed by the 870μm emission is not seen in the 1.4 mm continuum image. In Table 5.4 the results of Gaussian fits to the two peaks, component 1 and 2, are presented.

The Fig. 5.6 shows the CO (2–1) spectrum averaged over the region observed with the SMA. The CO (2–1) emission was detected from $\sim$−65 to 27 km s^{-1}, which therefore reaches higher velocities with respect to the CO (6–5) emission (see in particular the difference in the line profiles shown in Fig. 5.3 and 5.6). Figure 5.7 shows the CO (2–1) emission integrated over the high-velocity wings (indicated by dashed lines in Fig. 5.6), overlaid on the 3 color GLIMPSE image. The red- and blue-shifted wings are orientated in a north-south direction, with the outflow center closer to continuum component 2 than to component 1. However, no emission at intermediate velocities was found showing the east-west outflow found in the CO (6–

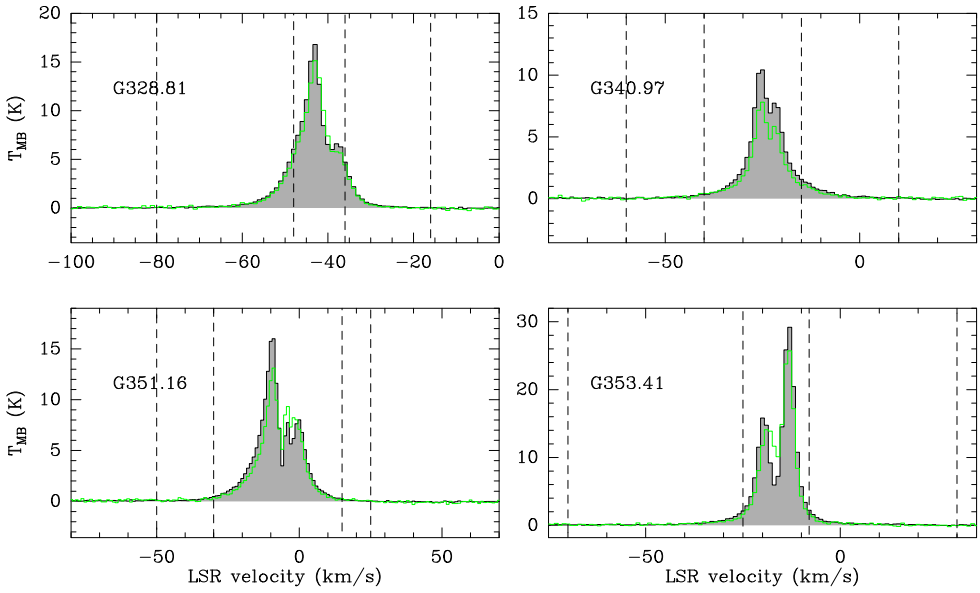

Figure 5.3: The average CO (6–5) and (7–6) spectra (black/grey and green, respectively) toward ATLASGAL sources. Vertical lines show the v_{min} and v_{max} that define the high-velocity outflow emission.

5). The latter may be due to a combination of space filtering and the contamination from the diffuse emission that hide this intermediate velocity outflow to the CO (2–1) line.

The SiO (5–4) emission was detected in a narrower velocity range than the CO (2–1) emission (see the average spectrum in Fig. 5.6). The integrated velocity emission from -23 to -18 km s^{-1} (blue-shifted) and from -2.4 to 0 km s^{-1} (red-shifted) is shown in Fig 5.7. In Fig. 5.8 it is also shown a comparison between the continuum, CO (2–1), and SiO (5–4) emission presented in previous figures. Indeed, the SiO blue- and red-shifted emission shows a more complicated structure than the CO (2–1) emission, and they do not seem to trace the same structure in most of the cases. The SiO (5–4) red-shifted emission coincide with continuum components 1, but strong emission is also detected to the southwest of component 1. The SiO (5–4) blue-shifted emission shows a strong emission feature also to the southwest of component 1, apart from overlapping with component 1 itself. The interpretation of the SiO emission is not straightforward, but it is possible that the emission features to the southwest of component 1 are tracing an additional outflow not traced by the CO emission.

Previous studies have also shown differences between the structures traced by CO and SiO. In chapter 4 we presented the case of the OMC-2 outflows, in which a SiO structure was found but without a clear counterpart in CO. Examples of

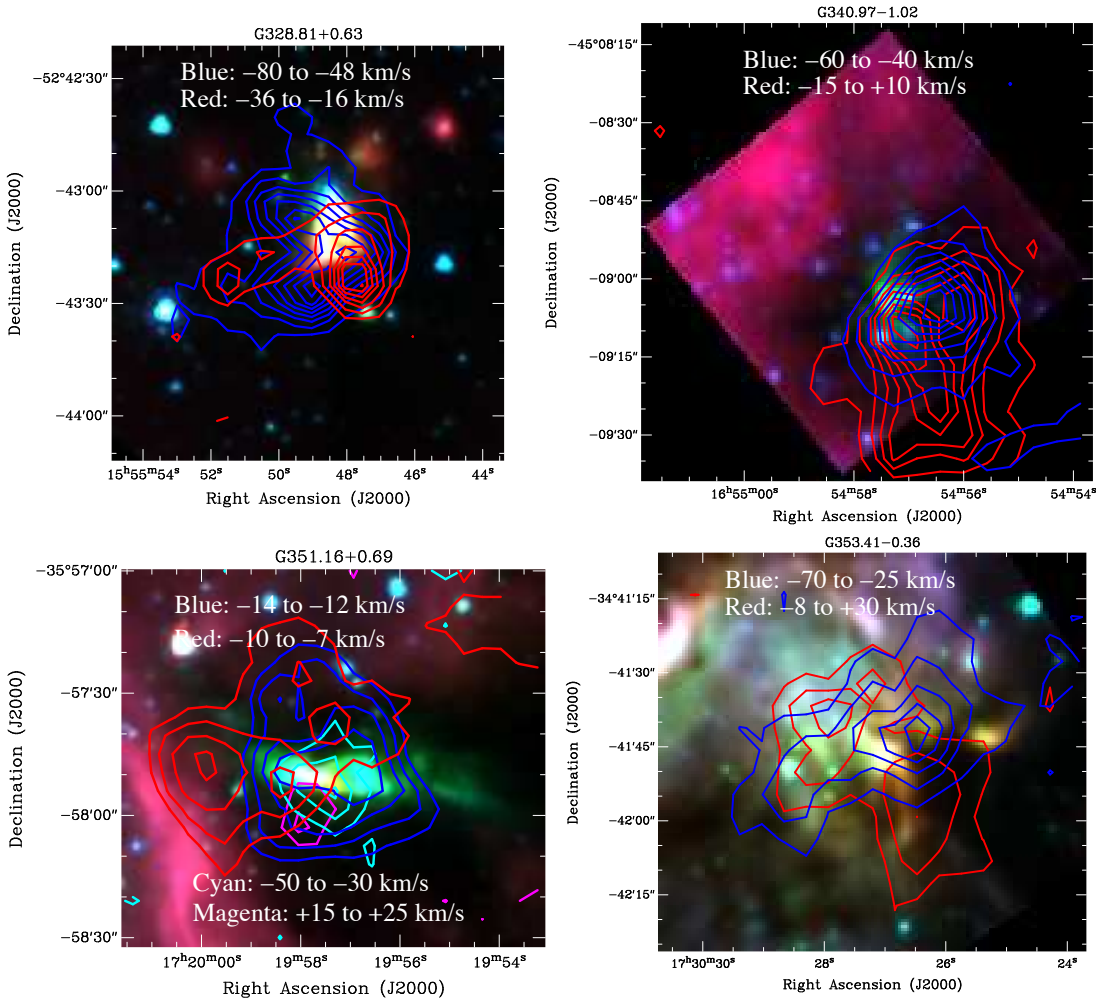

Figure 5.4: The CO (6–5) emission from ATLASGAL outflows. For all panels, blue and red contours start at 4σ and contour spacing is 3σ. In the case of the intermediate-velocity emission from G351.16+0.69 (blue and magenta contours) the first contour is 6σ and contour spacing is 3σ.

similar cases include the Orion-S region (Zapata et al. 2006) and IRAS 05358+3543 (Beuther et al. 2002a), which were actually observed with interferometers. Ruling out observational effects such as space filtering, the difference between the SiO and CO outflow emission can be attributed to shock chemistry effects (Gusdorf et al. 2008b). For example, from shock models in low-mass systems it is known that the shock velocity required to form SiO may not be reached in all outflows (Gusdorf et al. 2008b). In addition, observational evidence in low-mass outflows shows that evolved outflow sources do not present prominent SiO outflow emission (Bachiller 1996). However, it is important to point out that models to explain the SiO emission in massive systems are scare, and therefore it is not obvious whether a similar

Table 5.4: Parameters of the 1.4 mm continuum sources

	Component 1	Component 2
Peak intensity (Jy/beam)	0.85±0.08	0.56±0.04
Total integrated flux (Jy)	1.77	1.45
R.A. (J2000)	$17^h19^m57.41^s$	$17^h19^m57.73^s$
DEC (J2000)	$-35°57'52.3''$	$-35°57'52.27$
Deconvolved Major axis (arcsec)	4.1	4.9
Deconvolved Minor axis (arcsec)	3.4	4.3
Deconvolved Position angle (degrees)	-46.3	-7.2

explanation as in low-mass systems can be applied to massive outflows.

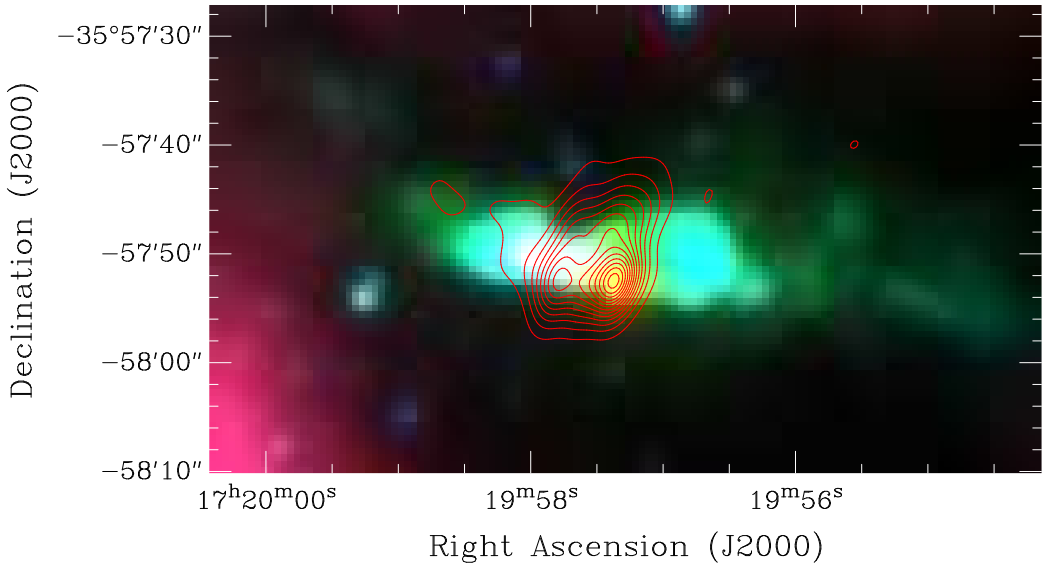

Figure 5.5: The 1.4 millimeter continuum emission (contours) in G351.16+0.69. The background shows the 3 color mid-IR image from Spitzer. First contour and contour spacing is 4σ (σ=16.2 mJy beam^{-1}).

5.5 Discussion

5.5.1 Comparison with Mid-IR observations

In Fig. 5.4 we have shown the outflow emission maps overlaid on the 3 color images from the GLIMPSE survey. In all the cases we found that the CO (6–5) outflow emission coincide with mid-IR features. However, in most of the cases the red-shifted emission is found in regions that are infrared dark, as expected since usually the infrared emission from the red-shifted lobes is obscured by the cloud.

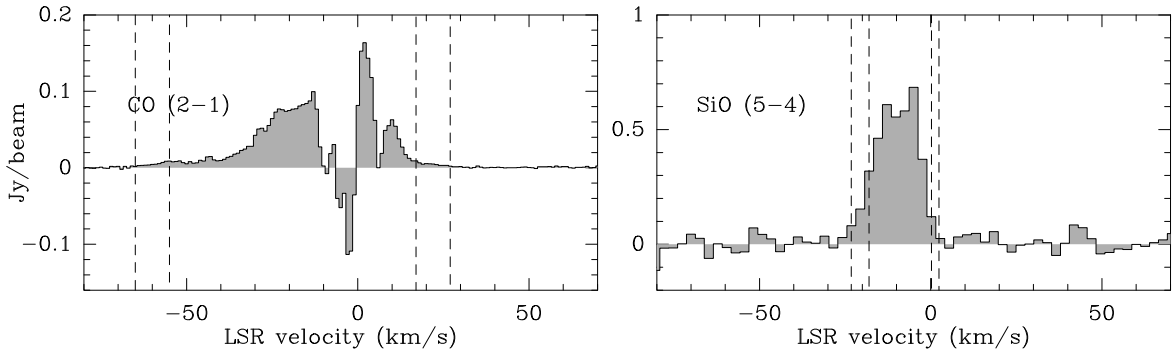

Figure 5.6: The CO (2–1) and SiO (5–4) SMA spectra in G351.16+0.69. The vertical dashed lines show the velocity ranges on which the maps in Fig. 5.7 were done.

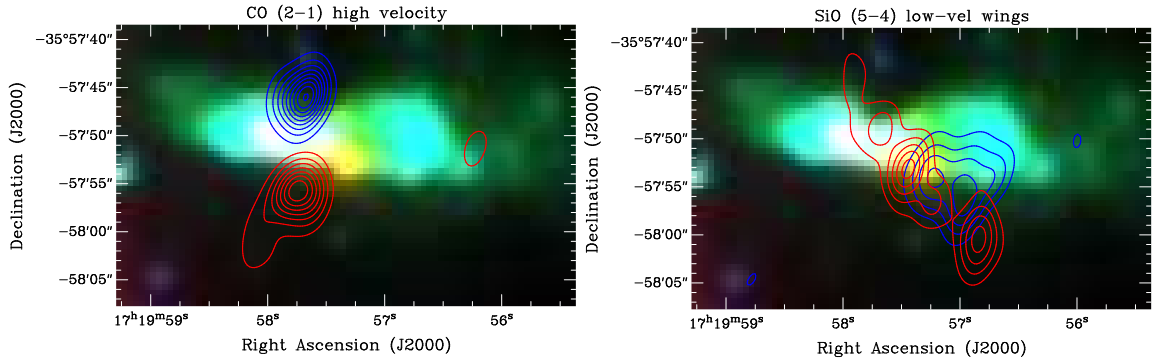

Figure 5.7: The CO (2–1) and SiO (5–4) emission (contours) compared to the mid-IR (color image) and millimeter continuum emission (grey scale) in G351.16+0.69. Blue and red contours are the blue- and red-shifted emission, respectively. Contour spacing and first contour is 4σ (σ =0.199 and 0.174 Jy beam, SiO blue-shifted and red-shifted, respectively; σ = 0.274 and 0.253 Jy beam, CO blue-shifted and red-shifted, respectively). Note that the velocity ranges are different for each molecule, with the SiO (5–4) detected at lower velocities (blue: -23.2 to -18.0 km s^{-}1, red:-2.4 to +0.2 km s^{-}1) compared with the CO (2–1) emission (blue: -65.0 to -55.0 km s^{-}1, red: +17.0 to +27.0 km s^{-}1).

Also, in several cases the morphologies of the emitting regions are different between the two tracers. We discuss each of the sources in more detail next:

G328.81+0.63. The main southern mid-IR lobe described in the previous section is mostly coincident with the blue-shifted CO emission. However, this blue-shifted structure seems to extend in a slightly different direction than the mid-IR lobe. A substantial part of the blue- and red-shifted lobes are seen projected against regions that are infrared dark.

G340.97−1.02. The blue- and red-shifted emission is indeed coincident with the main mid-IR structure. In particular, the inner part of the main red-shifted lobe

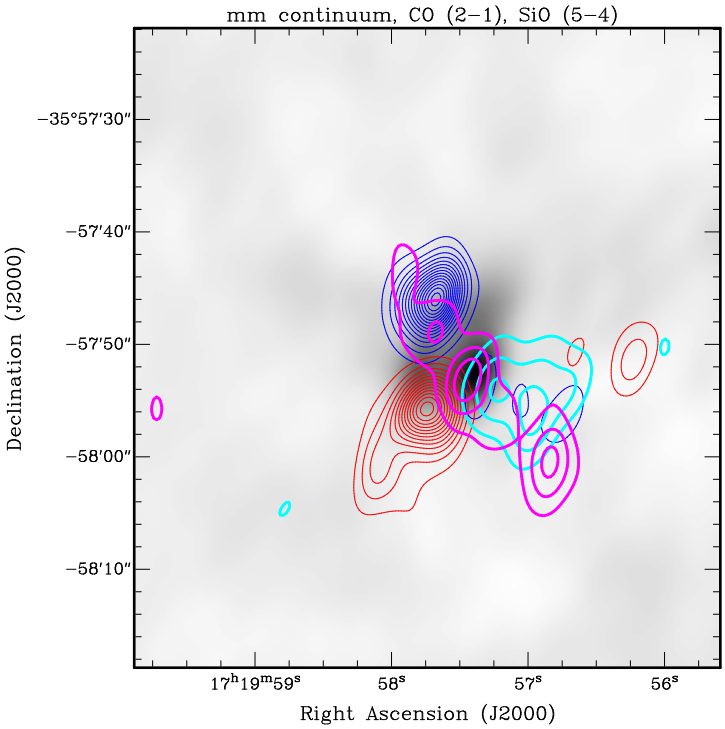

Figure 5.8: The CO (2–1) and SiO (5–4) emission (blue/red and cyan/magenta contours, respectively) from Fig. 5.7 overlaid on the millimeter continuum emission (grey scale). Contour spacing in this case is 6σ.

clearly overlap with the southern part of the *green excess* structure. However, other parts of the blue- and red-shifted structures lie in regions that are infrared dark, such as the terminal parts of the main red-shifted lobe, the second red-shifted peak, and the blue-shifted peak.

G351.16+0.69. The intermediate- and high-velocity CO emission overlaps with the main mid-IR structures. In particular, the intermediate-velocity blue-shifted emission traces the west lobe that is a prominent in *green excess*. Its counter-lobe, the red-shifted intermediate-velocity emission, has only a mid-IR counterpart towards its inner region. On the other hand, as revealed more clearly in the low−J CO emission, the high-velocity blue- and red-shifted emission does not show a mid-IR counter part, and indeed such high-velocity emission seems to trace an outflow perpendicular to the mid-IR east-west outflow. Interestingly, the SiO emission that is only detected at low velocities, has been found clearly tracing the jet-like structure revealed by the 8μm emission. In addition, the SiO emission may be tracing a third outflow structure to the south of the main western lobe, which also does not have counterpart in the mid-IR.

G353.41−0.36. The north-south outflow in the western part of this region seems to be coincident with a location that is mainly infrared dark. On the other hand, the blue- and red-shifted emission in the eastern side are coincident with patches that

Table 5.5: Outflow peak positions.

Position	α(J2000) (^{h} ^{m} ^{s})	δ(J2000) ($^\circ$ $'$ $''$)	v_{min}/v_{max} (km s^{-1})	$\int$ T$_{MB}$dv(σ) (K km s^{-1}) 6–5	7–6	6–5/7–6
G328.81-B1	15:55:48.9	−52:43:25	-80/-48	130.2(2.1)	106.8(5.4)	1.22(0.06)
G328.81-R1	15:55:47.7	−52:43:22	-36/-16	29.2(1.3)	26.8(4.1)	1.10(0.17)
G328.81-B2	15:55:49.2	−52:43:08	-80/-48	109.2(1.7)	72.3(5.3)	1.51(0.11)
G328.81-R2	15:55:51.4	−52:43:22	-36/-16	13.6(1.8)	14.4(5.0)	0.94(0.35)
G340.97-B1	16:54:56.5	−45:09:06	-60/-40	27.4(2.0)	34.4(4.1)	0.80(0.11)
G340.97-R1	16:54:56.7	−45:09:13	-15/10	11.4(1.4)	9.5(3.7)	1.2(0.49)
G351.16-B1	17:19:57.5	−35:57:50	-50/-30	19.2(1.7)	14.3(3.7)	1.34(0.37)
G351.16-R1	17:19:57.7	−35:58:00	15/25	23.4(1.3)	3.1(3.1)	7.5(7.5)
G353.41-B1	17:30:26.4	−34:41:42	-70/-25	84.4(2.5)	67.9(5.6)	1.24(0.11)
G353.41-R1	17:30:26.4	−34:41:56	-8/30	36.7(1.6)	30.6(4.0)	1.20(0.16)
G353.41-R2	17:30:27.8	−34:41:38	-8/30	48.1(1.8)	26.1(4.3)	1.84(0.31)

are infrared bright, but with no clear outflow morphologies. In general, as described above in this region it is difficult to distinguish outflow structures from the mir-IR images.

5.5.2 Excitation and physical conditions

As we have proceeded for low- and intermediate-mass outflows, we calculate the gas excitation and physical conditions by using LTE and non-LTE methods. For the LTE case we use the rotational diagram method as described in sect. 3.7.1 and 4.7.1, while the non-LTE calculations are performed with RADEX, as explained in sect. 3.7.2 and 4.7.2. For this analysis we have selected several positions in each of the regions, choosing the strongest CO (6–5) emission peaks in the blue and red lobes. The selected positions are listed in Table 5.5. The integrated CO (6–5) and CO (7–6) intensities in the wing range are used for the analysis, for which the CO (7–6) maps were convolved to the angular resolution of the CO (6–5) map.

The results of the rotational diagram analysis are presented in Table 5.6. Among the positions with temperatures $\geq$ 99 K we found G328.81-R1 (99 K), G328.81-R2 (140 K), G340.97-B1 (494 K). G351.16-R1 is the position with the lowest rotational temperature. In general positions in G328.81+0.63 and G340.97−1.02 show the highest rotational temperatures, while the lowest are found in G351.16+0.69.

In Fig. 5.9 we show the LVG results for the outflow selected positions. As in previous chapters, the results are presented as plots of thermal pressure (T×n) vs. T. Due to the degeneracy of the solutions, only lower limits can be given. The lower limits to the kinetic temperatures are similar to the rotational temperatures we have presented above, with the same tendency of higher temperatures towards G328.81-R1 ($\geq$100 K), G328.81-R2($\geq$150 K), and G340.97-B1 ($\geq$450 K). Similarly, the lower limits to the thermal pressure present higher values towards these positions. On the other hand, the lower limits for positions such as G351-R1, G353-R2, and G328-B2 show the lowest values.

Table 5.6: Rotational diagram results.

Position	T_{rot}(K)	N_T (10^{16} cm^{-2})
G328.61-B1	77±5%	5.5±18%
G328.81-R1	99±16%	1.1±53%
G328.81-B2	54±7%	6.1±25%
G328.81-R2	140±37%	0.5±129%
G340.97-B1	494±14%	2.0±49%
G340.97-R1	79±41%	0.4±138%
G351.16-B1	64±27%	0.9±93%
G351.16-R1	23±100%	4.1±336%
G353.41-B1	74±9%	3.6±30%
G353.41-R1	79±14%	1.5±47%
G353.41-R2	41±17%	4.0±57%

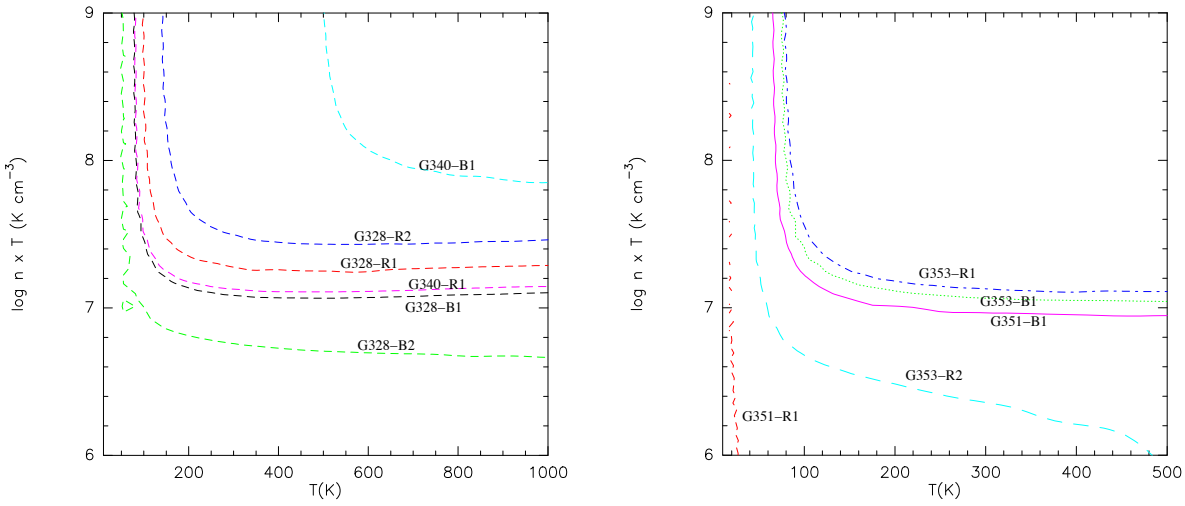

Figure 5.9: LVG results performed at selected positions of the ATLASGAL outflows. Each of the curves shows the observed line ratio at the position indicated by the labels.

A comparison with the results found in low- and intermediate-mass outflows shows that the excitation conditions in the high-mass outflows are at least as high as in the former cases. Indeed in the case of G340.97-B1 even physical conditions (kinetic temperature and thermal pressure) were found.

5.5.3 Outflow mass and energetics

From the CO (6–5) emission integrated in the wing range, we have calculated the outflow mass in a way similar to the one used in previous chapters, i.e. from the integrated intensity maps and assuming that the emission is optically thin (see equations 4.1, 4.2, and 4.3). Outflow parameter such as dynamical time scale, me-

Table 5.7: Outflow properties derived the mid$-J$ CO observations.

Velocity range	δv_{max} (km s^{-1})	R$_{max}$ (10^{-2}) (pc)	t_d (10^3) (yr)	M(H$_2$) (10^{-2}) (M$_\odot$)	F_m (10^{-3}) (M$_\odot$ km s^{-1} yr^{-1})	E$_k$ (10^{45}) (erg)	L_{mec} ($L_\odot$)
G328.81+0.63							
Blue	28	72.88	25.46	35.32	0.54	5.4	1.72
Red	36	60.69	16.49	16.06	0.49	4.1	2.00
Total				51.38	1.03	9.5	3.72
G340.97−1.02							
Blue	35	29.68	8.297	4.65	0.27	1.1	1.10
Red	35	39.19	10.95	10.18	0.45	2.4	1.80
Total				14.83	0.72	3.5	2.90
G351.16+0.69							
Blue	42	23.16	5.394	2.59	0.28	0.9	1.34
Red	33	16.17	4.792	3.53	0.34	0.7	1.27
I-Blue	2	21.63	105.778	10.70	0.003	0.008	0.0004
I-Red	3	24.60	80.220	17.52	0.009	0.03	0.003
Total				34.34	0.63	1.6	2.61
G353.41−0.36							
Blue	53	54.10	9.986	12.45	0.92	6.8	5.55
Red	47	59.73	12.432	12.84	0.68	5.5	3.62
Total				25.29	1.60	12.3	9.17

chanical force, kinetic energy, and mechanical luminosity have been also calculated following the equations shown in previous chapters (see, sect. 4.8), and assuming the kinematic distances from Table 5.1. As pointed out already, the methods used to calculate the the outflows' parameters are usually accurate within a factor of 2-3 for the mass determination and within 10-30 for the kinematic parameters. The outflow's parameters are presented in Table 5.7 for each of the four massive regions. Table 5.7 shows the outflows' parameters for the blue- and red-shifted lobes separately and also the total values. In the case of G351 we show separately the intermediate-velocity ranges as well. The total outflow masses are 5.1×10^{-1} M$_\odot$, 1.4×10^{-1} M$_\odot$, 3.4×10^{-1} M$_\odot$, and 2.5×10^{-1} M$_\odot$, for G328.81, G340.97, G351.16, and G353. We found that without taking into account the intermediate-velocity range in G351.16 the outflow's mass would amount to only 6.1×10^{-2} M$_\odot$. In general we see that the outflows' mass determined in these massive regions are between one and two orders of magnitude larger than the masses estimated in previous chapters for low- and intermediate-mass outflows, in agreement with previous findings using low$-J$ CO transitions.

Outflow's parameters such as mechanical force, kinetic energy, and mechanical luminosity range from about 3×10^{-6} to 1.6×10^{-3} M$_\odot$ km s^{-1} yr^{-1}, 8×10^{42} to 1×10^{46} erg, and 4×10^{-4} to 9 $L_\odot$, respectively. In order to compare these results with previously reported values for sources of different masses, in Fig. 5.10 plots of protostellar envelope mass versus outflow force and luminosity are presented. In

total 8 sources are included in these plots (sources whose full outflow extension was not mapped were excluded), and therefore this comparison is only tentative due to the low statistics. In Fig. 5.10 it is shown that, excluding the cases of L1448 and OMC-3 MMS 5 (indicated in the figure), the tendency is similar to previous studies based on low$-J$ CO lines (e.g. Beuther et al. 2002; T08), i.e. sources in low-mass star forming regions have lower mechanical force and luminosities than sources in high-mass star forming regions. However, the difference between low- and high-mass star forming regions is only between one and two orders of magnitude, which is then close to range of uncertainties in the determination of the outflows physical parameters. Remarkable is the fact that L1448 and OMC-3 MMS5 show similar values to the high-mass case. It is important to point out that the distance determination to the high-mass sources plays an important role in the calculations, and may be driving the tendencies seen in Fig. 5.10. The conclusion here is that, owing to the few sources in our sample together with the uncertainties in the determination of the outflow physical conditions, in particular for high mass sources whose distances are poorly known, no clear tendencies of the outflow energetics as a function of protostellar properties can be firmly given. Mid$-J$ CO observations in a larger sample are needed to verify whether the trends obtained with low$-J$ CO lines are also seen by using higher excitation CO lines.

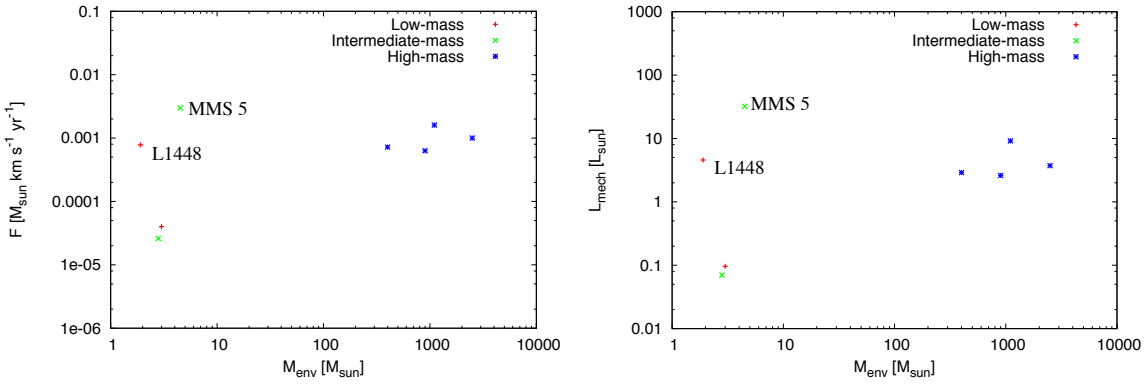

Figure 5.10: Outflow's versus protostars properties. Right: Envelope mass vs. Outflow force. Left: Envelope mass vs. outflow mechanical luminosity.

5.6 Summary and conclusions

The main results from this study are:

- Strong mid$-J$ CO emission was found tracing the high-velocity gas likely related to outflows in four massive star formation regions selected from the ATLASGAL survey.
- In each field, more than one bipolar outflow may be present, based on the morphology of the mid$-J$ CO emission.

- We find a spatial correlation between the CO outflow lobes and the mid-IR emission obtained from GLIMPSE archival data. Out of them, at least two fields (G340.97 and G351.16) show a clear excess in the 4.5μm band. However, usually the red-shifted lobes were found in regions that are infrared dark.

- Additional interferometric low$-J$ CO and SiO observations in G351.16 confirmed the multiple outflow system in this region.

- G351.16 shows one of the more peculiar cases based on the CO, SiO, and mid-IR images. The intermediate-velocity CO emission, revealed only by the mid$-J$ CO lines, traces the east-west flow that is also prominent in *green excess*. The high-velocity CO emission traces a north-south outflow, most prominent in the interferometric low$-J$ CO map, and without a mid-IR counterpart. Finally, a jet-like structure that dominates in the mid-IR at 8.0 μm, is mostly traced by the SiO emission and the high-velocity CO emission.

- Although partially, the outflow's physical parameters as determined throughout the mid$-J$ CO lines follow the trends already revealed by low$-J$ CO observations. However, additional observations in a larger sample are needed to verify whether or not this is the case.

Chapter 6

Hot gas in outflows: High-J CO emission in the Cepheus E protostellar outflow[1]

6.1 Introduction

Observations over the past few decades have shown that during the star formation process, mass accretion is commonly associated with mass ejection in the form of jets. The interaction between the jet and the parent cloud generates shock fronts, that form large cavities called bipolar outflows. The simultaneous presence of jets and bipolar outflows, as well as accretion disks surrounding protostellar condensations, are commonly observed (Arce et al. 2007), making them the basic elements of the star formation scenario. In this picture, different excitation regimes, related to the different structures, are revealed with a diversity of observational probes, such as continuum emission and molecular transitions at different wavelengths. In the jet/outflow system, at its temperature peak the shocked material is mainly radiatively cooled through the near-IR transitions of H_2, whereas the low-lying CO transitions trace the lower density, lower temperature (< 50 K) post-shock gas. In-between those two extreme regimes and over the 100-2000 K range, the cooling of the gas occurs mainly through the emission of atomic and molecular lines such as [OI], H_2O, high$-J$ CO, OH, and H_2 transitions, which fall in the mid- to far-infrared spectral range (Nisini et al. 1999).

Traditionally, the physical conditions of the gas in protostellar outflows have been studied by means of ground-based observations of low-lying rotational transitions of the CO molecule (usually up to $J_u = 3$, corresponding to $E_u < 50$ K). In most cases, these low-energy transitions are more sensitive to the low excitation swept-up gas, not exclusively related with the jet and/or shock front. On the other hand, higher-lying transitions ($E_u \gtrsim 100$ K) probe the warm gas unambiguously related with

[1]Based on Gómez-Ruiz, Gusdorf, Leurini, Codella, Güsten, Wyrowski, Requena-Torres, Risacher, Wampfler. High-J CO emission in the Cepheus E protostellar outflow observed with SOFIA/GREAT. A&A, 542, L9

the jet and/or hot spots in the shocked gas. However, transitions with relatively high$-J$ rotational quantum numbers (e.g. $J_{\rm u} \geq 9$) fall into the window of the far-infrared regime that can not be observed from the ground. High$-J$ CO observations were pioneered with the *Infrared Space Observatory* (ISO), which actually targeted several protostellar outflows (Nisini et al. 1999, 2000; Giannini et al. 2001). These ISO observations revealed that the high$-J$ CO emission does indeed trace outflowing gas above 1000 K, but their poor spectral resolution did not allow us to probe either the presence of different spectral components, or the physical conditions of the gas as a function its velocity. In addition, their low spatial resolution ($\sim 80''$ at wavelengths corresponding to its Long Wavelength Spectrometer, LWS) complicates the analysis owing to the presence of different structures within the same beam. Only recently, with the *Herschel* Space Observatory in operation and the Stratospheric Observatory for Far-Infrared Astronomy (SOFIA) starting operation, we had the opportunity to follow-up on these previous studies with high-resolution FIR spectroscopy and angular resolutions in the 15-20$''$ range.

In this chapter, we present one of the first studies of two high$-J$ CO spectrally resolved lines in a protostellar outflow, as an example of the potential of SOFIA observations with GREAT in the context of protostellar jets/outflows.

6.2 The source

For this study, we selected the protostellar outflow Cep E, in the Cepheus molecular cloud, since it is associated with a relatively nearby ($\sim$730 pc) intermediate-mass class 0 source (IRAS 23011+6126: Chini et al. 2001) of 100 $L_\odot$, surrounded by an envelope structure of mass $\sim$ 18 $M_\odot$. The jet/outflow system itself has been intensively studied at multiple wavelengths (Eislöffel et al. 1996; Lefloch et al. 1996; Moro-Martín et al. 2001; Smith et al. 2003). Near- and mid- Infrared observations have revealed a clear bipolar morphology that within each lobe shows features such as cavities, bow-shocks and knots of gas emitting in vibrational and ro-vibrational H_2 transitions (Eislöffel et al. 1996; Velusamy et al. 2011). The CO spectrum shows strong wings and also secondary peaks at extremely high velocities, the latter possibly related with the jet component. Indeed, Cep E is one of the few young stellar objects know to have such extremely high velocty component. All these characteristic make the Cep E outflow an ideal target for the study of the high$-J$ CO emission in jet/outflow systems.

6.3 Observations

The SOFIA telescope was pointed towards the southern lobe of the Cep E outflow (Fig. 6.1). As seen in Fig. 6.1, the SOFIA observations covered the infrared knots BI and BII. The observations were performed during basic science flights in July

Table 6.1: The CO observations.

CO Line	ν_0 (GHz)	E_u/k (K)	HPBW ($''$)	rms[a] (mK)	τ_{atm}	t_{ON} (min)
(13–12)	1496.9922	503.1	20.0	82	0.03	15
(12–11)	1381.9951	431.3	21.7	96	0.16	7.4
(2–1)[b]	230.5380	16.6	20.0	32	-	-

[a] T_{MB} scale, at 3 km s^{-1} spectral resolution.
[b] Convolved to 20$''$ from original $\sim$ 11$''$ resolution (IRAM-30m), Lefloch et al. in prep.

2011, with the German Receiver for Astronomy at Terahertz Frequencies (GREAT[2]: Heyminck et al. 2012). The L1 band of the GREAT instrument was used to observe, in two separate flights, the CO (12–11) and (13–12) transitions at ∼1.4 THz and ∼1.5 THz, in the lower and upper sidebands, respectively. In Table 6.1, the line frequencies, diffraction-limited beam sizes, time ON source (t_{ON}), and atmospheric opacities (τ_{atm}) during the observations are presented. The front-end was connected to the AFFTS back-end (Klein et al. 2012), providing a total bandwidth of 1.5 GHz and a spectral resolution of 212 kHz, that at the observed frequencies correspond to $\sim$ 300 km s^{-1} and ∼0.4 km s^{-1}, respectively. Single pointing observations were done in double-beam chopped mode, with a chop throw of 60$''$ in RA (at 1 Hz). The pointing was established with the optical guide cameras, and was stable to 4$''$. The calibration uncertainty is within 20%. From observations of Jupiter and Mars, a main-beam efficiency of 0.54±0.05 in the L1 band was determined (Heyminck et al. 2012), that - with a forward efficiency of 0.95 - was used to convert antenna to main beam temperatures, T_{MB}. Subsequent analysis of the data was done with CLASS within the GILDAS software[3], following the standard procedures of baseline subtraction and spectra averaging. A first-order baseline was subtracted from all spectra.

Calibration was performed by carefully fitting the observed sky emission (Guan et al. 2012). Unfortunately, both CO transitions suffer from residual terrestrial atmospheric features at SOFIA's flight altitude: the CO (12–11) detection bandwidth contains a strong water absorption (from the signal band) at positive velocities >60 km/s. This does not however affect the calibration of the pre-dominantly negative velocity emission towards the southern lobe. This is different for CO (13–12), whose calibration (and baselines) at extremely negative velocities (of lower than - 120 km s^{-1}) are more uncertain owing to an image band atmospheric feature. However, quite comparable integrated intensities for both lines at small S/N values supports our confidence in the adopted calibration procedure.

[2] GREAT is a development by the MPI für Radioastronomie and the KOSMA/Universität zu Köln, in cooperation with the MPI für Sonnensystemforschung and the DLR Institut für Planetenforschung.
[3] http://www.iram.fr/IRAMFR/GILDAS

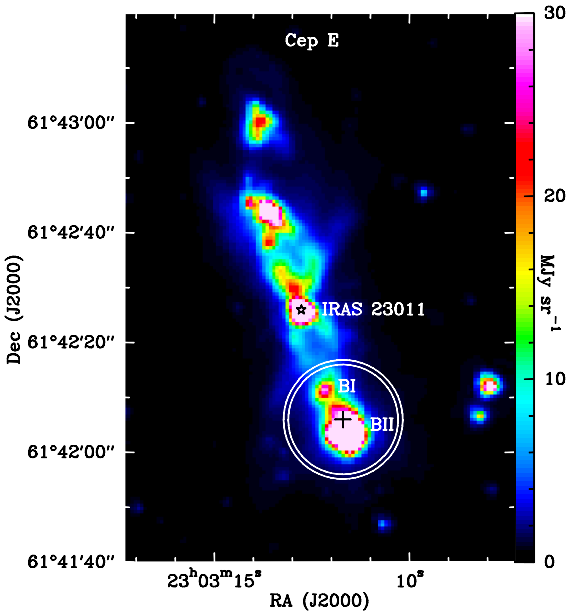

Figure 6.1: *Spitzer*/IRAC band-two (4.5 μm) image of the Cep E protostellar outflow (retrieved from the *Spitzer* archive). White circles mark the diffraction-limited SOFIA beams at the frequencies of CO (12–11) and (13-12) (decreasing beam size with increasing $J_{\rm u}$, see Table 6.1), centered at the brightest IR knot of the southern lobe, $\alpha = 23^h03^m11^s70$ $\delta = +61°42'06.0''$ (black plus symbol). White letters label the two main knots inside our beams, BII and BI, as well as the Cep E central source (IRAS 23011: black star).

6.4 Results

Together with the SOFIA/GREAT spectra, in Fig. 6.2 we also show a CO (2–1) line profile taken at the corresponding position from a Nyquist sampled map, obtained with the IRAM-30m telescope (Lefloch et al., in prep). The CO (2–1) spectrum was convolved to a beam of 20″ (i.e. the SOFIA beam at the (13–12) transition, see Table 6.1). From the CO spectra shown in Fig. 6.2 at least three spectral features can be distinguished: two secondary peaks, at around −125 km s^{-1} and −65 km s^{-1}, and a wing-like profile (smooth decrease of intensity towards high velocities) in the range from −50 km s^{-1} to −20 km s^{-1}. The secondary peaks are similar to the so-called molecular 'bullets' often observed in the spectrum from class 0 protostars and likely related to the jet component (e.g. L1448: Bachiller et al. 1990). These 'bullets' were reported previously in Cep E (Lefloch et al. 1996). The wing-like feature is typical of the outflow phenomenon, mostly tracing the cavity walls crated by the jet, and usually referred to as the 'standard' high-velocity component (e.g., Bachiller et al. 1990). On the basis of these spectral features, in Fig. 6.2 we divide all spectra into three velocity ranges: extremely high velocity (EHV: −140 to −100 km s^{-1}), intermediate-to-high velocity (IHV: −100 to −50 km s^{-1}), and standard high velocity (SHV: −50 to −20 km s^{-1}). In Table 6.2, we present the line intensities integrated within the defined velocity ranges. From the

spectra in Fig. 6.2, one can see that the bullet-like profile in the IHV range is more prominent in high$-J$ than in low-J CO, with the latter still being dominated by the wing-like profile that extends into this velocity range. On the other hand, the SHV component is stronger in low$-J$ than in high$-J$ CO. From the integrated intensities in Table 6.2, we found that the (2–1)/(12–11) ratio is about 0.8, 0.4, and 2.2, for EHV, IHV, and SHV, respectively, indicating different excitation conditions in the different velocity ranges. These findings underline the necessity for velocity-resolved spectroscopy in the excited CO transitions, to identify the bullets as distinct features. The significant emission of the high$-J$ CO line at high-velocity indicates that it is very likely related to the jet component, unlike the wing component, which becomes weaker in these lines. Finally, the emission at low velocities is still considerable in our high$-J$ CO lines. This implies that the *a priori* assumption made in the analysis of some ISO observations, namely that the excited CO emission originates exclusively from the high-velocity gas (e.g. Nisini et al. 2000), could be incorrect.

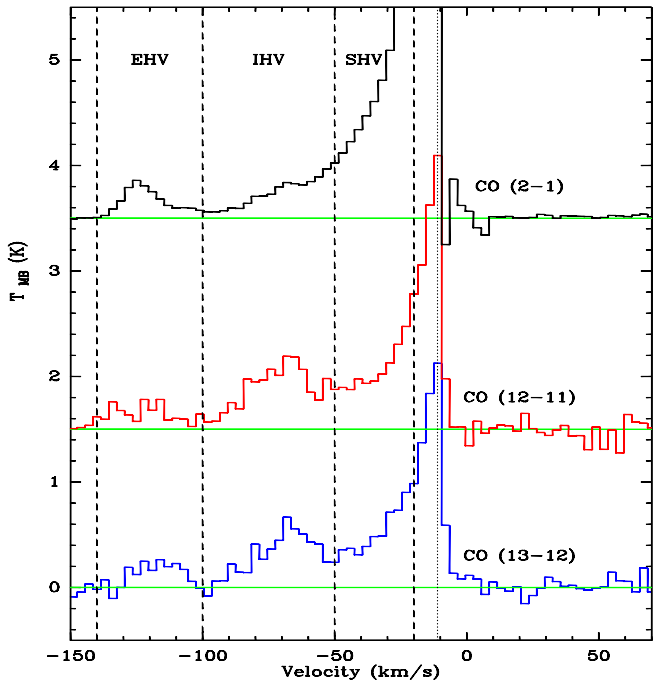

Figure 6.2: SOFIA/GREAT spectra of CO (12–11) and (13–12) in Cep E, together with the low$-J$ CO (2–1) transition, taken at the position shown in Fig. 6.1. The CO (13–12) and (2–1) spectra are taken from data with a spatial resolution of 20″, while the spatial resolution of the CO (12–11) is 21.7″. The two upper spectra have been shifted along the Y-axis. The green horizontal lines show the zero level of each spectrum. The dashed vertical lines indicate the limits of each velocity range defined in Table 6.2. The dotted vertical line shows the systemic velocity (-11 km s^{-1}). The spectral resolution is 3 km s^{-1} for all lines.

Table 6.2: Velocity ranges and integrated intensities.

CO	$\int T_{\rm MB}$dv (K km s^{-1})^a		
Transition	EHV	IHV	SHV
13–12	4.8(0.9)	14.9(1.0)	16.1(0.8)
12–11	6.0(1.0)	19.5(1.2)	17.7(0.9)
2–1	5.1(0.2)	8.8(0.3)	38.9(0.2)
EHV: -140 to -100 km s^{-1}; IHV: -100 to -50 km s^{-1}			
SHV: -50 to -20 km s^{-1}			

[a]Statistical errors in parenthesis.

6.5 Discussion: physical conditions

To constrain the physical conditions, we performed radiative transfer calculations with the RADEX code (van der Tak et al. 2007) based on the large velocity gradient (LVG) approximation and assuming a plane-parallel 'slab' geometry for the escape probability formula. The molecular data were retrieved from the LAMDA data base[4]. The collisional rate coefficients were adopted from Yang et al. (2010), who calculated the collisional rates between CO and H_2, incorporating energy levels up to $J = 40$ for kinetic temperatures of up to 3000 K.

For the purposes of our study of the physical conditions as a function of velocity, we use the integrated intensities in the EHV, IHV, and SHV ranges (Table 6.2). The value that we adopt for the linewidth, Δv, is directly inferred from the definition of our different velocity ranges (40, 50, and 30 km s^{-1}, for EHV, IHV and SHV, respectively). Our background radiation field is assumed to only be produced by the CMB. Then, our procedure consists in running, for each velocity range, a grid of RADEX models to compute the integrated intensities within a three-dimensional parameter space defined by T (kinetic temperature), n (H_2 volume density), and N(CO) (CO column density).

The LVG results were analyzed based on the (2–1)/(12–11), (2–1)/(13–12) line ratios and the absolute integrated intensities of those three lines. We point out that owing to the use of these ratios the results are biased toward the lower excitations traced by the low$-J$ CO lines, and hence our results should be assumed to be lower limits. We use the IR size of the BI ($\sim 3'' \times 4''$) and BII ($\sim 8'' \times 8''$) knots to compute the brightness temperature, correcting for beam dilution effects. For the SHV component, we assumed the size of BII, while for the IHV and EHV components the size of BI was assumed. These assumptions are based on the knowledge that the EHV and IHV low$-J$ CO emission peaks around BI, while the SHV emission peaks around BII (Hatchell et al. 1999). The LVG solutions were found when both the ratios and absolute integrated intensities match in the (T, n) plane. The N(CO) ranges constrained in this way are 4-9$\times 10^{17}$, 4-6$\times 10^{17}$, and 1-4$\times 10^{17}$ cm^{-2}, for the SHV, IHV, and EHV components, respectively. We tested the influence of the

[4]http://www.strw.leidenuniv.nl/∼moldata/

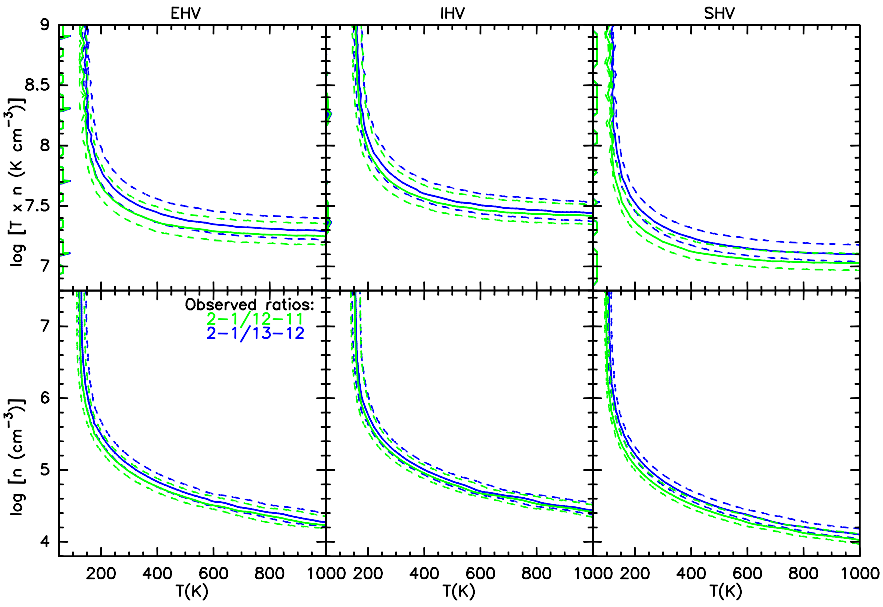

Figure 6.3: LVG results produced by the RADEX code for the observed intensity ratios in the EHV, IHV, and SHV ranges (left, middle, and right panels, respectively). The results are shown as T vs. n and $n \times T$ (thermal pressure) vs. T plots (lower and upper panels, respectively). The CO (2–1)/(12–11) ratio is indicated in green and the CO (2–1)/(13–12) ratio in blue. The observed ratio is drawn with solid lines, while the line ratio uncertainty (including statistical and 20 % of the calibration errors) with dashed lines. $N = 2{\times}10^{17}$, $5{\times}10^{17}$, and $7{\times}10^{17}$ cm^{-3}; and Δv = 40, 50, and 30 km s^{-1}, for EHV, IHV, and SHV, respectively.

size of the emission region on our N(CO) conclusions by varying the assumed size from a compact emission scenario, where the emission spreads over half the BI knot size, to a very extended case in which the filling factor is equal to one. Over this range, we found that N(CO) varies over up to two orders of magnitude. However, this change in N(CO) does not modify significantly the solution of the line ratios described below. In Fig. 6.3, we show the RADEX results as plots of T versus (vs.) n and $(n \times T)$ vs. T. In the latter, $(n \times T)$ represents the thermal pressure, and is shown because in the LVG analysis the results are not as degenerate as for T vs. n (see Fig. 6.3). The (2–1)/(12–11) and (2–1)/(13–12) ratios yield lower limits to the parameters of $T \gtrsim 100$ K, $n \gtrsim 4.2{\times}10^4$ cm^{-3}, and $(n{\times}T) \gtrsim 10^7$ K cm^{-3}. These lower limits indicate that the line ratios actually trace high densities and temperatures, but the remarkable result of our LVG analysis is that the thermal pressure tends to be higher in the IHV range than in both the EHV and SHV ranges. In addition, it is quiet a surprise that both EHV and SHV provide similar constraints, since it is usually found that the EHV component (probably related to the jet) has higher excitation than the SHV component (which is likely to trace the outflow cavity).

The H_2O mapping observations at 183 GHz of Lefloch et al. (2011), which covered the blue lobe and the central region of Cep-E with an angular resolution of $\sim$13″, also showed prominent bullet-like spectral features in the IHV range. The strongest emission was found around the central region, while weaker and no emission at all was found at BI and BII, respectively. Together with additional SiO (8–7) observations, LVG calculations made for the gas in the central region yielded the physical conditions of $T \sim 200$ K and $n \sim 10^6$ cm^{-3}, which are comparable to the ones reported here, suggesting that the SiO, H_2O, and high$-J$ CO emission arises from gas with similar physical conditions, despite the different frequency range and positions probed. A correlation between the physical conditions of these molecules is an expected result given that the considered formation routes of SiO and H_2O associate themselves with warm and dense gas. However additional observations are required to verify the spatial correlation between these molecules and to provide more accurate determinations of the physical conditions.

Previous ISO observations of CO transitions from (14–13) up to (25–26), yielded kinetic temperatures and H_2 densities in the range 200-1200 K and $4{\times}10^4$-$4{\times}10^6$ cm^{-3}, respectively. These constraints were obtained by fitting LVG models to the total integrated emission of these spectrally unresolved high$-J$ CO lines (Giannini et al. 2001; Moro-Martín et al. 2001). It is remarkable that our lower limits are in good agreement with the values obtained from ISO, although our results are given for three distinct velocity ranges over the same global one. However, a more complete LVG analysis is needed to strengthen our conclusions with respect to previous ISO studies, and to more clearly probe the physical conditions prevailing in the observed regions. Such an analysis should be based on additional observations of both lower- and higher-J CO transitions with the GREAT spectrometer, such as the (11–10) and (16–15) ones, the latter would also allow us to make direct comparisons with ISO observations.

Spectrally resolved *Herschel*/HIFI observations have been used to study the

emission in different velocity ranges in low-mass outflows by measuring the ratios of low− to high−J CO lines, which is an approach that is similar to our analysis. The kinetic temperatures generally inferred by those studies for the outflow components are in the range 100-200 K (Yıldız et al. 2010; Bjerkeli et al. 2011). These values are similar to our lower limits. As already pointed out, the line ratios of a few high−J CO lines with low−J CO lines bias the results toward lower excitation conditions, and could in the end be inappropriate owing to the different physical component possibly related to each of them, as it has been proven in a few outflows (van Kempen et al. 2010b). In this respect, additional observations of more high−J CO lines, as well low− and mid−J CO transitions, are required to test the possibility of the contribution of different physical components to the CO emission in outflows. Eventually, the combination of a maximum number of CO lines will provide the optimal way to shed light on the physical processes responsible for the existence of these components (e.g. Gusdorf et al. 2012; Visser et al. 2012).

6.6 Conclusions

The principal conclusions of the present study are:

- Our analysis of SOFIA/GREAT data has demonstrated that high−J CO lines are a good tracer of molecular bullets in protostellar outflows.
- The bullet at intermediate-to-high velocities has a higher level of excitation than the low and extremely high velocity gas, at the observed position of the Cep-E outflow.
- The still considerable low-velocity emission in high−J CO lines should be taken into account when modeling data.
- More and higher−J CO transitions must be observed to break the degeneracy in the LVG solutions.

Chapter 7

Conclusions and perspectives for future work

Here a summary of the main contributions of this thesis as well as the perspective for future work are presented:

The complex chemical-kinematical structure of protostellar outflows

As observed at high spatial resolution, the SiO, H_2CO and CH_3OH emission in the L1157 protostellar outflow present a complex position-velocity distribution. In particular, the emission at the main shock of the blue lobe, which has been selected as target for multiple chemical studies, shows a more complex (clumpy) structure than previously known. The H_2CO and CH_3OH lines trace (or delineate) the U-shaped structure, with a similar overall distribution of both species. On the other hand, the SiO emission was found mainly tracing a high-velocity compact clump at the tip of the U-shaped structure, surrounded by additional lower velocity clumps. Since the SMA observations recovered only $\sim$10% of the low velocity emission at this position, it is very likely that the low-velocity SiO is spatially extended. However, it is not clear whether these features revealed by the SiO emission at the tip of the U-shaped structure are indicating the presence of multiple shocks, or alternatively a single shock interacting with a pre-existing clump(s). All these results show therefore how when observed at high-angular resolution, different chemical tracers can be tracing different kinematical structures in protostellar outflows.

One of the main outcomes from the data presented in this theses for L1157 is that the multitude of observations currently underway to observe different molecular transitions taking this source as the prototype of chemically active outflow should take into account the possibility that L1157 maybe a peculiar case of outflow, not representative of a general case, even within the class 0 phase (other class 0 sources, e.g. BHR 71, do not show such chemical activity). It is clear that a more comprehensive study surveying an statistical significant sample is needed to verify whether or not L1157 is a particular case, or whether chemical active outflows are a common characteristic among class 0 protostars. One of such studies have been started by

surveying molecular lines in another prototypical class 0 outflow: L1448-mm. Tafalla et al. (2010) observed the later source, which is a prototype of highly collimated outflow with extremely high-velocity emission, finding that the high-velocity gas in this source present chemical similarities with the L1157 outflow. However, since these observations were performed with a single-dish instrument, the spatial distribution of the different molecules could no be tested. As an interferometric follow-up to this study, we have proposed EVLA observations covering several molecular lines at high spatial resolution. The future of this field of research will be drastically improved as new observing facilities, able to observe simultaneously several molecular lines, come on-line within the next few years, e.g. EVLA and ALMA.

The distribution of the warm gas in protostellar outflows

The mid$-J$ CO emission in the mostly isolated star forming regions L1448 and HH211 shows that the warm gas in their corresponding outflows is prominent in the high-velocity gas close to the exciting source and the terminal bow shocks, suggesting that energetic processes are at work in these environments and are especially traced by these lines. Extremely High Velocity emission in L1448-mm was detected in both CO (6–5) and (7–6) transitions from the clumps inside a radius of about 10" from the central object. By a comparison with previous observations it has been found that the mid-J CO (6–5) and (7–6) emission is stronger towards the central region of L1448-mm than the low-J CO emission. Similarly, the terminal bow shocks in both objects are stronger in mid-J CO (6–5) and (7–6) than in low$-J$ CO. A LVG analysis, that includes far-IR CO lines from ISO, shows that is not possible to fit simultaneously the mid$-J$ and high$-J$ CO lines with only one component, for both L1448-mm and HH211-mm outflows, which may support recent studies that propose multiple physical components. A relevant result obtained from the mid$-J$ CO observations in L1448 and (partially) in HH211 is that even at low velocities the emission clearly defines the outflow structures, which is remarkably different from what we see in low$-J$ CO lines.

In our relatively large scale mid$-J$ CO mapping of the OMC-2/3 region, which covered several intermediate-mass protostars in different evolutionary phases, we found that the warm gas is especially prominent in early class 0 type sources. In addition, we have discovered in the CO (6–5) and (7–6) lines an extremely high velocity outflow in OMC-3 MMS5, that was not revealed by previous CO (3–2) observations. By a comparison with previous observations, it has been found that the CO (6–5) and (7–6) emission is stronger towards the location of the central objects than the low-J CO (3–2) emission. As in the case of the low-mass protostars, even at around the cloud velocity the outflow structures are clearly seen, in contrast with low$-$J CO observations in which the low-velocity gas from the outflow is hidden by the emission from the cloud. The kinematics and physical conditions of MMS 5 outflow suggest that it is the counterpart of the young class 0 low-mass outflows (e.g. L1448), and therefore that young intermediate-mass outflows are as energetic as their low-mass counterparts. The discovery of highly excited, extremely high-

velocity gas, by means of mid$-J$ CO observations, may indicate that this kind of outflow are particularly traced by mid$-J$ CO lines.

Strong mid$-J$ CO emission was also found in massive protostellar objects candidates. In each observed field, more than one bipolar outflow are present, consistent with what is usually found in this kind of environments. An important result from our observations is the discovery of a protostellar outflow whose axis is close to the plane of the sky and therefore of relatively low velocities. Only the mid$-J$ CO lines were able to trace this outflow, pointing out the importance of these lines in revealing outflows with this particular orientation. Given the cluster environments in which massive stars evolve, the low-velocity mid$-J$ CO emission, which very well traces outflow structures, proved to be an important tool to identify the outflows corresponding to each member of the system, reducing the confusion typical of the more traditional low$-J$ CO observations. Although partially, the outflow's physical parameters as determined throughout the mid$-J$ CO lines follow the trends already revealed by low$-J$ CO observations. However, additional observations in a larger sample are needed to verify whether or not this is the case.

Therefore, the overall picture presented by the mid$-J$ CO observations in protostellar outflows is a tendency to trace the most excited regions within them, i.e. the jet component and the terminal bow shocks, as expected owing to the higher energies required for their excitation compared with the low$-J$ CO lines. The mid$-J$ CO lines have proven also to be good tracers of the low-velocity emission in outflows, as well as important tracers of highly excited extremely high velocity emission. The later characteristics may suggest that unbiased surveys using mid$-J$ CO lines will reveal more easily outflows with EHV emission and also unveil outflows with axis along the plane of the sky that are hidden to the low$-J$ CO emission.

The perspectives for further studies in mid$-J$ CO lines include the mapping of complete clouds that were already mapped in low$-J$ CO transitions, in order to see how much the detection rates are affected by outflows orientated along the plane of the sky, that are not detectable in low$-J$ CO but revealed in mid$-J$ CO transitions. The recently proposed automatic methods to find outflow features in the three dimensional space would need to be updated to account for low-velocity outflow structures (see, e.g., Borkin et al. 2008). Including these missing outflows in the statistics will be an important factor to properly determine the contribution of protostellar outflows to the turbulence in molecular clouds.

If confirmed the tendency of finding EHV outflows more easily with mid$-J$ CO lines, these transitions would become a powerful tool to look for these objects that are currently scare but are of vital importance to study jets and their origin in star formation. But important to point out is that single-dish observations are not sufficient to resolve the jet structure. Therefore, synergy with ALMA is foreseen in this regard: perform large scale surveys with single-dish and later on follow them up with ALMA at higher angular resolution. Actually, ALMA early science observations will target the CO (6–5) emission in a low-mass outflow.

The hot gas in protostellar outflows.

The high$-J$ CO lines at terahertz frequencies proved to be important tracers of molecular bullets in the Cep-E intermediate-mass outflow. At the observed position in the Cep-E outflow, the SOFIA/GREAT spectrum revealed bullets at intermediate and extremely high velocities. The bullet at intermediate velocities has a higher level of excitation than the low and extremely high velocity gas. In addition, it was found that the low-velocity emission is still considerable in these high excitation lines, which thus means that it should be taken into account when modeling data.

Of all the projects presented in this thesis, this was the one which explored a relatively new technique in the study of protostellar outflows. The next step in the study of high$-J$ CO lines is the mapping of full outflow extensions, in order to trace the distribution of the hot gas. Actually, the mapping of high$-J$ CO lines are currently scheduled for observations with the Herschel observatory by a few groups. The potential with SOFIA is the mapping of higher$-J$ CO transitions than the ones possible to observe with Herschel. As a matter of fact, we have submitted a SOFIA/GREAT follow-up proposal to map the high$-J$ CO emission in the Cep-E outflow. The study of spectrally resolved high$-J$ CO lines is just starting and it will likely improve our knowledge of the hot gas in protostellar outflows.

Bibliography

Arce, H. G. 2003, in Revista Mexicana de Astronomia y Astrofisica, vol. 27, Vol. 15, Revista Mexicana de Astronomia y Astrofisica Conference Series, ed. J. Arthur & W. J. Henney, 123–125

Arce, H. G. & Goodman, A. A. 2002, ApJ, 575, 911

Arce, H. G. & Sargent, A. I. 2004, ApJ, 612, 342

Arce, H. G., Shepherd, D., Gueth, F., et al. 2007, Protostars and Planets V, 245

Aso, Y., Tatematsu, K., Sekimoto, Y., et al. 2000, ApJS, 131, 465

Avery, L. W. & Chiao, M. 1996, ApJ, 463, 642

Bachiller, R. 1996, Annual Review of Astron and Astrophys, 34, 111

Bachiller, R., Andre, P., & Cabrit, S. 1991a, A&A, 241, L43

Bachiller, R. & Cernicharo, J. 1986, A&A, 168, 262

Bachiller, R., Liechti, S., Walmsley, C. M., & Colomer, F. 1995, A&A, 295, L51+

Bachiller, R., Martin-Pintado, J., & Fuente, A. 1991b, A&A, 243, L21

Bachiller, R., Martin-Pintado, J., Tafalla, M., Cernicharo, J., & Lazareff, B. 1990, A&A, 231, 174

Bachiller, R. & Perez Gutierrez, M. 1997, ApJL, 487, L93+

Bachiller, R., Pérez Gutiérrez, M., Kumar, M. S. N., & Tafalla, M. 2001, A&A, 372, 899

Beltrán, M. T., Estalella, R., Girart, J. M., Ho, P. T. P., & Anglada, G. 2008, A&A, 481, 93

Beltrán, M. T., Gueth, F., Guilloteau, S., & Dutrey, A. 2004, A&A, 416, 631

Benedettini, M., Viti, S., Codella, C., et al. 2007, MNRAS, 381, 1127

Benjamin, R. A., Churchwell, E., Babler, B. L., et al. 2003, Public. of the Astron. Soc. Pac., 115, 953

Beuther, H. 2005, in X-Ray and Radio Connections (eds. L.O. Sjouwerman and K.K Dyer) Published electronically by NRAO, http://www.aoc.nrao.edu/events/xraydio Held 3-6 February 2004 in Santa Fe, New Mexico, USA, (E3.02) 8 pages

Beuther, H., Schilke, P., & Gueth, F. 2004, ApJ, 608, 330

Beuther, H., Schilke, P., Gueth, F., et al. 2002a, A&A, 387, 931

Beuther, H., Schilke, P., Sridharan, T. K., et al. 2002b, A&A, 383, 892

Bjerkeli, P., Liseau, R., Nisini, B., et al. 2011, A&A, 533, A80+

Bonnell, I. A. & Bate, M. R. 2005, MNRAS, 362, 915

Borkin, M., Arce, H., Goodman, A., & Halle, M. 2008, in Astronomical Society of the Pacific Conference Series, Vol. 394, Astronomical Data Analysis Software and Systems XVII, ed. R. W. Argyle, P. S. Bunclark, & J. R. Lewis, 145

Brogan, C. L., Hunter, T. R., Cyganowski, C. J., et al. 2009, ApJ, 707, 1

Burton, M. G., Ashley, M. C. B., Marks, R. D., et al. 2000, ApJ, 542, 359

Cabrit, S. & Bertout, C. 1986, ApJ, 307, 313

Cabrit, S. & Bertout, C. 1990, ApJ, 348, 530

Cabrit, S. & Bertout, C. 1992, A&A, 261, 274

Cesaroni, R., Galli, D., Lodato, G., Walmsley, C. M., & Zhang, Q. 2007, Protostars and Planets V, 197

Charnley, S. B., Tielens, A. G. G. M., & Rodgers, S. D. 1997, ApJL, 482, L203+

Chernin, L. M. & Masson, C. R. 1992, ApJL, 396, L35

Chini, R., Reipurth, B., Ward-Thompson, D., et al. 1997, ApJL, 474, L135+

Chini, R., Ward-Thompson, D., Kirk, J. M., et al. 2001, A&A, 369, 155

Chrysostomou, A., Hough, J. H., Aspin, C., & Bailey, J. A. 1994, MNRAS, 268, L63

Codella, C., Benedettini, M., Beltrán, M. T., et al. 2009, A&A, 507, L25

Codella, C., Lefloch, B., Ceccarelli, C., et al. 2010, A&A, 518, L112

Crimier, N., Ceccarelli, C., Alonso-Albi, T., et al. 2010, A&A, 516, A102+

Curtis, E. I., Richer, J. S., Swift, J. J., & Williams, J. P. 2010, MNRAS, 408, 1516

Cyganowski, C. J., Whitney, B. A., Holden, E., et al. 2008, AJ, 136, 2391

De Buizer, J. M. 2003, MNRAS, 341, 277

De Buizer, J. M. & Vacca, W. D. 2010, AJ, 140, 196

Dionatos, O., Nisini, B., Cabrit, S., Kristensen, L., & Pineau Des Forêts, G. 2010, A&A, 521, A7+

Dionatos, O., Nisini, B., Garcia Lopez, R., et al. 2009, ApJ, 692, 1

Dutrey, A., Guilloteau, S., & Bachiller, R. 1997, A&A, 325, 758

Eisloffel, J., Mundt, R., Ray, T. P., & Rodriguez, L. F. 2000, Protostars and Planets IV, 815

Eislöffel, J., Smith, M. D., Davis, C. J., & Ray, T. P. 1996, AJ, 112, 2086

Ellingsen, S. P., Shabala, S. S., & Kurtz, S. E. 2005, MNRAS, 357, 1003

Enoch, M. L., Young, K. E., Glenn, J., et al. 2006, ApJ, 638, 293

Froebrich, D. 2005, ApJS, 156, 169

Fuente, A., Ceccarelli, C., Neri, R., et al. 2007, A&A, 468, L37

Fuente, A., Martin-Pintado, J., Bachiller, R., Neri, R., & Palla, F. 1998, A&A, 334, 253

Fuente, A., Martın-Pintado, J., Bachiller, R., Rodrıguez-Franco, A., & Palla, F. 2002, A&A, 387, 977

Fuente, A., Neri, R., Martín-Pintado, J., et al. 2001, A&A, 366, 873

Garay, G., Brooks, K. J., Mardones, D., & Norris, R. P. 2006, ApJ, 651, 914

Giannini, T., Nisini, B., & Lorenzetti, D. 2001, ApJ, 555, 40

Giannini, T., Nisini, B., Neufeld, D., et al. 2011, ApJ, 738, 80

Goldsmith, P. F. & Langer, W. D. 1999, ApJ, 517, 209

Guan, X., Stutzki, J., Graf, U., et al. 2012, A&A, this volume

Gueth, F. & Guilloteau, S. 1999a, A&A, 343, 571

Gueth, F. & Guilloteau, S. 1999b, A&A, 343, 571

Gueth, F., Guilloteau, S., & Bachiller, R. 1996, A&A, 307, 891

Gueth, F., Guilloteau, S., & Bachiller, R. 1998, A&A, 333, 287

Gueth, F., Guilloteau, S., Dutrey, A., & Bachiller, R. 1997, A&A, 323, 943

Gusdorf, A., Anderl, S., Güsten, R., et al. 2012, A&A, this volume

Gusdorf, A., Cabrit, S., Flower, D. R., & Pineau Des Forêts, G. 2008a, A&A, 482, 809

Gusdorf, A., Giannini, T., Flower, D. R., et al. 2011, A&A, 532, A53

Gusdorf, A., Pineau Des Forêts, G., Cabrit, S., & Flower, D. R. 2008b, A&A, 490, 695

Güsten, R., Nyman, L. Å., Schilke, P., et al. 2006, A&A, 454, L13

Harvey, P. M. & Gatley, I. 1983, ApJ, 269, 613

Hatchell, J., Fuller, G. A., & Ladd, E. F. 1999, A&A, 346, 278

Heyminck, S., Graf, U., Güsten, R., et al. 2012, A&A, this volume

Hirano, N., Liu, S.-Y., Shang, H., et al. 2006, ApJL, 636, L141

Hirano, N. & Taniguchi, Y. 2001, ApJL, 550, L219

Hirota, T., Honma, M., Imai, H., et al. 2011, Publications of the ASJ, 63, 1

Ho, P. T. P., Moran, J. M., & Lo, K. Y. 2004, ApJL, 616, L1

Jiménez-Serra, I., Martín-Pintado, J., Caselli, P., Viti, S., & Rodríguez-Franco, A. 2009, ApJ, 695, 149

Johnstone, D. & Bally, J. 1999, ApJL, 510, L49

Jørgensen, J. K., Bourke, T. L., Myers, P. C., et al. 2007, ApJ, 659, 479

Kasemann, C., Güsten, R., Heyminck, S., et al. 2006, in Society of Photo-Optical Instrumentation Engineers (SPIE) Conference Series, Vol. 6275, Society of Photo-Optical Instrumentation Engineers (SPIE) Conference Series

Kawamura, J. H., Hunter, T. R., Tong, C.-Y. E., et al. 1999, Public. of the Astron. Soc. Pac., 111, 1088

Klein, B., Hochgürtel, S., Krämer, I., et al. 2012, A&A, this volume

Klein, B., Philipp, S. D., Krämer, I., et al. 2006, A&A, 454, L29

Kraemer, K. E., Deutsch, L. K., Jackson, J. M., et al. 1999, ApJ, 516, 817

Kraus, S., Hofmann, K.-H., Menten, K. M., et al. 2010, Nature, 466, 339

Kwan, J. & Scoville, N. 1976, ApJL, 210, L39

Kwan, J. & Tademaru, E. 1995, ApJ, 454, 382

Kwon, W., Looney, L. W., Crutcher, R. M., & Kirk, J. M. 2006, ApJ, 653, 1358

Langer, W. D. & Penzias, A. A. 1993, ApJ, 408, 539

Lee, C.-F., Ho, P. T. P., Palau, A., et al. 2007, ApJ, 670, 1188

Lee, C.-F., Mundy, L. G., Reipurth, B., Ostriker, E. C., & Stone, J. M. 2000, ApJ, 542, 925

Lefloch, B., Cabrit, S., Codella, C., et al. 2010, A&A, 518, L113

Lefloch, B., Cernicharo, J., Pacheco, S., & Ceccarelli, C. 2011, A&A, 527, L3

Lefloch, B., Eisloeffel, J., & Lazareff, B. 1996, A&A, 313, L17

Leurini, S., Schilke, P., Parise, B., et al. 2006, A&A, 454, L83

Li, Z.-Y. & Shu, F. H. 1996, ApJ, 472, 211

Looney, L. W., Tobin, J. J., & Kwon, W. 2007, ApJL, 670, L131

López-Sepulcre, A., Codella, C., Cesaroni, R., Marcelino, N., & Walmsley, C. M. 2009, A&A, 499, 811

Loughran, L., McBreen, B., Fazio, G. G., et al. 1986, ApJ, 303, 629

Mac Low, M.-M. & Klessen, R. S. 2004, Reviews of Modern Physics, 76, 125

Mangum, J. G. & Wootten, A. 1993, ApJS, 89, 123

Margulis, M. & Lada, C. J. 1985, ApJ, 299, 925

Martin-Pintado, J., Bachiller, R., & Fuente, A. 1992a, A&A, 254, 315

Martin-Pintado, J., Bachiller, R., & Fuente, A. 1992b, A&A, 254, 315

Masson, C. R. & Chernin, L. M. 1993, ApJ, 414, 230

Matthews, B. C., Lai, S.-P., Crutcher, R. M., & Wilson, C. D. 2005, ApJ, 626, 959

Matzner, C. D. & McKee, C. F. 1999, ApJL, 526, L109

McBreen, B., Fazio, G. G., Stier, M., & Wright, E. L. 1979, ApJL, 232, L183

McCaughrean, M. J., Rayner, J. T., & Zinnecker, H. 1994, ApJL, 436, L189

Menten, K. M., Reid, M. J., Forbrich, J., & Brunthaler, A. 2007, A&A, 474, 515

Molinari, S., Swinyard, B., Bally, J., et al. 2010, A&A, 518, L100

Moro-Martín, A., Noriega-Crespo, A., Molinari, S., et al. 2001, ApJ, 555, 146

Neckel, T. 1978, A&A, 69, 51

Neufeld, D. A., Nisini, B., Giannini, T., et al. 2009, ApJ, 706, 170

Nisini, B., Benedettini, M., Giannini, T., et al. 1999, A&A, 350, 529

Nisini, B., Benedettini, M., Giannini, T., et al. 2000, A&A, 360, 297

Nisini, B., Codella, C., Giannini, T., & Richer, J. S. 2002, A&A, 395, L25

Nisini, B., Codella, C., Giannini, T., et al. 2007, A&A, 462, 163

Nisini, B., Giannini, T., Neufeld, D. A., et al. 2010, ApJ, 724, 69

Palau, A., Ho, P. T. P., Zhang, Q., et al. 2006, ApJL, 636, L137

Peretto, N. & Fuller, G. A. 2009, A&A, 505, 405

Price, S. D., Egan, M. P., Carey, S. J., Mizuno, D. R., & Kuchar, T. A. 2001, AJ, 121, 2819

Raga, A. & Cabrit, S. 1993, A&A, 278, 267

Raga, A. C., Binette, L., Canto, J., & Calvet, N. 1990, ApJ, 364, 601

Raga, A. C. & Kofman, L. 1992, ApJ, 386, 222

Reipurth, B., Bally, J., & Devine, D. 1997, AJ, 114, 2708

Richer, J. S., Shepherd, D. S., Cabrit, S., Bachiller, R., & Churchwell, E. 2000, Protostars and Planets IV, 867

Rodriguez, L. F., Moran, J. M., & Ho, P. T. P. 1980, ApJL, 240, L149

Rohlfs, K. & Wilson, T. L. 2004, Tools of radio astronomy, ed. Rohlfs, K. & Wilson, T. L.

Sault, R. J., Staveley-Smith, L., & Brouw, W. N. 1996, A&AS, 120, 375

Schilke, P., Walmsley, C. M., Pineau des Forets, G., & Flower, D. R. 1997, A&A, 321, 293

Schöier, F. L., Jørgensen, J. K., van Dishoeck, E. F., & Blake, G. A. 2004, A&A, 418, 185

Schuller, F., Menten, K. M., Contreras, Y., et al. 2009, A&A, 504, 415

Scoville, N. Z., Carlstrom, J. E., Chandler, C. J., et al. 1993, Public. of the Astron. Soc. Pac., 105, 1482

Seale, J. P. & Looney, L. W. 2008, ApJ, 675, 427

Shang, H., Allen, A., Li, Z.-Y., et al. 2006, ApJ, 649, 845

Shepherd, D. S. 2005, ArXiv Astrophysics e-prints

Shepherd, D. S. & Churchwell, E. 1996, ApJ, 472, 225

Shepherd, D. S., Yu, K. C., Bally, J., & Testi, L. 2000, ApJ, 535, 833

Shimajiri, Y., Takahashi, S., Takakuwa, S., Saito, M., & Kawabe, R. 2009, Publications of the ASJ, 61, 1055

Shu, F. H., Adams, F. C., & Lizano, S. 1987, Annual Review of Astron and Astrophys, 25, 23

Shu, F. H., Ruden, S. P., Lada, C. J., & Lizano, S. 1991, ApJL, 370, L31

Simpson, J. P., Burton, M. G., Colgan, S. W. J., et al. 2009, ApJ, 700, 1488

Smith, H. A., Hora, J. L., Marengo, M., & Pipher, J. L. 2006, ApJ, 645, 1264

Smith, M. D., Froebrich, D., & Eislöffel, J. 2003, ApJ, 592, 245

Snell, R. L. 1987, in IAU Symp. 115: Star Forming Regions, 213–236

Snell, R. L., Loren, R. B., & Plambeck, R. L. 1980, ApJL, 239, L17

Stanke, T., McCaughrean, M. J., & Zinnecker, H. 2002, A&A, 392, 239

Tafalla, M. & Bachiller, R. 1995, ApJL, 443, L37

Tafalla, M., Bachiller, R., Wright, M. C. H., & Welch, W. J. 1997, ApJ, 474, 329

Tafalla, M., Santiago-García, J., Hacar, A., & Bachiller, R. 2010, A&A, 522, A91+

Takahashi, S. & Ho, P. T. P. 2012, ApJL, 745, L10

Takahashi, S., Ho, P. T. P., Tang, Y.-W., Kawabe, R., & Saito, M. 2009, ApJ, 704, 1459

Takahashi, S., Saito, M., Ohashi, N., et al. 2008, ApJ, 688, 344

Takahashi, S., Saito, M., Takakuwa, S., & Kawabe, R. 2006, ApJ, 651, 933

Takami, M., Karr, J. L., Koh, H., Chen, H.-H., & Lee, H.-T. 2010, ApJ, 720, 155

Tielens, A. G. G. M. & Whittet, D. C. B. 1997, in IAU Symposium, Vol. 178, IAU Symposium, ed. E. F. van Dishoeck, 45–+

Tobin, J. J., Looney, L. W., Mundy, L. G., Kwon, W., & Hamidouche, M. 2007, ApJ, 659, 1404

Umemoto, T., Iwata, T., Fukui, Y., et al. 1992, ApJL, 392, L83

Umemoto, T., Mikami, H., Yamamoto, S., & Hirano, N. 1999, ApJL, 525, L105

Urquhart, J. S., Busfield, A. L., Hoare, M. G., et al. 2007, A&A, 474, 891

Vaidya, B., Fendt, C., Beuther, H., & Porth, O. 2011, ApJ, 742, 56

van der Tak, F. F. S., Black, J. H., Schöier, F. L., Jansen, D. J., & van Dishoeck, E. F. 2007, A&A, 468, 627

van Dishoeck, E. F., Jansen, D. J., & Phillips, T. G. 1993, A&A, 279, 541

van Kempen, T. A., Green, J. D., Evans, N. J., et al. 2010a, A&A, 518, L128+

van Kempen, T. A., Kristensen, L. E., Herczeg, G. J., et al. 2010b, A&A, 518, L121+

van Kempen, T. A., van Dishoeck, E. F., Güsten, R., et al. 2009a, A&A, 507, 1425

van Kempen, T. A., van Dishoeck, E. F., Güsten, R., et al. 2009b, A&A, 501, 633

Velusamy, T., Langer, W. D., Kumar, M. S. N., & Grave, J. M. C. 2011, ApJ, 741, 60

Visser, R., Kristensen, L. E., Bruderer, S., et al. 2012, A&A, 537, A55

Viti, S., Jimenez-Serra, I., Yates, J. A., et al. 2011, ApJL, 740, L3+

Watanabe, N. & Kouchi, A. 2002, ApJL, 571, L173

Williams, J. P., Plambeck, R. L., & Heyer, M. H. 2003, ApJ, 591, 1025

Yang, B., Stancil, P. C., Balakrishnan, N., & Forrey, R. C. 2010, ApJ, 718, 1062

Yıldız, U. A., van Dishoeck, E. F., Kristensen, L. E., et al. 2010, A&A, 521, L40

Yu, K. C., Bally, J., & Devine, D. 1997, ApJL, 485, L45+

Zapata, L. A., Ho, P. T. P., Rodríguez, L. F., et al. 2006, ApJ, 653, 398

Zhang, Q., Ho, P. T. P., & Wright, M. C. H. 2000, AJ, 119, 1345

Zhang, Q., Ho, P. T. P., Wright, M. C. H., & Wilner, D. J. 1995, ApJL, 451, L71+

Zhang, Q., Hunter, T. R., Brand, J., et al. 2005, ApJ, 625, 864

Zhang, Q., Hunter, T. R., Brand, J., et al. 2001, ApJL, 552, L167

Zinnecker, H. & Yorke, H. W. 2007, Annual Review of Astron and Astrophys, 45, 481

List of Publications

Gómez-Ruiz, A. I., Gusdorf, A., Leurini, S., Codella, C., Güsten, R., Wyrowski, F., Requena-Torres, M. A., Risacher, C., & Wampfler, S. F. *"High-J CO emission in the Cepheus E protostellar outflow observed with SOFIA/GREAT,"* 2012, A&A, 512, L9.

Gómez-Ruiz, A. I., Hirano, N., Leurini, S., & Liu, S.-Y. *"The L1157 protostellar outflow imaged with the SMA,"* 2012, submitted to A&A.

Gómez-Ruiz, A. I., Wyrowski, F., Gusdorf, A., Leurini, S., Menten, K., & Güsten, R. *"Warm gas in protostellar outflows I. Flows from the low-mass protostars L1448 and HH211,"* 2012, submitted to A&A.

Acknowledgements

... siento que tengo que dar las gracias a una multitud de personas, incluso aquellas que ya he olvidado, que al amarme o al estar simplemente a mi lado, con su fraternal presencia no sólo me han ayudado a vivir, sino que son, tal vez, mi misma vida.
Marisa Madieri

I would like to first thank Prof. Karl Menten for allowing me to work in his group at MPIfR to perform the research for this PhD thesis, and also for his advice and support to my career. I also give thanks to Dr. Friedrich Wyrowski who supervised my work and actually suggested many of the ideas presented here. I am also in debt with Dr. Silvia Leurini and Dr. Antoine Gusdorf for all the patience, time, and ideas that made me improve my work at different levels. I also give a big thank you to all APEX staff Chile and the submillimeter technologies group at MPIfR, from whom I learned lots of good stuff. In particular I thank Dr. Rolf Güsten for the very nice conversions about the submillimeter eyes and the instruments related to them.

I also thank very much my officemates, Laura, Felipe, Fujun, Fang-Chun, and Lisa, for the company and help during all these years of hard work. Without them the life would have been definitely much harder. Although with very different backgrounds and idiosyncrasies, I think we had great times together in the *kinderzimmer*. I could spent lots of lines describing the reason for my gratitude towards you, but as you know I am already writing a novel about the crazy life and adventures of the people in raum 2.36. At the same level I thank the company and friendship of Ana-Felipe and Brenda, who can also be part of my novel. Actually such story can go as long as the never ending Garcia-Marquez works, and as such I must include here my gratitude to Verena Gielen, with whom I learned different aspects about the life outside the astro-world and the life in Germany, y muchos otros aspectos de la vida que resultaria un poco complicado de explicarlos aqui.

Finalmente agradezco infinitamente a mis padres, hermanos y hermana, quienes me apoyaron en todo momento durante todos estos años en el camino, algunas veces solitario, que lleva a las estrellas.

Arturo I. Gómez-Ruiz
Bonn, 2012